# Characterization of Nonequilibrium Reacting Molecular Plasmas and Flames using Coherent Anti-Stokes Raman Spectroscopy

**DISSERTATION**

Presented in Partial Fulfillment of the Requirements for the Degree Doctor of Philosophy in the Graduate School of The Ohio State University

By

Yi-chen Hung, M.S.

Graduate Program in Chemical Physics

The Ohio State University

2018

Dissertation Committee

Dr. Igor Adamovich, Advisor

Dr. Heather Allen

Dr. Hannah Shafaat

Dr. Douglass Schumacher

# Abstract

Broadband ns coherent anti-Stokes Raman Spectroscopy (CARS) diagnostics is used to study vibrational energy transfer in the afterglow of a diffuse filament, ns pulse discharge in nitrogen, air, and their mixtures with carbon dioxide and hydrogen. The results indicate that nitrogen vibrational excitation in the discharge occurs by electron impact, with subsequent vibration-vibration (V-V) energy transfer within $N_2$ vibrational manifold, vibration-translation (V-T) relaxation, and near-resonance V-V′ energy transfer from $N_2$ to $CO_2$ asymmetric stretch vibrational mode. This considerably accelerates the net rate of energy thermalization and temperature rise in the afterglow and demonstrates that adding $CO_2$ to nonequilibrium flows of nitrogen and air would result in a rapid temperature increase. Measurements of temperature, $N_2$ vibrational temperature, and OH number density in nitrogen, air, and $H_2$-air mixtures are used to study a possible effect of nitrogen vibrational excitation on low-temperature kinetics of $HO_2$ and OH radicals, at high specific energy loading. CARS measurements demonstrate that the discharge generates strong vibrational nonequilibrium in air and $H_2$-air mixtures. The kinetics of population and decay of $N_2$ vibrational levels at these conditions are well understood. Laser Induced Fluorescence measurements of OH number density show that it peaks in the afterglow, at approximately the same time as $N_2$ vibrational temperature. However, comparison of the experimental data with kinetic modeling predictions shows that OH number density at the present conditions is not affected by $N_2$ vibrational excitation directly. Kinetic modeling predicts a transient OH number density overshoot at a higher discharge coupled energy, due to the temperature rise caused by $N_2$ vibrational relaxation by O atoms, which may well be a dominant effect in discharges with high specific energy loading.

CARS diagnostics has also been used to characterize a microwave discharge plasma in nitrogen, to determine the potential of a cw microwave discharge for energy-efficient plasmachemical dissociation of $CO_2$. The measurement results indicate that rotational-translational temperature in a cw microwave discharge plasma in nitrogen is very high, up to T = 2000 K, such that it is extremely unlikely that significant vibrational nonequilibrium of $N_2$ or $CO_2$ can be sustained at these conditions. However, operating a pulsed microwave discharge at a very low duty cycle resulted in significant $N_2$ vibrational nonequilibrium. In the afterglow, the plasma rapidly approaches near thermal equilibrium. The results suggest that energy efficient $CO_2$ dissociation in pure $CO_2$ or in $CO_2$-$N_2$ microwave discharges may be achieved either during pulsed operation, or at conditions when the flow residence time in the discharge is very short, as occurs in discharges sustained in supersonic flows.

Finally, CARS diagnostics, combined with CARS-like ps Four-Wave Mixing and ps Second Harmonic Generation diagnostics, has been used for temperature and electric field measurements in atmospheric pressure hydrogen diffusion flames, enhanced by ns pulse and AC discharges. The four-wave mixing measurements show that peak electric field during breakdown in the flame, approximately 40 kV/cm, is significantly lower compared to that in room air, 75 kV/cm, due to the higher temperature of the combustion products, T = 1300 ± 150 K. Both in air and in the flame, the electric field follows the applied voltage before breakdown and decreases rapidly after breakdown, due to plasma self-shielding. Peak reduced electric field measured in the plasma sustained in the flame varies from E/N = 300 Td to 800 Td. To improve the sensitivity, electric field was also measured by ps Second Harmonic Generation. Temperature distribution in the flame was measured vs. the height above the burner exit and vs. the transverse distance across the flame. When the distance

between the discharge electrodes is reduced, the flame becomes attached to the top of the electrodes instead of the burner exit. Temperature and time-resolved electric field are measured in a ns pulse discharge sustained both in the low-temperature hydrogen flow below the flame (T = 370 K) and in the hydrogen diffusion flame (T ≈ 1500 K). Peak reduced electric field measured in a near-room temperature hydrogen flow (≈ 100 Td) is close to breakdown field in hydrogen predicted by Paschen law. Peak reduced electric field in the flame is approximately a factor of 2 higher, due to the lower number density in the plasma. Electric field measurement in the AC plasma sustained in the flame demonstrate strong near-DC electric field offset ("ion wind") resulting in flame distortion at these conditions.

# Dedication

Dedicated to my grandfather, Kan-lin Hung,

whose hard work and selfless dedication cultivate his family

# Acknowledgements

First of all, I would like to thank my advisor, Igor Adamovich. Without his patience, support and guidance over the past four years, I cannot accomplish my ph.D degree. The last two years of my ph.D career are especially fruitful and rewarding.

Many thanks to my colleague, Dr. Kraig Frederickson for providing introduction to coherent anti-Stokes Raman scattering spectroscopy, and assisting me to set up my own experiments. Without your help, I cannot image how much more time I need to spend to get things work.

Thanks to Dr. Marien Simeni Simeni not only for countless discussions about lab works but also for sincere friendship during the past three years. Wish you have a wonderful life in the next stage of career life. Bon voyage! Thanks to Mr. Elijah Jans for helps in my experiments. Your enthusiasm for learning is impressing.

Thanks to the wonderful people that I have met in the non-equilibirum thermodynamics laboratory in the Ohio State University: Dr. Walter Lempert, Dr. Bill Rich, Dr. Ben Goldberg, Dr. Vitaly Petrishchev, Dr. Caroline Winters, Dr. Zak Eckert, and Mr. Ilya Gulko. Working with you guys are an incredible and precious experience to me.

Finally, thanks to my husband Wei-ming Hung. Your love and support are the best cure-all for my darkest moments during graduate school. Thank you for taking care about my family when I was not in Taiwan. I owe you too much. I would also like to thank both the financial and mental supports from my family members.

# Vita

2006 National Taichung Girls Senior High School, Taichung, Taiwan

2010 B.S. Applied Chemistry, National Chiao Tung University,Hsinchu, Taiwan

2011 Research Assistant, Academia Sinica, Nankang, Taipei City, Taiwan

2016 M.S. Chemical Physics, The Ohio State University, Columbus, Ohio, USA

2012 – present Graduate Research Assistant, Chemical Physics Graduate Program,

Department of Chemistry, The Ohio State University, Columbus, Ohio, USA

# Publications

[1] Simokaitiene, J.; Stanislovaityte, E.; Grazulevicius, J.; Jankauskas, V.; Gu, R.; Dehaen, W.; Hung, YC. and Hsu, CP. "Methoxyphenyl-substituted derivatives of indolo[3,2-b]carbazole: structure-properties relationship" J. Org. Chem., 2012, 77(11), pp 4924-4931

[2] You, ZQ; Hung, YC and Hsu, CP "Calculating Electron Transfer Coupling with Density Functional Theory: The Long-Range Corrected Density Functionals" J. Phys. Chem. B, 2015, 119(24), pp 7480-7490

[3] K. Frederickson, Y.-C. Hung, W.R. Lempert, and I.V. Adamovich, "Control of Vibrational Distribution Functions in Nonequilibrium Molecular Plasmas and High-Speed Flows", Plasma Sources Science and Technology, vol. 26, 2017, p. 014002

[4] C. Winters, Y.-C. Hung, E. Jans, Z. Eckert, K. Frederickson, I.V. Adamovich, and N. Popov, "OH Radical Kinetics in Hydrogen-Air Mixtures at the Conditions of Strong Vibrational Nonequilibrium", Journal of Physics D: Applied Physics, vol. 50, 2017, p. 505203

[5] M. Simeni Simeni, E. Baratte, Y.-C. Hung, K. Frederickson, and I.V. Adamovich, "Ps Four-Wave Mixing Measurements of Electric field in a Ns Pulse Discharge in a Hydrogen Diffusion Flame", accepted for publication in Proceedings of the Combustion Institute, 2018

# Fields of Study

Major Field: Chemical Physics

# Table of Contents

# List of Tables

# List of Figures

# Chapter 1. Introduction

## 1.1. Energy Partition in Nonequilibrium Molecular Plasmas

Characterization of high-pressure nonequilibrium plasmas using non-intrusive laser diagnostics is essential for development of a number of engineering applications such as high-speed plasma flow control, plasma assisted combustion, plasma materials processing, and novel plasma chemical synthesis. Specific parameters that are critically important for efficient use of plasmas for these applications include reduced electric field (ratio of the electric field to the number density, E/N), electron density and temperature, heavy species temperature, vibrational level populations of dominant molecular species, and number densities of excited electronic states and highly reactive radical species. The use of nanosecond pulse duration discharges for these applications are of particular interest since they can generate diffuse nonequilibrium plasmas at high pressures (~1 bar) and high pulse repetition rates (up to ~100 kHz), and are characterized by high peak reduced electric fields, *E/N*, up to several hundred Townsend (1 Td = $10^{-17}$ V·cm$^2$). However, other types of electric discharge sustained in high-pressure gas mixtures, such as AC dielectric barrier discharges (AC-DBD) and microwave discharges, have also been used widely. It is well known that energy partition among different energy modes in nonequilibrium, low-temperature, high-pressure plasmas (rotational, vibrational, electronic, dissociation, and ionization) is controlled primarily by the electron energy distribution function. Over a wide range of conditions, this partition can be characterized in terms of the reduced electric field, *E/N*. Therefore the knowledge of this key parameter is critical for insight into kinetics of energy transfer and chemical reactions in these plasmas. At high E/N values, ~10 - 300 Td, a

significant fraction of discharge input energy goes into population of excited states of molecules (vibrational and electronic), as well as molecular dissociation and ionization by electron impact.

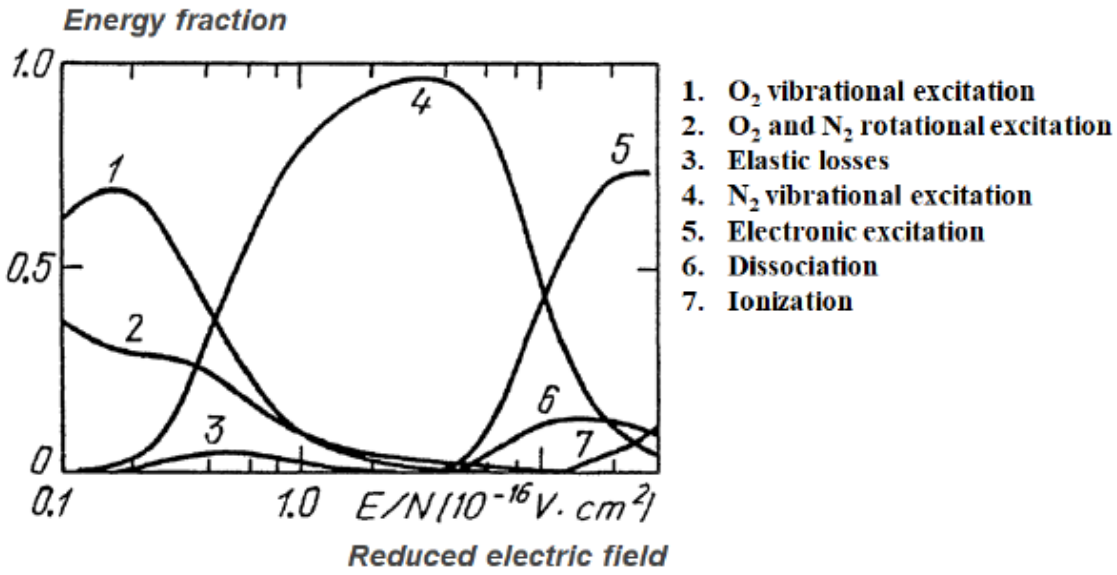


**Figure 1.1. Energy partition among different molecular energy modes vs. reduced electric field (E/N) in an electric discharge in dry air [1].**

As an illustration, Figure 1.1 [1] plots the discharge input energy partition among different molecular energy modes of $N_2$ and $O_2$ in dry air, versus the reduced electric field. It can be seen that a significant fraction of the discharge energy goes to electron impact excitation of vibrational and electronic states of $N_2$ molecules. Energy partition in nonequilibrium plasmas sustained in other molecular gases is qualitatively similar to the one shown in Figure 1.1 [1]. Collisional quenching of the excited states (including reactive quenching) and reactions of radical species generated in the discharge considerably expand the variety of energy transfer processes and chemical reactions in low-temperature gas mixtures. From a fundamental kinetics perspective, however, some of the dominant energy transfer and chemical reaction processes in these plasmas remain not fully understood.

## 1.2. Effect of Reaction of Excited Electronic Species on Fluid Mechanics and Plasma Chemistry

In air and fuel-air mixtures, electronically excited nitrogen molecules $N_2$ ($A^3\Sigma_u^+, B^3\Pi_g, C^3\Pi_u, a^1\Sigma_u^-$) and O atoms, O($^1$D), generated during the discharge by electron impact, react with $O_2$ and fuel species, such as $H_2$ or $CH_4$, to produce O atoms, H atoms, and OH radicals,

$$N_2{}^*\left(A^3\Sigma_u^+, B^3\Pi_g, C^3\Pi_u, a^1\Sigma_u^-\right) + O_2 \rightarrow N_2\left(X^1\Sigma_g^+\right) + O + O\,, \quad \text{(Equation 1.1)}$$

$$N_2{}^*\left(A^3\Sigma_u^+, B^3\Pi_g, C^3\Pi_u, a^1\Sigma_u^-\right) + H_2 \rightarrow N_2\left(X^1\Sigma_g^+\right) + H + H\,, \quad \text{(Equation 1.2)}$$

$$N_2{}^*\left(A^3\Sigma_u^+, B^3\Pi_g, C^3\Pi_u, a^1\Sigma_u^-\right) + CH_4 \rightarrow N_2\left(X^1\Sigma_g^+\right) + CH_3 + H\,, \quad \text{(Equation 1.3)}$$

$$O(^1D) + H_2 \rightarrow OH + H. \qquad \text{(Equation 1.4)}$$

in addition to dissociation of $O_2$, $H_2$, and hydrocarbon species by direct electron impact,

$$O_2 + e \rightarrow O + O + e, \qquad \text{(Equation 1.5)}$$

$$H_2 + e \rightarrow H + H + e, \qquad \text{(Equation 1.6)}$$

$$CH_4 + e \rightarrow CH_3 + H + e. \qquad \text{(Equation 1.7)}$$

These reactions provide a major contribution to the net rate of atomic species generation in nonequilibrium plasmas. Since the rate coefficients for most of these quenching processes are comparable with the gas-kinetic collision rate, they also result in rapid heating of the plasma, generating localized thermal perturbations. In air, the effect of rapid thermalization of internal energy on a sub-acoustic time scale, which generates high-amplitude pressure perturbations in air flows (e.g. see Figure 1.2), has been quantified only recently [2-6].

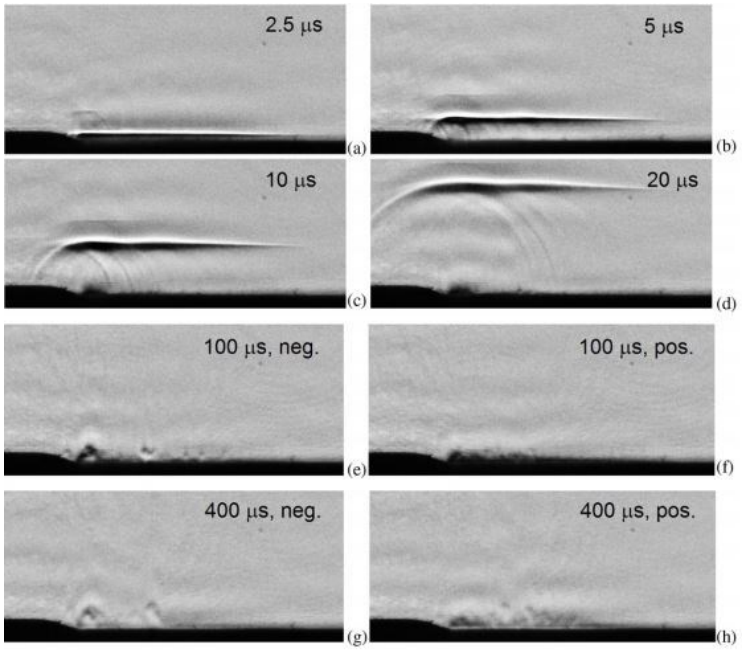


**Figure 1.2. Schlieren images of perturbations produced by a surface ns pulse discharge for different delay times after the discharge pulse in quiescent air at atmospheric pressure. Image size 25 x 11 mm. Pulse peak voltage 12 kV, pulse repetition rate 200 Hz, camera gate 12 ns [2].**

This effect has a significant potential for high-speed plasma flow control, since high-amplitude thermal and pressure perturbations result in formation of large-scale coherent structures in high-speed flows [2]. Figure 1.3 [7] shows computational modeling predictions and experimental images illustrating formation of coherent structures (spanwise vortices) and boundary layer reattachment in a flow over an airfoil, under the impact of several ns discharge pulses. The modeling calculations demonstrate that localized thermal perturbations in a near-surface ns pulse discharge trigger a flow instability and

vortex formation, resulting in a major effect on the flow (boundary layer reattachment), as well as reducing drag and increasing lift on the airfoil.

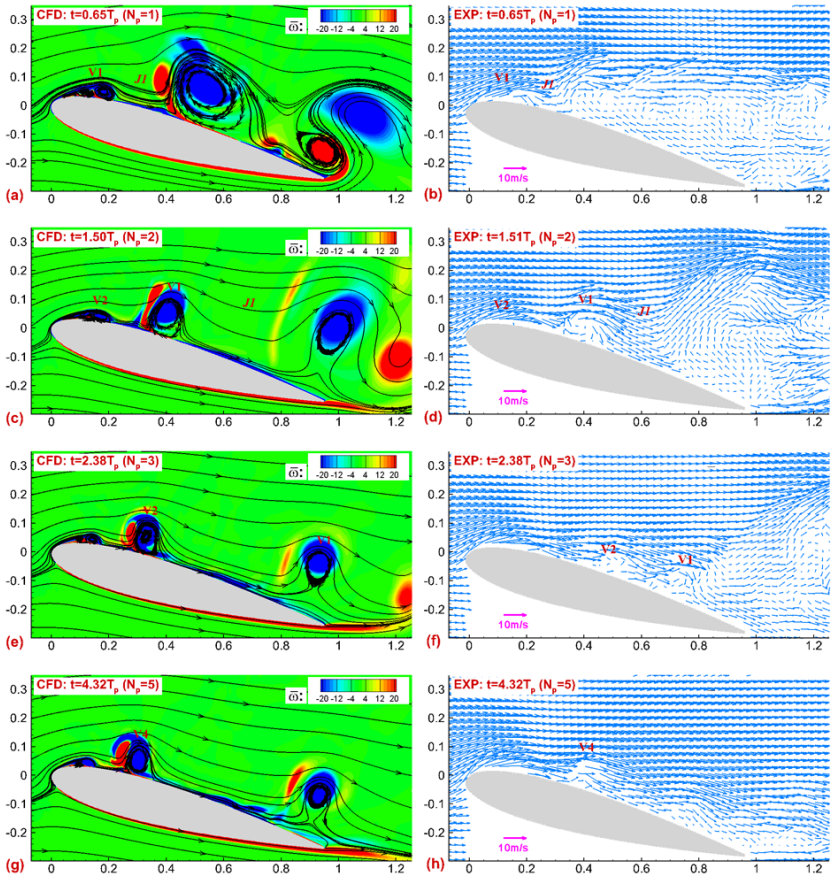


**Figure 1.3. Computational modeling (left column) and experimental (right column) images showing formation of coherent structures (spanwise vortices) and boundary layer reattachment in a flow over an airfoil, under the impact of several ns discharge pulses (1, 2, 3, and 5 pulses, respectively). Flow velocity ~ 10 m/s. In each plot, $T_p = 1/f$ denotes the actuation period [7].**

H atoms, O atoms, and OH radicals generated in the plasma are also highly reactive species which initiate chain propagation and chain branching reactions of fuel oxidation even at relatively low temperatures, which is the dominant effect in plasma-assisted combustion applications [8-10]. Figure 1.4 [11] shows that a burst of ns duration discharge pulses generated in a stoichiometric ethylene-air mixture results in its ignition. Comparison with kinetic modeling predictions demonstrates that fuel oxidation and ignition occur due to reactions of radicals produced during quenching of excited electronic states of $N_2$ and O.

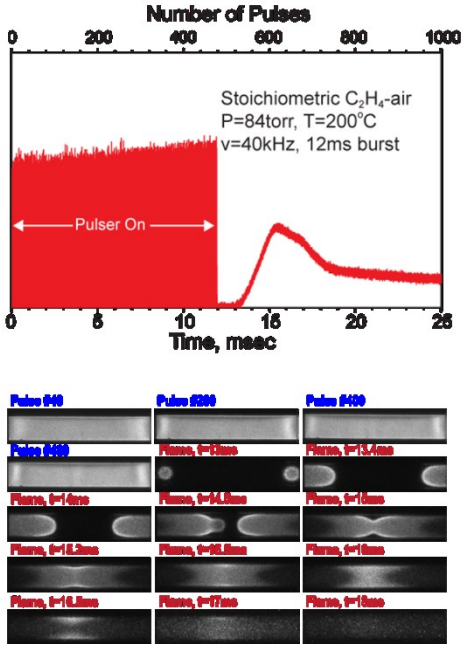


**Figure 1.4. (a) OH emission (310 nm) and (b) broadband plasma emission images of a repetitively pulsed ns discharge and a flame in a stoichiometric ethylene-air mixture ($T_0$ = 473 K, P = 84 Torr, f = 40 kHz). Discharge burst duration is 12 ms long, ignition occurs at t = 13 ms [11].**

### 1.3. Vibrational Relaxation and Energy Thermalization in Air Plasma

Compared to reactions of excited electronic states, the effect of $N_2$ vibrational relaxation on internal energy thermalization in air plasmas, high-speed flow field, and kinetics of fuel oxidation in fuel-air plasmas is not understood. Use of coupling between relaxation of vibrational energy modes and perturbations of macroscopic flow parameters may have a significant potential for high-speed flow field manipulation. At this time, understanding of coupling between relaxation of energy stored in the internal energy modes of molecules and the flow field remains incomplete. Recent experimental results point to the existence of strong coupling mechanisms between excitation/relaxation of the internal energy modes and the flow, such as delay of turbulent transition in hypersonic boundary layer flows caused by vibrational relaxation of $CO_2$ [12], or turbulence intensity reduction in low Reynolds number flows, when relaxation time of nitrogen vibrationally excited in an RF discharge matches the turbulence decay time [13]. However, detailed experimental data isolating and quantifying these mechanisms are not available. This requires measurements of key parameters of nonequilibrium, vibrationally relaxing, chemically reacting flows in a relatively simple flow geometry, which lends itself to detailed optical diagnostics.

Recent experiments at Ohio State [3,5] provide new insight into coupling of molecular energy transfer and fluid mechanics. In this work, kinetics of nonequilibrium energy addition to internal molecular modes in air on ns time scale, with subsequent energy transfer among different energy modes, on ns to ms time scale, has been studied using ps coherent Anti-Stokes Raman spectroscopy (CARS). These measurements were conducted in point-to-point, ns pulse, diffuse filament discharges in quiescent nitrogen and dry air. The

results yield direct, quantitative evidence of transient "rapid" heating of the gas on a sub-acoustic time scale (i.e. the characteristic time scale for propagation of pressure perturbations). Kinetic modeling analysis of these results [5] demonstrated that this effect occurs during collisional quenching of electronically excited $N_2$ molecules (see Figure 1.5(a)). These results also isolated the significant "slow" heating in air, on a time scale much longer compared to the acoustic time scale, which is nearly completely absent in nitrogen. Kinetic modeling calculations demonstrate that the "slow" heating is caused by vibration-translation (V-T) relaxation of nitrogen by O atoms (see Figure 1.5(b)). In contrast, V-T relaxation in pure nitrogen is quite slow, such that the "slow" temperature rise does not occur.

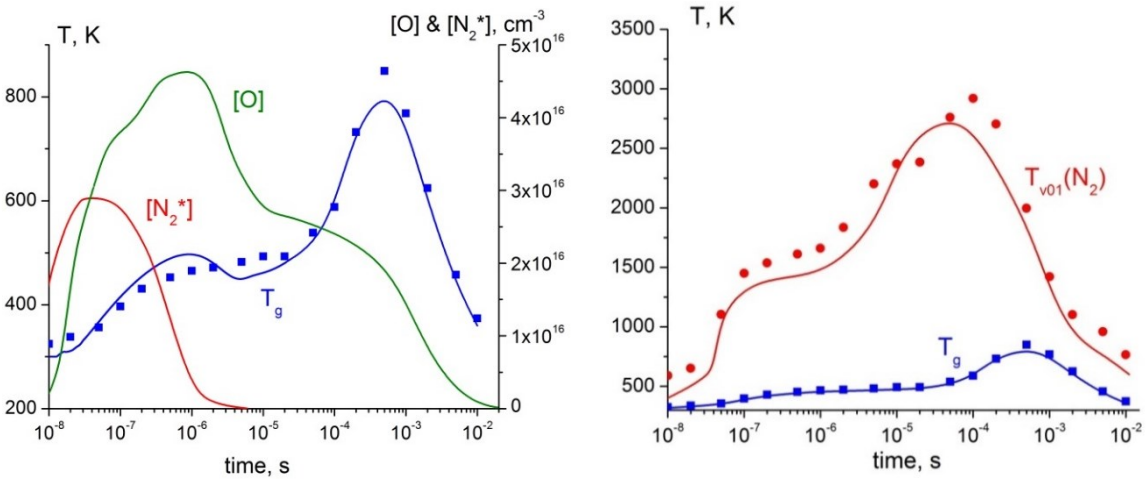


**Figure 1.5. (a) Comparison of experimental and predicted temperature during and after ns pulse discharge in dry air at P = 100 Torr, demonstrating a two-stage mechanism of energy thermalization. (b) Comparison of experimental and predicted temperature and $N_2$ vibrational temperature in air at these conditions [5].**

These processes affect energy transfer in nonequilibrium flows on widely different time scales, from hundreds of ns to hundreds of μs, producing a two-fold effect. First, as discussed above, energy thermalization on a sub-acoustic time scale ("rapid" localized heating) produces high-amplitude pressure perturbations (compression waves), which can be generated repeatedly by varying the discharge pulse repetition rate. Second, energy stored in the vibrational mode of nitrogen in the ground electronic state, $N_2(X^1\Sigma_g^+,v)$ is not thermalized sufficiently rapidly to contribute to compression wave formation. However, energy transfer from vibrationally excited $N_2$ to vibrational modes of $CO_2$, by rapid near-resonance vibration-vibration (V-V′) energy exchange, may well accelerate temperature rise and therefore affect the flow field due to the relatively rapid V-T relaxation of $CO_2$. Figure 1.6 [14] shows measurements of $N_2$ vibrational temperature distributions in a supersonic shear layer flow, with and without injection of $CO_2$ (a rapid V-T relaxer species) into the vibrationally nonequilibrium nitrogen flow, illustrating significant reduction of vibrational nonequilibrium in the shear layer. Figure 1.7 [12] compares schlieren images of the shear layer when non-excited nitrogen and $CO_2$ are injected into the flow. It can be seen that injection of $CO_2$, resulting in the temperature and pressure rise in the flow, shifts the shear layer up, demonstrating a strong effect of vibrational nonequilibrium on the supersonic flow field.

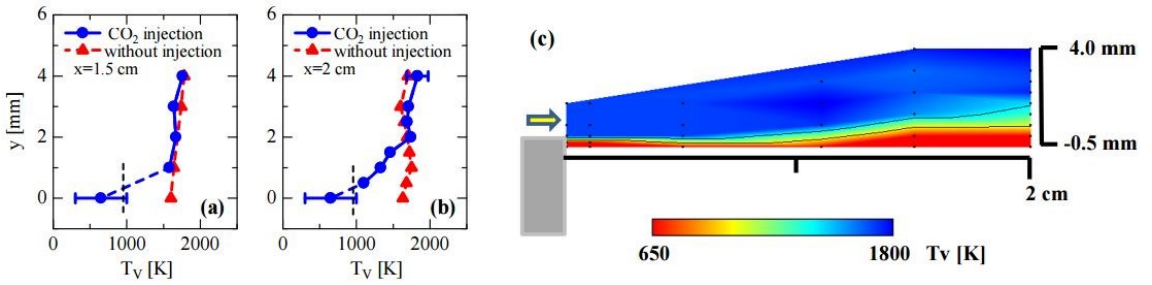


**Figure 1.6. (a, b) $N_2$ vibrational temperature distributions with and without $CO_2$ injection at different streamwise locations in a supersonic shear layer flow. (c) 2D vibrational temperature distribution in the shear layer with $CO_2$ injection [14].**

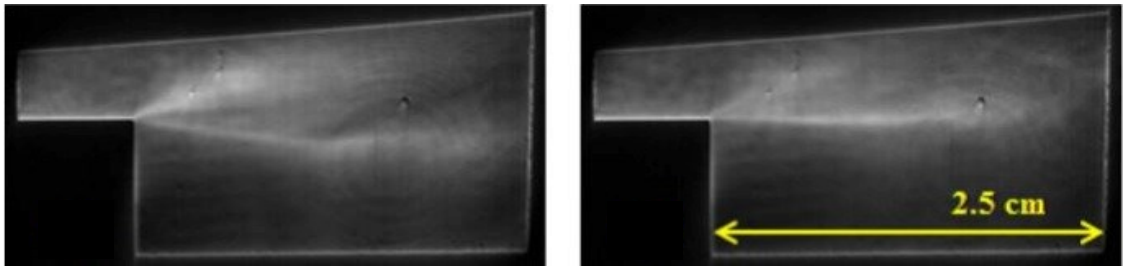


**Figure 1.7. Schlieren images of the shear layer (a) with injection of non-excited $N_2$, (b) with injection of an $N_2$-$CO_2$ mixture. The difference between the flow structure is apparent [12].**

One of the objectives of the present work is to identify, isolate, and quantify a specific mechanism of the accelerated $N_2$ vibrational energy relaxation via targeted loading and storage of energy in the internal molecular modes, and subsequent coupling to the flow by adding a rapid relaxer species, $CO_2$. The effect of accelerated vibrational relaxation on the flow may be used to generate high-amplitude perturbations in the boundary layer, shear layer, and shock wave/boundary layer interaction flows. Quantitative studies of the effect of

vibrational relaxation on a high-speed flow field would help determine feasibility of this approach for active aerodynamic control of high-speed flows.

### 1.4. Reactions of Vibrationally Excited Species in Fuel-Air Mixtures

The role of vibrationally excited nitrogen molecules in the ground electronic state, $N_2(X^1\Sigma_g^+,v)$, in chemical kinetics of reacting nonequilibrium plasmas remains rather poorly understood. It may well be significant for two principal reasons, (i) high input energy fraction into $N_2$ vibrational excitation by electron impact in electric discharges in air and fuel-air mixtures, as discussed above, and (ii) relatively slow $N_2$ vibrational relaxation rate, even in plasmas with significant concentrations of hydrogen, hydrocarbon species, and oxygen atoms. Because of this, considerable amount of energy in transient plasmas is stored in the vibrational energy mode of molecular nitrogen, which affects the rate of temperature rise [3, 4] and, indirectly, the rate coefficients of chemical reactions. To illustrate this, Figure 1.7 [4] shows that the temperature rise after a ns pulse discharge in $H_2$-air mixture is more significant compared to that in air.

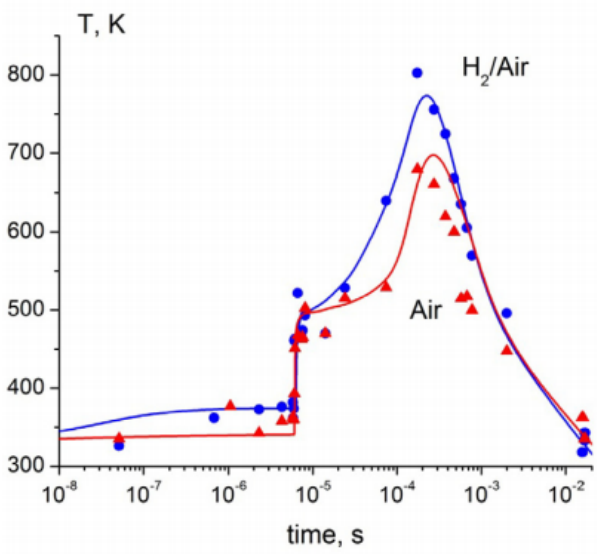


**Figure 1.8. Comparison of the time-resolved gas temperature inferred from pure rotational CARS spectra and predicted by kinetic modeling, along the centerline of a ns pulse discharge filament in 40 Torr of dry air and lean $H_2$ air mixture, during and after the discharge pulse. Symbols: experimental data, solid lines: modeling predictions [4].**

A more direct effect of $N_2$ vibrational excitation on plasma chemistry, either via reactions with $N_2(X^1\Sigma_g^+, v)$ as one of the reactants, or via vibrational energy transfer from nitrogen molecules to other reactive molecular species, has been a matter of some debate. The effect of $N_2(X^1\Sigma_g^+, v)$ molecules on nitric oxide formation in low-temperature glow discharges in air has been discussed in the literature extensively [15]. Direct measurements or high-fidelity theoretical predictions of rates of these reactions at low temperatures are not available. The principal difficulty in quantifying this effect is that it would require measurements of vibrational populations of the ground electronic state of nitrogen, e.g. by coherent anti-Stokes Raman Scattering (CARS) or by spontaneous Raman scattering [18 - 20], along with measurements of number densities of other reactants and products, such as

NO, O atoms, and N atoms. One recent example of such measurements is the use of simultaneous $N_2$ CARS, NO Laser Induced Fluorescence (LIF), and Two-Photon Absorption LIF (N and O TALIF) [15] to quantify the effect of reaction

$$N_2(X^1\Sigma_g^+,v) + O \rightarrow NO + N \qquad \text{(Equation 1.8)}$$

on the rate of NO formation in a low-temperature air plasma generated by a ns pulse discharge. At these conditions, the contribution of this reaction, compared to reactive quenching of excited electronic states of $N_2$,

$$N_2(A^3\Sigma_u^+, B^3\Pi_g, C^3\Pi_u, a^1\Sigma_u^-) + O \rightarrow NO + N \qquad \text{(Equation 1.9)}$$

appears to be minor. However, in quasi-steady state low-pressure plasmas sustained by DC or RF discharges, at considerably lower reduced electric fields, this reaction may well be one of the dominant channels of nitric oxide formation [15].

Another reaction pathway, hypothesized in Ref. [8], suggests that vibrationally excited nitrogen may delay OH recombination due to the near-resonance vibrational energy transfer to the relatively "unreactive" $HO_2$ radical,

$$N_2(X^1\Sigma_g^+,v=1) + HO_2 \rightarrow N_2(X^1\Sigma_g^+,v=0) + HO_2\ (\nu_2+\nu_3) \rightarrow N_2 + H + O_2 \qquad \text{(Equation 1.10)}$$

It was also suggested that this process may sustain chain propagation and chain branching chemical reactions of H atoms in the low-temperature afterglow in fuel-air mixtures, and thus extend OH radical lifetime. The underlying assumption of this hypothesis is that dissociation of $HO_2$ by vibrational energy transfer from $N_2$ would mitigate a major chain termination process during low-temperature oxidation of hydrogen. This would generate additional H atoms (see Equation 1.10), driving a well-known chain reaction process

$$H + O_2 \rightarrow OH + H, \qquad \text{(Equation 1.11)}$$

and

$$O + H_2 \rightarrow OH + O, \qquad \text{(Equation 1.12)}$$

and thus resulting in a higher transient OH number density. Recent time-resolved measurements of OH number density in ns pulse discharge afterglow in preheated atmospheric pressure hydrocarbon-air mixtures [16], which demonstrated anomalously long OH lifetime and its non-monotonous decay in the afterglow, seem to support this hypothesis. Figure 1.9 plots OH number density vs. time delay after the discharge pulse in several hydrocarbon mixtures, showing [OH] overshoot on a ms time scale. Kinetic modeling of atmospheric pressure hydrogen-air plasmas with significant initial vibrational excitation of nitrogen, $T_v$ ($N_2$) = 3000 K, incorporating the process of Equation 1.10, predicts that this effect would result in a transient OH number density rise in the afterglow, peaking on the time scale of ~ 300 μs – 4 ms at T = 600 - 800 K [8], as shown in Figure 1.7, consistent with the experimental data of Ref. [16].

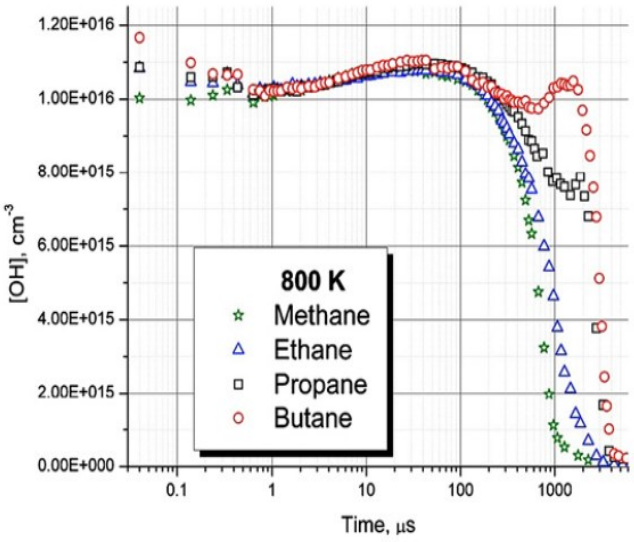


**Figure 1.9. OH evolution after the discharge pulse in lean hydrocarbon-air mixtures (equivalence ratio φ=0.1). P = 1 atm, initial temperature T = 800 K [16].**

In Ref. [17], it was pointed out that an increase in the OH decay time observed in Ref. [16] may also be caused by the gas heating due to vibrational relaxation of nitrogen by hydrogen or by hydrocarbons species. In fact, sustaining strong vibrational excitation in the late afterglow in $H_2$-air and hydrocarbon-air mixtures, without significant heating of the gas, appears unlikely due to heating caused by vibrational relaxation. Since the gas temperature and $N_2$ vibrational temperature in the experiments of Ref. [16] have not been measured, the effect of heating of the flow by the discharge on vibrational relaxation rate, chemical reaction rates, and OH lifetime in the afterglow cannot be ruled out. Direct vibrational temperature measurements at these conditions are critical due to the significant uncertainty in the state-specific rates of $N_2$ vibrational relaxation in reacting fuel-air mixtures.

Although it may well be possible that reactions of vibrationally excited $N_2$ molecules in fuel-air plasmas affect low-temperature fuel oxidation chemistry via reaction of Equation 1.10, as suggested in Ref. [8], additional experimental studies are needed to verify this conjecture. In this dissertation, $N_2$ vibrational CARS and OH LIF measurements are used (i) to determine time-resolved temperature and $N_2$ vibrational temperature, (ii) to monitor absolute, time resolved OH number density, and (iii) to detect a possible effect of $N_2$ vibrational excitation on OH kinetics in lean $H_2$-air afterglow plasmas sustained by a ns pulse discharge, at elevated gas temperatures and strong vibrational excitation. The approach employed in the present experiments is similar to that used previously, when a ns pulse, diffuse filament discharge in air was used to generate strongly nonequilibrium plasmas, up to T = 850 K and $T_v(N_2)$ = 4000 K at 1 atm [18-20] and up to T = 600 K and $T_v$ ($N_2$) = 3000 K at 100 Torr [3]. Kinetic modeling of a ns pulse discharge and the afterglow in $H_2$-air mixtures, using the model developed in Refs. [21, 22], is employed to interpret the experimental results.

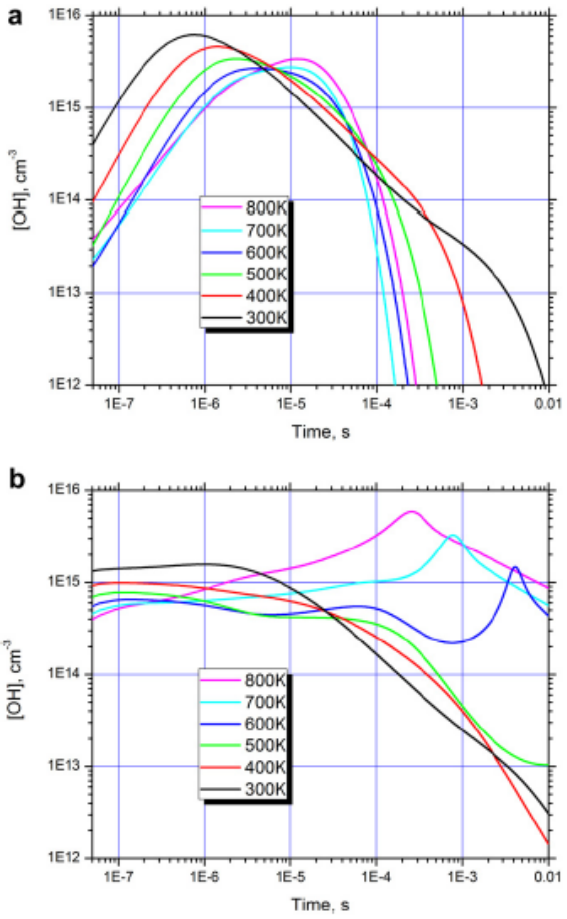


**Figure 1.10. Predicted OH number density in an atmospheric pressure 3% $H_2$-air mixture excited by a ns discharge pulse, at the initial temperature of 300 K. (a) "conventional" combustion chemistry, and (b) including $N_2$-$HO_2$ V-V' energy transfer, reaction of Equation 1.10 [8].**

### 1.5. Plasma-chemical Conversion of $CO_2$

Plasma chemical dissociation of carbon dioxide has been studied extensively [23-25], due to its significant potential for $CO_2$ emissions reduction and energy storage in $CO_2$ dissociation products (CO and $O_2$), with subsequent conversion to other chemical energy storage species such as syngas (CO / $H_2$ mixture) and hydrocarbons. Over the last decade, with the accelerated development of distributed, intermittent electrical power sources such as solar photovoltaic cells and wind turbines, as well as increasing concerns over the effect of $CO_2$ on global climate change, feasibility of the temporary storage of electrical power in $CO_2$ dissociation products has become a focus of intense study [24, 25].

Significant $CO_2$ dissociation in high-temperature, near thermal equilibrium plasmas, via the reactions

$$CO_2 + M \rightarrow CO + O + M, \ \Delta H = 5.5 \text{ eV/mol} \qquad \text{(Equation 1.13)}$$

$$O + O + M \rightarrow O_2 + M, \qquad \text{(Equation 1.14)}$$

require sustaining temperatures of T = 2500 - 3500 K. This is illustrated in Figure 1.11, plotting equilibrium composition of $CO_2$ vs. temperature at a pressure of 0.16 atm [23]. It can be seen that at T < 2000 K, mole fraction of CO and $O_2$ products do not exceed several percent. This requirement imposes significant engineering constraints on a plasma chemical reactor, which would need to operate at high temperatures and pressures, for an extended period of time.

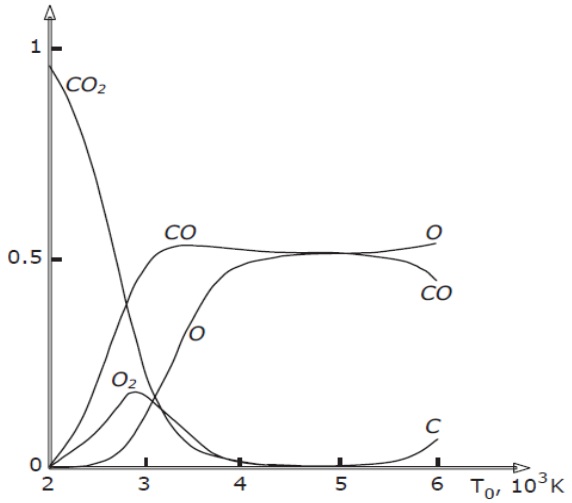


**Figure 1.11. Equilibrium mole fractions of products of $CO_2$ decomposition in a thermal plasma as functions of temperature, at a pressure of 0.16 atm [23].**

Another fundamental limitation on $CO_2$ dissociation in thermal plasmas is the energy cost. The enthalpy change in reaction of Equation 1.13 is very high, ΔH = 5.5 eV/molecule. Although the net energy cost of the process is somewhat lower due to the reaction of Equation 1.14 being exothermic, the enthalpy change for the net process,

$$CO_2 \rightarrow CO + \tfrac{1}{2}O_2, \qquad \Delta H = 2.9 \text{ eV/mol}, \qquad \text{(Equation 1.15)}$$

is still very significant, ΔH = 2.9 eV/molecule. The energy efficiency of $CO_2$ dissociation in an actual plasma chemical process is defined as the ratio of the reaction enthalpy and the actual energy cost per CO product molecule [23],

$$\eta = \Delta H / E_{CO} \qquad \text{(Equation 1.16)}$$

Theoretical maximum value for the efficiency of $CO_2$ dissociation in a thermal plasma is approximately 43-48%, with the maximum CO yield of 55% (see Figure 1.11) [1]. This value

represents a thermodynamic limit. Basically, the energy efficiency of this process in thermal plasmas is limited by the equipartition of energy among all molecular energy modes. Energy-efficient $CO_2$ dissociation in thermal plasmas also requires rapid cooling of the products, to reduce the effect of reverse reactions.

Note that CO generated by $CO_2$ dissociation in the plasmas can be also converted to hydrogen, in a reaction with water vapor,

$$CO + H_2O \rightarrow CO_2 + H_2, \Delta H = 2.5 \text{ eV/mol} \qquad \text{(Equation 1.17)}$$

with the net enthalpy change for the entire process (i.e. Equations 1.15 and 1.17)

$$CO_2 + H_2O \rightarrow CO + H_2 + \tfrac{1}{2} O_2 \qquad \text{(Equation 1.18)}$$

of $\Delta H$ = -0.4 eV/molecule. Contribution of reactions of Equations 1.15 and 1.17 results in a two-stage process producing hydrogen from water vapor with $CO_2$ recirculation.

Energy efficiency of $CO_2$ dissociation may be improved significantly if the discharge energy is channeled into the $CO_2$ vibrational energy modes, rather than partitioned equally among all molecular energy modes, as occurs in thermal plasmas. It is well known that in nonequilibrium plasmas in molecular gases such as $N_2$, CO, $CO_2$, and air, most of the discharge input energy (up to 80-90% at the electron temperature of 1-2 eV) goes to vibrational excitation by electron impact, over a wide range of parameters [1, 23]. This, along with the relatively slow vibrational relaxation, may result in sustaining strong vibrational nonequilibrium in $CO_2$, resulting in significant populations of high vibrational levels by anharmonic vibration-vibration (V-V) pumping [26] and in efficient dissociation from high vibrational levels,

$$CO_2\ (v_1, v_2, v_3) + M \rightarrow CO + O + M, \qquad \text{(Equation 1.19)}$$

where the total $CO_2$ vibrational energy would be above the dissociation limit of 5.5 eV. In addition, the O atom produced in the reaction of Equation 1.19 may react with another vibrationally excited $CO_2$ molecule

$$CO_2\ (v_1, v_2, v_3) + O \rightarrow CO + O_2 + M, \qquad \text{(Equation 1.20)}$$

producing a second CO molecule.

To illustrate this, Figure 1.12 shows discharge energy partition among different electron impact excitation channels in $CO_2$ plasma, plotted versus the reduced electric field E/N. It can be seen that over a wide range of E/N input energy fraction going to excitation of vibrational states of $CO_2$, is up to 90%.

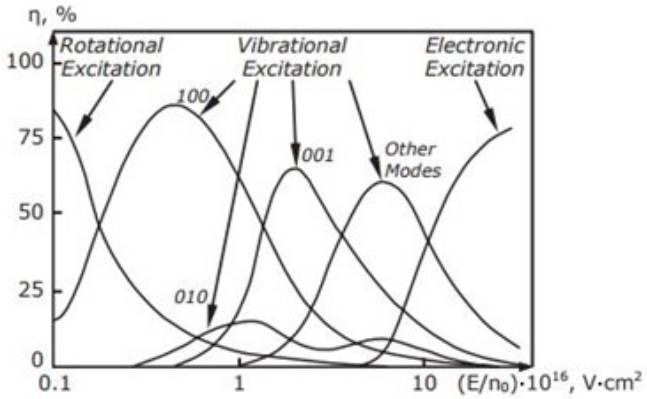


**Figure 1.12. Discharge energy partition among different molecular energy modes in $CO_2$ plasma [23].**

During the rapid anharmonic V-V up-pumping of $CO_2$,

$$CO_2 (v_1, v_2, v_3) + CO_2 (w_1, w_2, w_3) \rightarrow CO_2 (v_1, v_2, v_3\text{-}1) + CO_2 (w_1, w_2, w_3\text{+}1), \quad \text{(Equation 1.21)}$$

some of the $CO_2$ molecules obtain sufficient vibrational energy to reach the dissociation limit, resulting in efficient $CO_2$ dissociation (see Figure 1.13 (a)). Although intramolecular V-V energy transfer, e.g.

$$CO_2 (0, 0, 1) + CO_2 \rightarrow CO_2 (0, 1, 0) + CO_2, \quad \text{(Equation 1.22)}$$

and V-T relaxation of $CO_2$ bending mode,

$$CO_2 (0,1,0) + CO_2 \rightarrow CO_2 (0,0,0), \quad \text{(Equation 1.23)}$$

are relatively rapid (the rate coefficients for both processes at room temperature are $k_{VT} \sim 5 \cdot 10^{-15}$ $cm^3 \cdot s^{-1}$) [27], the characteristic time for $CO_2$ V-T relaxation in a nonequilibrium plasma remains much longer compared to the characteristic time for the anharmonic V-V pumping. Figure 1.13 (b,c) shows that $CO_2$ dissociation by electron impact, via excitation of electronic states, is less efficient compared to that via anharmonic V-V pumping, since some of the excitation energy is dissipated as heat.

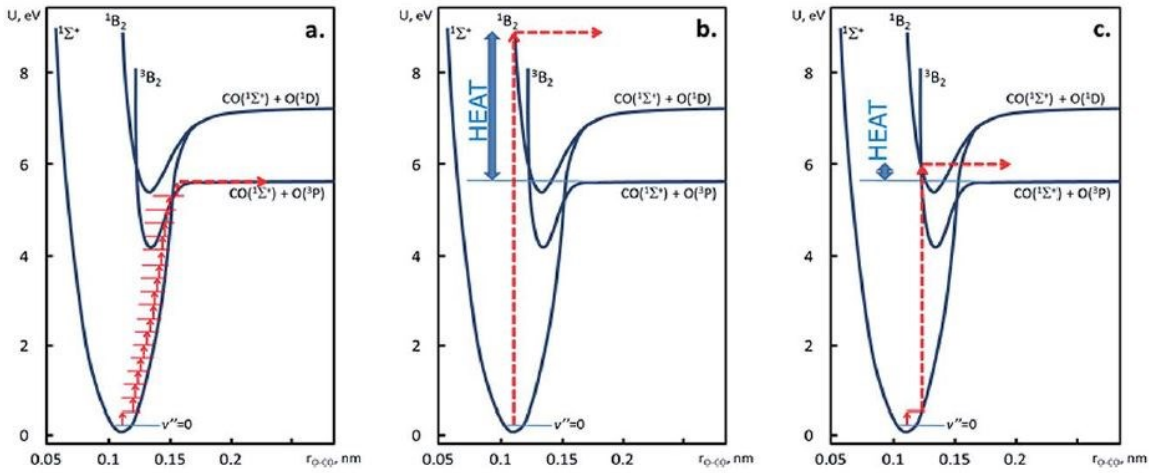


**Figure 1.13. $CO_2$ potential energy diagram as a function of C-O bond length, (a) V-V anharmonic up-pumping causing stepwise vibrational excitation and resulting in efficient $CO_2$ dissociation, (b) dissociation by electron impact via excitation of an electronic state, and (c) combination of mechanisms (a) and (b) [28].**

Therefore, operating an electric discharge at the reduced electric field value such that the fraction of input energy going to $CO_2$ vibrational excitation is high may significantly increase $CO_2$ dissociation energy efficiency.

However, operating the discharge at a high specific energy input may also result in significant temperature increase, which would dramatically accelerate the rate of V-T relaxation [27] and reduce vibrational nonequilibrium. Therefore, operation at strongly nonequilibrium conditions is critical for efficient dissociation of $CO_2$. $CO_2$ dissociation in electric discharge plasmas has been studied extensively in 1980s, demonstrating significant advantage of nonequilibrium discharges compared to high-temperature thermal plasmas. In 1977, it was shown that in atmospheric pressure, thermal equilibrium arc discharge, the energy efficiency of the process is only approximately 15% [23]. In low-pressure discharges,

specifically in a glow discharge, the energy efficiency is only ~8% [23]. In 1981, significantly higher energy efficiency was achieved in a pulsed microwave discharge and in a nonequilibrium RF discharge. In discharges sustained in fast subsonic and supersonic flows, the energy efficiency was shown to achieve 80 – 90 % [23], thus exceeding the thermodynamic limit for thermal equilibrium. As can be seen from Figure 1.14, both kinetic modeling calculations and experiments in nonequilibrium microwave discharges show $CO_2$ dissociation energy efficiency exceeding 80%, i.e. significantly higher compared to theoretical predictions and experimental data in near equilibrium thermal plasmas, such as in arc discharges. Based on these results, a microwave discharge plasma operated at strongly nonequilibrium conditions appears to be the most promising environment for energy-efficient $CO_2$ dissociation.

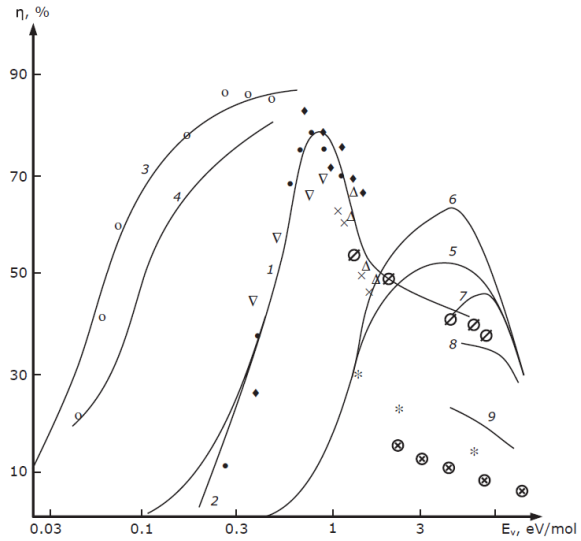


**Figure 1.14. Energy efficiency of $CO_2$ dissociation as a function of specific energy input (1, 2). Nonequilibrium calculations in one and two-temperature approximations; nonequilibrium calculations for supersonic flows, M =5 (3) and M = 3.5 (4); (5, 6) calculations of thermal dissociation with ideal (5) and super-ideal (6) quenching; (7-9) thermal dissociation with quenching rates $10^9$ K/s (7), $10^8$ K/s (8), and $10^7$ K/s (9). Experimental data in microwave discharge: ∘, ⧫, ×, Δ; in supersonic microwave discharge: • ; in RF discharge: ∇, ∅ ; in arc discharge: ⊗, ∗ [23].**

More recently, these promising results generated renewed interest in the use of microwave discharge plasmas for energy-efficient $CO_2$ dissociation. However, energy efficiency measured in recent experiments in a microwave discharge in pure $CO_2$, over a wide range of parameters, does not exceed 50% (see Figure 1.15), which is comparable with the results obtained in thermal plasmas (see Figure 1.14). This suggests that vibrational nonequilibrium in the discharge, at the conditions of Ref. [28], may not very significant. This demonstrates the need for additional characterization of high-pressure microwave plasmas such as used in these experiments.

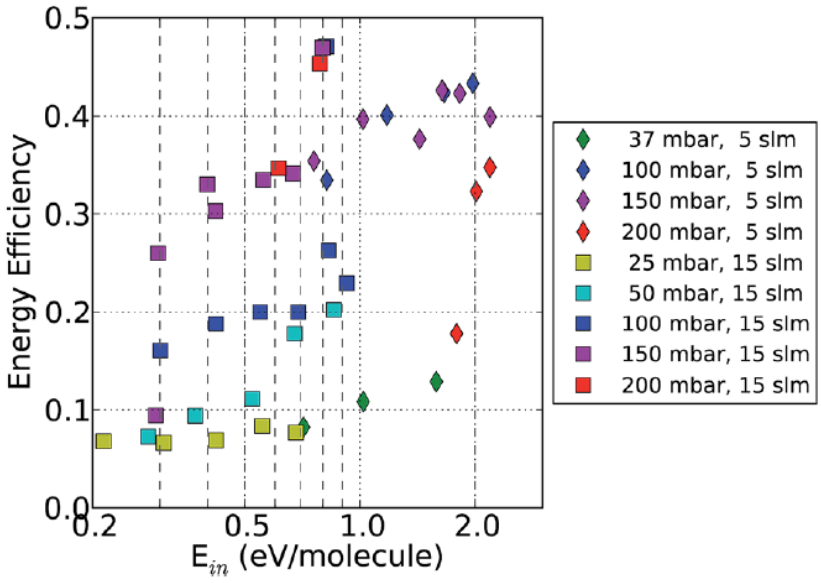


**Figure 1.15. Energy efficiency measured in a microwave plasma in pure $CO_2$ as a function of the specific energy input, at different flow rates and pressures [28].**

### 1.6. Measurements of Electric Field and Temperature Distributions in Flames

Knowledge of the reduced electric field in weakly ionized plasmas generated in reacting fuel-air mixtures and in flames is critical for understanding and quantifying the effect of strong electric fields on kinetics of excited species and radicals produced in the plasma, ignition, flameholding, flame stability, as well as for development of combustion control methods and plasma assisted combustion applications [8, 9]. As discussed above, in electric discharges sustained in fuel-air mixtures, reduced electric field waveform is well known to control the discharge energy partition among internal energy modes of molecules and atoms [1, 23], which is the dominant effect determining the rates of production of excited species and radicals by electron impact, as well as the rates of plasma chemical reactions [8]. In these environments, estimating the reduced electric field based on the

applied voltage waveforms, or predicting the electric field by solving the Poisson equation for the electric potential may result in significant uncertainty. Electric field distribution may be strongly perturbed by plasma self-shielding, which is controlled by ionization, electron-ion recombination, ion-molecule reactions, electron and ion transport, electron emission from electrodes, and surface charge accumulation on dielectric surfaces. In flames, externally applied electric field generates the ion wind, entraining the flow of neutral species, and affects the ion-molecule reaction chemistry. This has a strong effect on flame stability [8, 9], flashback [29], soot generation [30], and flow field in the reaction zone [31-34]. Understanding the kinetics of these processes and validation of high-fidelity modeling predictions require electric field measurements using accurate, non-intrusive experimental methods.

Determining the reduced electric field requires measurements of both the electric field and the temperature in the plasma. Two laser diagnostics techniques for electric field measurements in high-pressure plasmas developed over the last decade are ns / ps Four-Wave Mixing (FWM) [35-37], and fs / ps Second Harmonic Generation (SHG) [38, 39]. Both of these methods can have sub-ns temporal resolution, limited by the coherence decay time of molecules excited by the pump and probe beams (in four-wave mixing technique, which is similar to CARS), or by the duration of the laser beam (in second harmonic generation). Other advantages include straightforward absolute calibration and measurement of the individual components of the electric field vector with well-defined spatial resolutions. Note that second harmonic generation is essentially species independent [38] and can be used in different gas mixtures, while four-wave mixing requires the use of different wavelength Stokes beams for different probe species. In both methods, the spatial resolution along the

laser beams, determined by the Rayleigh range of the beams and the coherence length, may vary from ~ 1 mm [38] to several cm [36]. The spatial resolution in the direction perpendicular to the laser beam is on the order of the focused beam diameter ~ 100 μm.

Coherent anti-Stokes Raman Scattering (CARS) has been used for temperature and species concentration measurements in reacting flows and flames very extensively (e.g. see [40]. In this dissertation, ns broadband CARS, ps four-wave mixing, and ps second harmonic generation are used for measurements of temperature distribution and electric field in an atmospheric pressure hydrogen diffusion flame enhanced by dielectric barrier discharges (DBD) sustained by ns pulse and AC sine wave waveforms. Specifically, the temperature distribution inferred from CARS spectra is critical for the interpretation of electric filed measurements and determination of reduced electric field in the plasma.

### 1.7. Structure of the Dissertation

The following chapters of this dissertation are organized as follows: Chapter 2 presents a brief overview of Coherent Anti-Stokes Raman scattering (CARS) used for $N_2$ vibrational level populations and temperature measurements, and discusses advantages of CARS compared to spontaneous Raman scattering. Chapter 3 discusses $N_2$ vibrational temperature and translational-rotational temperature measurements in $N_2$, air and their mixtures with $CO_2$ and $H_2$, as well as OH number density measurements by laser induced fluorescence (LIF) in $H_2$-air mixtures. The main objectives of these measurements are two-fold: (a) demonstrate and quantify the effect of adding $CO_2$ to nitrogen and air on $N_2$

vibrational relaxation and energy thermalization rates in ns pulse discharge plasmas, for applications in high-speed flow control, and (b) determine if $N_2$ vibrational relaxation affects kinetics of radical species in low-temperature fuel-air mixtures excited by ns pulse discharge plasmas, for plasma-assisted combustion applications. The focus of Chapter 4 is on characterization of microwave discharges in $CO_2$ and $N_2$, to determine feasibility of their use for energy-efficient $CO_2$ dissociation. Chapter 5 discusses temperature and electric field measurements in atmospheric pressure hydrogen diffusion flames enhanced by ns pulse discharge and AC discharge plasmas, to provide insight into the mechanisms of excited species production and ion wind generation. Finally, Chapter 6 summarizes the results and discusses future work.

# Chapter 2. Overview of Coherent Anti-Stokes Scattering (CARS) Spectroscopy

## 2.1. Vibrational-rotational energy levels of diatomic molecules

In this dissertation, Q-branch $N_2$ Raman spectra are of the principal interest because their intensity is much higher compared to O-branch and S-branch spectra. Excluding electronic excitation, the energy of a diatomic molecule can be approximated as

$$E_{total} = E_{tr} + E_{int} \quad , \qquad \text{(Equation 2.1)}$$

where $E_{tr}$ is the translational energy, controlled by the gas temperature, and $E_{int}$ is the internal energy, including vibrational and rotational energies,

$$E_{int}(cm^{-1}) = \omega_e\left(v+\frac{1}{2}\right) - \omega_e\chi_e\left(v+\frac{1}{2}\right)^2 + B_v J(J+1) - D_v J^2(J+1)^2, \qquad \text{(Equation 2.2)}$$

where

$$B_v = B_e - \alpha_e\left(v+\frac{1}{2}\right) + \gamma_e\left(v+\frac{1}{2}\right)^2 + \cdots \text{ and } D_v = D_e + \beta_e\left(v+\frac{1}{2}\right) + \cdots \qquad \text{(Equation 2.3)}$$

In Equations 2.2, v is the vibrational quantum number, $\omega_e$ is the characteristic vibrational frequency, $\chi_e$ is the vibrational anharmonicity constant, J is the rotational quantum number, and $B_V$ and $D_v$ are the first-order and second-order rotational constants, respectively. In Equation 2.3, $B_V$ is the rigid-rotor rotational constant $B_e = \frac{h}{8\pi^2\mu r_e^2 c}$, and $D_V$ is the factor

describing the reduction of the effective rotational constant due to the centrifugal distortion of the internuclear distance, $D_e = \frac{4{B_e}^3}{{\omega_e}^2}$. For a nitrogen molecule, the term $D_v J^2(J+1)^2$ can be neglected in most cases, since nitrogen has a high chemical bond energy and centrifugal distortion is not a significant factor. In general, if the centrifugal distortion is neglected, using Raman selection rules for diatomic molecules in the Q branch, $\Delta v = \pm 1$ and $\Delta J = 0$, the anti-Stokes transition energy from state (v, J) to state (v+1, J) is

$$\Delta E(v+1, J \leftarrow v, J) = E(v+1, J) - E(v, J)$$

$$= [\omega_e\left(v+\frac{3}{2}\right) - \omega_e\chi_e\left(v+\frac{3}{2}\right)^2 + B_v''J(J+1)]$$

$$-[\omega_e\left(v+\frac{1}{2}\right) - \omega_e\chi_e\left(v+\frac{1}{2}\right)^2 + B_v'J(J+1)]$$

$$= \omega_e - 2\omega_e\chi_e(v+1) - (B_v' - B_v'')J(J+1) \qquad \text{(Equation 2.4)}$$

where $B_v'$ and $B_v''$ are the rotational constants for the higher and lower vibrational energy states, respectively. Using Equation 2.4, the theoretical energy spacing between two adjacent bands in the Q-branch CARS spectrum can also be calculated, such that

$$\Delta\omega_{CARS,vib} = \Delta E(v+1, J \leftarrow v, J) - \Delta E(v+2, J \leftarrow v+1, J)$$

$$= -2\omega_e\chi_e - J(J+1)(B_v' - B_v'') \approx -2\omega_e\chi_e \qquad \text{(Equation 2.5)}$$

The second term in Equation 2.5, $J(J+1)(B_v' - B_v'')$, can be neglected since $\omega_e\chi_e \gg B_v'$, $B_v''$. Thus, vibrational bands of $N_2$ in Q branch CARS spectra are evenly spaced by $2\omega_e\chi_e$, with transition energy decreasing as the vibrational quantum number increases. For

nitrogen molecules, the spacing between two adjacent vibrational states is, $\Delta\omega_{\mathrm{CARS,vib}} \approx 28.648\ \mathrm{cm}^{-1}$.

If the spectral resolution is sufficiently high, individual rotational transitions within the v = 0 band can also be resolved. The theoretical rotational line spacing for the Q-branch anti-Stokes series within the v=0 band can be represented as

$$\Delta\omega_{CARS.rot} = \Delta\mathrm{E}(\mathrm{v}=1,\mathrm{J} \leftarrow \mathrm{v}=0,\mathrm{J}) - \Delta\mathrm{E}(v=1,\mathrm{J}+1 \leftarrow \mathrm{v}=0,\mathrm{J}+1)$$

$$= -2\mathrm{B_v}'(\mathrm{J}+1) \qquad \text{(Equation 2.6)}$$

Thus, the energy spacing between the rotational lines increases as J increases. By fitting the rotational structure of an experimental CARS spectrum with a theoretical synthetic spectrum, also predicting the rotational line intensities, the rotational temperature of the gas can be inferred. The synthetic spectrum used for this purpose and the temperature inference will be discussed in greater detail in the next chapter.

For $N_2$, $\omega_\mathrm{e} = 2358.57\ \mathrm{cm}^{-1}$, $\omega_\mathrm{e}\chi_\mathrm{e} = 14.324\ \mathrm{cm}^{-1}$, and $\mathrm{B}_\mathrm{v}' = 0.0173\mathrm{cm}^{-1}$, such that $\omega_\mathrm{e} \gg \omega_\mathrm{e}\chi_\mathrm{e} \gg \mathrm{B_v}'$ [41]. Table 2.1 lists Raman shift values for several vibrational bands of $N_2$, along with corresponding Stokes and anti-Stokes wavelengths, assuming that both the pump and the probe beams have the wavelength of 532 nm.

| Vibrational quantum number | Raman Shift [$cm^{-1}$] | Stokes wavelength [nm] | Anti-Stokes wavelength [nm] |
|---|---|---|---|
| **0** | 2329.92 | 607.27 | 473.33 |
| **1** | 2301.27 | 606.22 | 473.97 |
| **2** | 2272.63 | 605.17 | 474.62 |
| **3** | 2243.98 | 604.12 | 475.26 |
| **4** | 2215.33 | 603.08 | 475.91 |

**Table 2.1. Raman shift, Stokes wavelength, and anti-Stokes wavelength for several vibrational bands of $N_2$ [42].**

### 2.2. Vibrational-rotational Energy Levels of Carbon Dioxide

$CO_2$ is a linear triatomic molecule and has three normal vibrational modes denoted as $CO_2(\omega_1, \omega_2^l, \omega_3)$, such that the vibrational energy of a $CO_2$ molecule can be expressed as follows,

$$CO_2(\omega_1, \omega_2^l, \omega_3)(cm^{-1}) = \omega_1\left(v_1 + \frac{1}{2}\right) + \omega_2^l(v_2 + 1) + \omega_3\left(v_3 + \frac{1}{2}\right)$$

$$+x_{11}\left(v_1 + \frac{1}{2}\right)^2 + x_{22}(v_2 + 1)^2 + x_{33}\left(v_3 + \frac{1}{2}\right)^2 + x_{12}\left(v_1 + \frac{1}{2}\right)(v_2 + 1)$$

$$+x_{13}\left(v_1 + \tfrac{1}{2}\right)\left(v_3 + \tfrac{1}{2}\right) + x_{23}(v_2 + 1)\left(v_3 + \tfrac{1}{2}\right) + g_{22}l^2 \qquad \text{(Equation 2.7)}$$

In Equation 2.7, $\omega_1$ is the symmetric stretch vibrational frequency and $\omega_3$ is the asymmetric stretch vibrational frequency. $\omega_2^l$ is the vibrational frequency of a double degenerate deformation (bending) mode . $l$ is the quantum number for angular momentum about the internuclear axis for the bending mode. In Equation 2.7, $x_{11} = -3.79\ \mathrm{cm}^{-1}$, $x_{22} = -0.65\ \mathrm{cm}^{-1}$, $x_{33} = -12.90\ \mathrm{cm}^{-1}$, $x_{12} = 3.63\ \mathrm{cm}^{-1}$, $x_{13} = -19.36\ \mathrm{cm}^{-1}$, $x_{23} = -12.90\ \mathrm{cm}^{-1}$ are the vibrational anharmonicity coefficients [23]. The last term describes the contribution of the angular momentum induced by the double-degenerate bending mode vibrational motion into the total energy, with the coefficient $g_{22} = 0.08\ \mathrm{cm}^{-1}$, and can be neglected when $l < 5$ [23].

Since CARS is a Raman scattering technique, only the symmetric stretch vibrational mode of $CO_2$, which has a non-zero Raman cross section, can be probed. For this mode, the transition energy from the first excited vibrational state, $CO_2$ (1,0,0), to the ground state, $CO_2$ (0,0,0) can be simplified to

$$\mathrm{CO_2}(0,0,0 \leftarrow 1,0,0)(\mathrm{cm}^{-1}) \approx \omega_1\left(1+\frac{1}{2}\right) + x_{11}\left(1+\frac{1}{2}\right)^2 - \omega_1\left(0+\frac{1}{2}\right) - x_{11}\left(0+\frac{1}{2}\right)^2$$
$$= \omega_1 + 2x_{11}, \qquad \text{(Equation 2.8)}$$

assuming that there are no coherent Raman scattering transitions in the other two vibrational modes. The Raman shift for $CO_2$ (1,0,0 → 0,0,0) transition is 1389 $cm^{-1}$.

## 2.3. Brief Overview of CARS Theory and Background

Coherent Anti-Stokes Raman Spectroscopy (CARS) is a four-wave mixing technique used for measurements of temperature, vibrational level populations, and species concentrations in reacting gas mixtures, non-equilibrium high-speed flows, and non-equilibrium plasmas. When three input laser beams are focused to overlap at the focal point, using proper spatial alignment, a coherent laser-like output signal beam is generated.

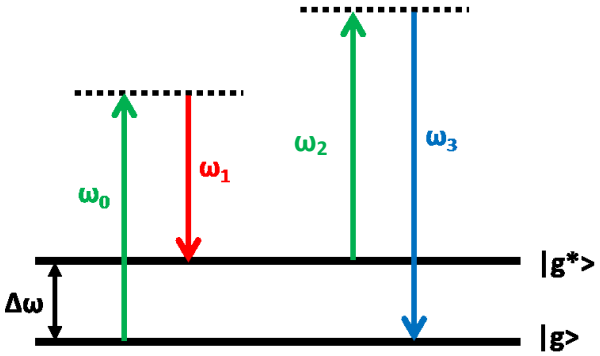


**Figure 2.1. Energy diagram of coherent anti-Stokes scattering.**

There are two two-photon steps involved in CARS diagnostics. The first step occurs when the pump and Stokes beam photons interact with the target molecule. By choosing the frequency of the pump beam, $\omega_0$, and of the Stokes beam, $\omega_1$, the energy difference between them, $\Delta\omega = \omega_0 - \omega_1$, can match the vibrational/rotational energy spacing of the target molecule and cause a coherent resonance in molecular electron orbitals (oscillating nonlinear polarization of the medium). In the second step, the third beam, the probe beam with frequency $\omega_2$, is used to generate Raman scattering from the coherent resonance of the

target molecule that is generated during the previous step. Due to the well-established phase relationship between all three incident beams, the resonance oscillation of the molecular electron cloud (i.e. polarization) generates coherently oscillating dipoles with the frequency $\omega_3 = \omega_2 + \Delta\omega = \omega_2 + \omega_0 - \omega_1$. During the scattering process, the oscillating dipoles emit anti-Stokes photons with the frequency $\omega_3$, in the direction determined by the photon phase matching (momentum conservation). Figure 2.1 shows the energy diagram of the CARS process. In CARS measurements, usually the same Nd:YAG laser is used to generate both the pump and the probe beams, although it is not necessary for the pump and probe beam to have the same frequency. The Stokes beam may be produced by a narrowband tunable dye laser (for scanning CARS spectra), or by a broadband dye laser, with the output spectrum chosen by using an appropriate mixture of laser dyes (for broadband CARS spectra).

The theoretical basis of CARS can be explained by the classical polarization theory. The starting point is the wave equation for the electric field

$$\nabla^2\vec{E} - \frac{1}{c^2}\frac{\partial^2\vec{E}}{\partial t^2} = \mu_0\frac{\partial^2\vec{P}}{\partial t^2}, \qquad \text{(Equation 2.9)}$$

where $\vec{E}$ and induced polarization $\vec{P}$ of the medium are sums of waves with various frequencies participating in the system. In an oscillating field, both $\vec{E}$ and $\vec{P}$ have time dependence on $e^{-i\omega_i t}$, such that the wave equation can be rewritten as

$$\nabla^2\vec{E}(\omega_i,\vec{r}) + \frac{\omega'^2}{c^2}\vec{E}(\omega_i,\vec{r}) = -\mu_0\omega'^2\vec{P}(\omega_i,\vec{r}) \qquad \text{(Equation 2.10)}$$

As the applied filed is increased, the induced polarization $\vec{P}$ is no longer linearly dependent on $\vec{E}$. The response of $\vec{P}$ in strong fields is generally described by a powers series of $\vec{E}$,

$$\vec{P} = \epsilon_0\left[\chi^{(1)}\vec{E} + \chi^{(2)}\vec{E}^2 + \chi^{(3)}\vec{E}^3 + \cdots\right], \qquad \text{(Equation 2.11)}$$

where $\chi^{(i)}$ are i-th order susceptibilities. Because of the inversion symmetry in the isotropic medium, all $\chi^{(even)}$ are equal to zero, leaving

$$\vec{P} \backsimeq \epsilon_0\left[\chi^{(1)}\vec{E} + \chi^{(3)}\vec{E}^3\right] = \vec{P}^{(1)} + \vec{P}^{(3)} \qquad \text{(Equation 2.12).}$$

Since we are interested only in the CARS signal with frequency $\omega_3$ (see Figure 2.1), the components of $\vec{P}^{(3)}$ for CARS can be written as

$$P_i^{(3)}(\omega_3) = \epsilon_0\chi_{ijkl}^{(3)}(\omega_3, \omega_0, \omega_1, \omega_2)\vec{E}_j(\omega_0, \vec{r})\vec{E}_k(\omega_1, \vec{r})\vec{E}_l(\omega_2, \vec{r}), \qquad \text{(Equation 2.13)}$$

where i is the polarization direction of the signal beam, and j, k, l, are the Cartesian indices indicating the three polarization directions (x, y, or z) of the incident beams (pump, Stokes, and probe). Consider the case when the pump and the probe beams have the same wavelength, i.e. $\omega_0 = \omega_2$ and $k_0 = k_2$. Substituting Equation 2.13 into Equation 2.10, and solving the wave equation, one can get the solution for $\vec{E}_{CARS}$, controlling the intensity of the CARS beam. The intensity of CARS, $I_{CARS}$, is proportional to $\left|\overrightarrow{E_{CARS}}\right|^2$, and is given as

$$I_{CARS} = \frac{{\omega_3}^2}{{n_0}^2 n_1 n_3 c^4 {\epsilon_0}^2} {I_0}^2 I_1 |\chi_{CARS}|^2 l^2 \left[\frac{\sin\left(\frac{\Delta k l}{2}\right)}{\frac{\Delta k l}{2}}\right]^2, \qquad \text{(Equation 2.14)}$$

where $n_i$ is the refraction index of a wave with the frequency of $\omega_i$; $\Delta k = 2\vec{k}_0 - \vec{k}_1 - \vec{k}_3$ is the phase-matching factor controlling coherent growth of the second harmonic signal due to constructive interference, discussed in Section 2.4; $\vec{k}_0, \vec{k}_1, \vec{k}_3$, are the wave vectors of pump/probe, Stokes, and CARS signal beam, respectively, and *l* is the length of interrogation region. From Equation 2.14, it can be seen that the signal intensity is maximized if $\Delta k = 0$. Using the derivation in Reference [42], the resonant CARS susceptibility $\chi_{CARS}$ can be expressed as

$$\chi_{CARS} = \frac{4\pi^2 \epsilon_0 c^4 (N_{g*} - N_g)}{\hbar {\omega_2}^4} \left(\frac{\partial \sigma}{\partial \Omega}\right) \frac{\omega_v}{[{\omega_v}^2 - (\omega_0 - \omega_1)^2 + i(\omega_0 - \omega_1)\Gamma]} \qquad \text{(Equation 2.15)}$$

In Equation 2.15, $\left(\frac{\partial \sigma}{\partial \Omega}\right)$ is the Raman cross section of the target species, $\omega_v$ is resonant frequency of molecule, and $N_{g*}$ and $N_g$ are populations of the higher and the lower states, g* and g, respectively (see Figure 2.1). For $N_2$ vibrational states, the Raman cross section is proportional to the vibrational quantum number, $v + 1$. Since $\chi_{CARS}$ is proportional to the population difference, $N_{g^*} - N_g$, the CARS signal intensity is quadratically proportional to $N_{g^*} - N_g$, such that CARS measurements become challenging at low pressures.

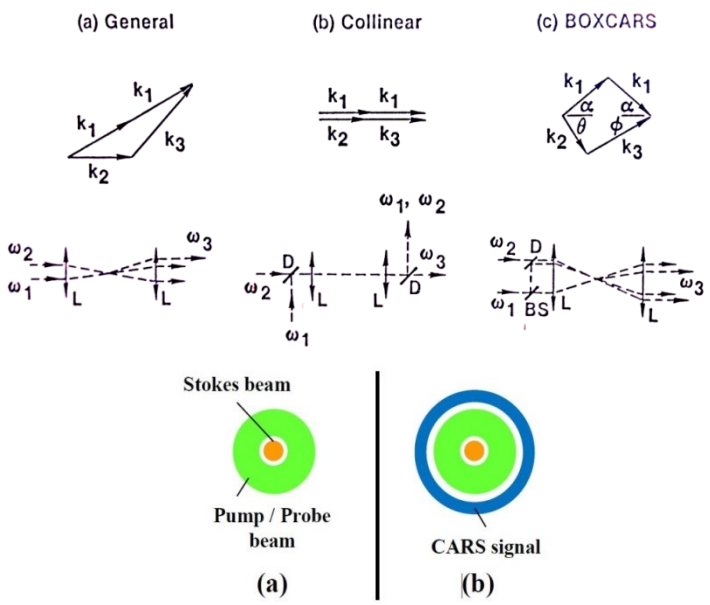


**Figure 2.2. Top: phase matching schemes for collinear CARS and BOX-CARS. Bottom: phase-matching diagram for USED-CARS.**

### 2.4. CARS Phase Matching

Phase-matching is an important factor to be considered in the CARS experiment. In order to have efficient signal generation, the three input beams should be aligned properly at the focal point. Three different phase-matching geometries are frequently used: collinear, BOX-CARS, and USED-CARS (Unstable-resonator Spatially Enhanced Detection CARS), illustrated in Figure 2.2. The collinear phase-matching geometry has the simplest alignment. Note that the photon energy conservation, $\omega_3 = 2\omega_0 - \omega_1$(see Figure 2.1), and the photon momentum conservation,$\Delta k = 2\overrightarrow{k_0} - \overrightarrow{k_1} - \overrightarrow{k_3} = 0$ (see Figure 2.2), cannot be satisfied simultaneously due to the dependence of the index of refraction of the medium on the frequency,

$$\Delta k = 2k_0(\omega_0) - k_1(\omega_1) - k_3(\omega_3) = \frac{2\omega_0 \cdot n(\omega_0) - \omega_1 \cdot n(\omega_1) - \omega_3 \cdot n(\omega_3)}{c}$$

(Equation 2.16)

where $n(\omega_i), i = 0, 1, 3$ is the refraction index at the frequency of pump/probe, Stokes, and anti-Stokes beams. At the present experimental conditions, the signal coherence length which controls the range of the coherent growth of the CARS signal, $L_c = \pi/\Delta k \sim 7$ cm, is much larger compared to the region probed by CARS. Therefore the spatial distribution of the CARS signal, as well as the length of the measurement volume are controlled by the intensities of the pump/probe and Stokes beams. Thus, the region where the CARS signal is generated (i.e. the spatial resolution of the measurements in the direction of the laser beam) is limited by the confocal parameter of the lens, $b = 2z_R$, where $z_R = \pi\omega_0/\lambda$ is the beam Rayleigh range, defined as the distance from the focal point where the beam waist $w(z) = w_0/[1 + z/z_g]^{1/2}$, increases by a factor of $\sqrt{2}$ (see Figure 2.3). In practical terms, the spatial resolution of the measurements is inversely proportional to the focal distance of the focusing lens, which controls the beam angular spread. The use of a shorter focal distance lens improves the spatial resolution but reduces the intensity of the CARS signal, accumulated over the confocal parameter of the lens.

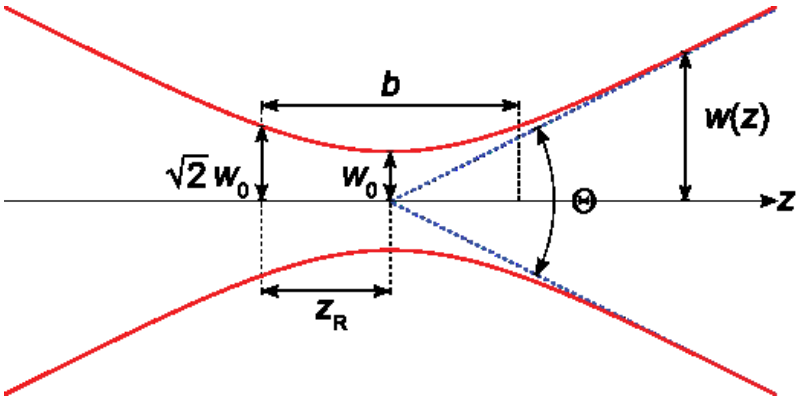


**Figure 2.3. Gaussian beam width as a function of the axial distance, w(z). $w_0$ is the beam waist, b is the confocal parameter, $z_R$ is the Rayleigh range and Θ is total angular spread. Figure taken from Wikipedia.**

Thus, the main advantages of collinear CARS are potentially much higher signal level due to the longer probing volume as well as relatively simple optical setup. Therefore, it has significant potential for probing non-equilibrium environments that do not have significant gradients in the direction of the laser beam. For BOX-CARS, there are many different alignment geometries. For example, folded BOX-CARS, which features folding of the phase-matching plane, gives better spatial resolution due to a much shorter laser beam overlap region (< 1 mm). However, the alignment of optical elements is considerably more difficult compared to collinear CARS. With much smaller interrogation volume, the signal level for BOX-CARS is much lower and is not suitable for measurements in low-pressure, high temperature environments. USED-CARS geometry is relatively simple to set up, and is particularly applied in automotive measurements in unstable resonator cavities, due to its insensitivity to refraction index variation during combustion tests [43].

## 2.5. Spectral Resolution and Injection Seeding

CARS spectral resolution is determined by the pump/probe and Stokes beam linewidth, as well as by the instrument function (i.e. the spectrometer slit width and the diffraction grating resolution). In the present experiments, Nd:YAG laser injection seeding is used to improve the CARS spectral resolution by dramatically reducing the pump/probe beam linewidth.

Injection seeding is an optical technique that is applied to pulsed lasers or optical parameter oscillators to achieve a narrow output linewidth. Usually, a single-frequency, low power, narrow linewidth laser is used as the seed laser. Without injection seeding, a pulsed laser emits on multiple resonant modes during operation, which have optical gain of comparable magnitude. The output from the seed laser has the frequency close to one of the resonant modes, and is acting as the "seed" to make that particular resonant mode dominating in the laser cavity. As a result, the emission bandwidth of the pulsed laser can be reduced significantly, compared to a "free-running" laser (without injection seeding). Additional experimental details on injection seeding will be discussed in Chapter 3.

## 2.6. Non-resonant signal (NRS) and CARS Spectra Processing Procedure

To determine the spectral output of the Stokes beam generated by the broadband dye laser, the non-resonant signal (NRS) from the discharge cell filled with argon has been measured. For this, the test cell was first evacuated, flushed with argon flow for several minutes to remove the residual air impurity, and then filled by argon to a pressure of 300 Torr. Argon is chosen for NRS measurement because it is a monatomic gas and therefore does not have vibrational or rotational CARS spectra. The raw NRS spectrum, plotted using symbols in Figure 2.4, was accumulated over 3000 laser shots. The peak near 473.3 nm is produced by a small amount of residual $N_2$ molecules remaining in the test cell, and is ignored when calculating a running average fitting curve, which is used for the CARS data reduction. This fitting curve is obtained by smoothing the raw NRS spectrum using a running average over a spectral interval of 0.29 nm. The locations of the $N_2$ vibrational band centers are also indicated in Figure 2.4 (see also Table 2.1). It can be seen that using the present dye mixture, $N_2$ vibrational levels v=0-4 can be detected in the CARS spectra.

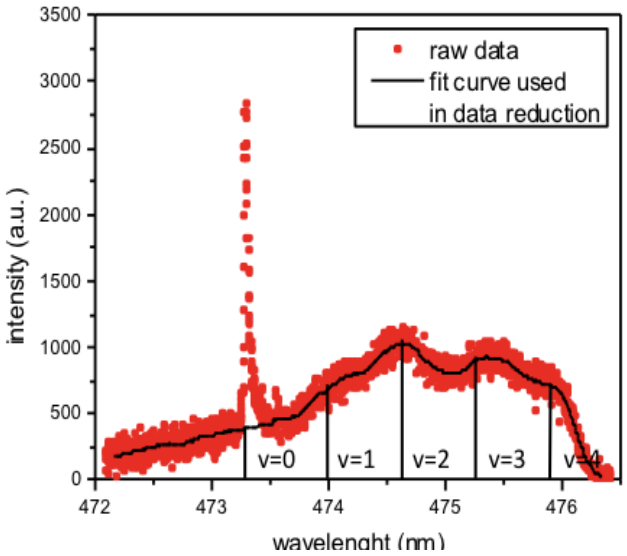


**Figure 2.4. Non-resonant background signal obtained from 300 Torr of argon using the broadband dye laser, plotted along with the locations of first five $N_2$ vibrational bands.**

In the present experiments, CARS diagnostics is used for the measurements of vibrational populations of $N_2$ and rotational-translational temperature in nonequilibrium, chemically reacting environments. Data reduction procedures used to infer vibrational level population from the CARS spectra is as follows. The first step is background subtraction, to remove the effects of stray light and camera dark current. The background is taken at the same experimental conditions, but with the Stokes beam blocked. After subtracting the background, the following step is to check if the spectrum baseline is at zero. Since the conditions for acquiring the background are slightly different from run to run, even for the same integration time, due to the drift of CCD camera dark current, it is necessary to shift the spectrum to the non-zero baseline manually.

In order to obtain the $N_2$ vibrational distribution function (VDF) and to calculate the vibrational temperature $T_V$, relative populations of each vibrational level are inferred from the spectrum. As can been seen from Equation 2.14, the CARS signal is proportional to the square of CARS susceptibility, $\chi_{CARS}$, and Equation 2.15 shows that $\chi_{CARS} \propto (N_{g^*} - N_g)\left(\frac{\partial\sigma}{\partial\Omega}\right)$. In other words, $I_{CARS} \propto (N_{g^*} - N_g)^2\left(\frac{\partial\sigma}{\partial\Omega}\right)^2$. After the background subtraction, the experimental spectrum is rescaled by the NRS spectrum taken in argon, to account for the spectral distribution of the broadband Stokes beam. After this, a square root of the intensity is taken and the spectrum is normalized. At this point, the normalized intensity is proportional to the difference in the vibrational level populations times the Raman cross section, $I_{CARS}' \propto (N_{g^*} - N_g)\left(\frac{\partial\sigma}{\partial\Omega}\right)$. To obtain the populations of the vibrational states, the area under each vibrational band of the processed CARS spectrum is integrated and divided by v+1, to account for the scaling of the Raman cross section with the vibrational quantum number. These results in the following set of linear equations,

$$S_0 = A \cdot (N_0 - N_1),$$

$$S_1 = A \cdot (N_1 - N_2),$$

$$S_2 = A \cdot (N_2 - N_3), \ldots$$

$$S_v = A \cdot (N_v - N_{v+1}) \qquad \text{(Equation 2.17)}$$

where $S_i$ are the integrated band signal intensities, $N_i$ are the vibrational level populations, A is a constant incorporating parameters such as efficiency of CARS signal collection, CCD camera quantum yield, etc., and v is the highest vibrational state detected. Clearly,

$$N_0 \approx (S_0 + S_1 + S_2 + \ldots S_v)/A,$$

$$N_1 \approx (S_1 + S_2 + \dots S_v)/A,$$

$$N_2 \approx (S_2 + \dots S_v)/A, \dots$$

$$N_v \approx S_v/A \qquad \text{(Equation 2.18)}$$

and

$$N_1/N_0 \approx (S_1 + S_2 + \dots S_v) \,/\, (S_0 + S_1 + S_2 + \dots S_v),$$

$$N_2/N_0 \approx (S_2 + \dots S_v) \,/\, (S_0 + S_1 + S_2 + \dots S_v), \dots$$

$$N_v/N_0 \approx S_v \,/\, (S_0 + S_1 + S_2 + \dots S_v) \qquad \text{(Equation 2.19)}$$

Finally, after normalization, the relative populations of the vibrational levels at $v > 0$ are calculated as follows,

$$f_i = \frac{N_i/N_0}{\sum N_i/N_0}, \; i = 1, 2 \dots \qquad \text{(Equation 2.20)}$$

# Chapter 3. Vibrational Energy Transfer in a "Diffuse Filament" Ns Pulse Discharge in Nitrogen, Air, and Their Mixtures with Carbon Dioxide and Hydrogen

## 3.1. Introduction

The main objectives of the experiments and kinetic modeling calculations discussed in this chapter are as follows. The first objective is to show that strong transient vibrational nonequilibrium can be generated in a high-specific energy loading, "diffuse filament" ns pulse discharge generated in nitrogen and air. The second objective is to demonstrate that the degree of vibrational nonequilibrium in the discharge and the afterglow, as well as the rate of heating in the afterglow, can be controlled and manipulated by adding carbon dioxide, a rapid relaxer species, to the gas mixture. These experiments provide quantitative insight into the kinetics of molecular energy transfer processes and the rate of energy thermalization in air flows in the presence of species accelerating vibrational relaxation of nitrogen, such as $CO_2$ or water vapor. The main application of these studies is the development of high-speed flow control methods using plasma actuators generating localized thermal perturbations in the flow. Specifically, the efficiency of these actuators and the flow control authority are determined by the rate of heating of the flow in the plasma.

The third objective of the present experiments is to demonstrate that strong vibrational nonequilibrium in a ns pulse discharge plasma and afterglow can also be generated in mixtures of air and hydrogen. Although kinetics of low-temperature plasma chemical reactions and ignition in hydrogen-air mixtures have been studied extensively, the

effect of vibrationally excited nitrogen molecules on reactions of radical species, such as OH, remains not well understood. In particular, it has been suggested recently [8] that vibrationally excited nitrogen may delay OH recombination, due to the near-resonance vibrational energy transfer to relatively "unreactive" $HO_2$ radical, resulting in its dissociation,

$$N_2(X^1\Sigma, v = 1) + HO_2 \rightarrow N_2(X^1\Sigma, v = 0) + HO_2\ (\nu_2+\nu_3) \rightarrow N_2 + H + O_2 \qquad \text{(Equation 3.1)}$$

This process may sustain chain propagation and chain branching chemical reactions of H atoms in low-temperature afterglow in fuel-air mixtures, and thus extend OH radical lifetime. The implication of this process is that dissociation of $HO_2$ by vibrational energy transfer from $N_2$ would mitigate a major chain termination process during the low-temperature oxidation of hydrogen, $H + O_2 + M \rightarrow HO_2 + M$. This would generate additional H atoms, driving a well-known chain reaction process, $H + O_2 \rightarrow OH + H$ and $O + H_2 \rightarrow OH + O$, and thus resulting in a higher transient OH number density and more rapid fuel oxidation.

Therefore the fourth objective of the present work is to determine whether vibrational excitation of nitrogen affects reaction kinetics of a dominant radical species, OH. For this, CARS measurements of $N_2$ vibrational temperature and rotational-translational temperature (the results of this work) are complemented by OH number density measurements by LIF (done in a separate study in the same discharge cell and at the same experimental conditions [44]) and by kinetic modeling calculations at the present experimental conditions [45].

### 3.2. Discharge Test Cell and Electrode Assembly

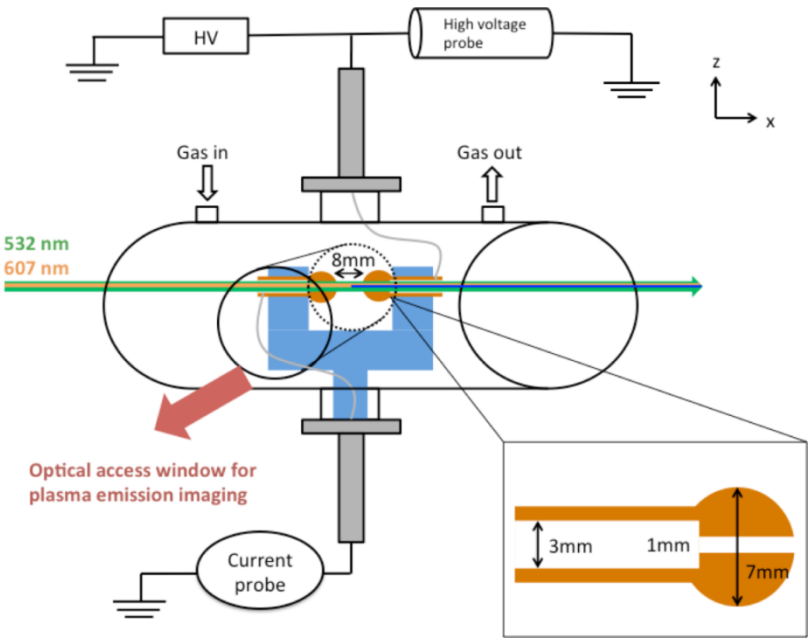


**Figure 3.1. Schematic diagram of the six-arm cross discharge test cell with BK7 glass and fused silica optical access windows. The 532 nm beam and the 607 nm beam are focused halfway between the two electrodes, generating CARS signal in gas mixtures in the cell.**

The electric discharge test cell is a six-arm cross glass cell with two 3" inner diameter arms in the x direction, two 2" inner diameter arms in the y-direction, and two 1" inner diameter arms in the z direction, as shown in Figure 3.1. Both the 3" arms and the 2" arms have optical access windows. Both 1" arms are equipped with high-voltage feed-throughs, one connected to the high voltage terminal of a ns pulse generator and the other is grounded. A high voltage probe (Tektronix P6015A) is connected to the high-voltage side, and a current probe (Pearson Electronics wideband current monitor) is connected to the ground side, to measure the discharge pulse voltage and current, monitored by an

oscilloscope (Agilent DSO-X-4032A). The BK-7 glass windows in the 3" arms of the test cell are used to provide optical access for the pump and Stokes beams, as well as for the CARS signal beam during the CARS measurements (discussed in Section 3.4.3), while the fused silica windows in the 2" arms provide optical access for plasma imaging (discussed in Section 3.3). A U-shaped electrode holder machined from macor ceramic, with the dimensions of 1.4"x1.3"x0.8", is placed at the center of the discharge cell. Two ¼" diameter holes are drilled in the electrode holder to hold the discharge electrodes, as shown in Figure 3.1. Two spherical electrodes 7 mm in diameter, made of copper, are separated by an 8 mm gap and connected to two hollow copper cylinders 16 mm long and ¼" in diameter, with an inner diameter of 3.5 mm. A 1 mm diameter hole is drilled through each electrode, along the centerline, and the electrodes are aligned to allow optical access for the pump and Stokes laser beams, as well as the CARS signal beam (for $N_2$ vibrational temperature and gas temperature measurements, discussed in Section 3.5), and for the LIF pump beam (for OH number density measurements, see Section 3.6) (see Figures 3.2 and 3.3). The discharge cell is mounted on a three-dimensional translation stage, such that it can be adjusted to the desired location during the alignment of the laser beams.

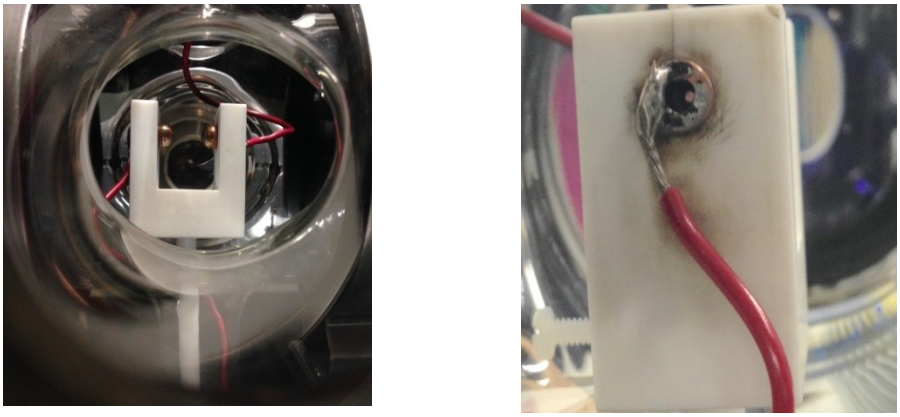

**Figure 3.2. Left: Photograph of the discharge electrodes and the electrode holder, taken through the optical access window in the 2" diameter arm. Right: photograph of a 1 mm diameter hole drilled through the electrode to provide optical access for the laser beams, taken through the optical access window in the 3" diameter arm.**

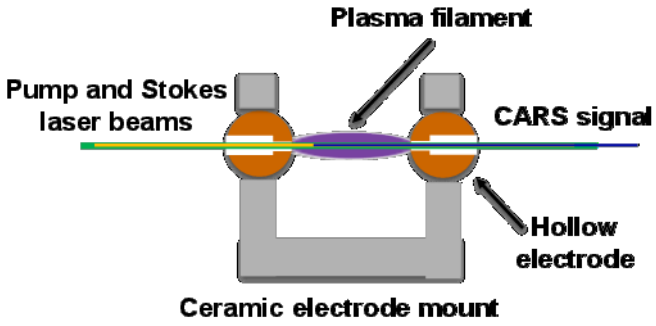


**Figure 3.3. Schematic of the discharge electrode assembly and optical access in the diffuse filament discharge test cell.**

In the present work, the total pressure in the discharge cell is 100 ± 1 Torr. After the test cell is evacuated by a Dayton 3K211 vacuum pump, the gas mixtures (nitrogen, dry air, or their mixtures with carbon dioxide or hydrogen) are flown through the cell at the flow rate of 1.1±0.1 SLM. The velocity through the cell is approximately 3.4 cm/s at room temperature, assuming that the test cell is a 3" diameter cylinder. The cell leak is about 6 Torr per hour, corresponding to the estimated oxygen impurity of 70 ppm (in $N_2$ and $N_2$-$CO_2$ mixtures) and water impurity of less than 3.5 ppm (in all mixtures tested). The flow rates of the mixture components through the cell are monitored by an Omega FMA-A2308 mass flow controller for $N_2$ and dry air, Sierra Smart Trek-2 Series 100 flow controller for $CO_2$, and 2000 sccm and 20 sccm MKS mass flow controller calibrated for $N_2$, and for $H_2$-air mixtures.

### 3.3. Nanosecond Pulse Discharge Waveforms and Plasma Images

The discharge electrodes are connected to a custom-made high peak voltage, nanosecond duration pulse generator. The pulse generator produces alternating polarity pulses, with peak voltage up to 15 kV and pulse duration of approximately 100 ns FWHM. The pulse generator also produces a relatively low voltage, opposite polarity "pre-pulse" approximately 6 microseconds prior to the main high-voltage pulse. The high-voltage pulse amplitude is controlled by the DC input to the pulse generator, provided by a Glassman Series LQ DC power supply. The DC input voltage is varied from 490 V or 510 V. Figure 3.4 shows the discharge pulse voltage waveforms for both positive and negative polarity pulses

in 100 Torr of air at DC voltage of 490V. It can be seen that peak voltages for different polarities are very close to each other.

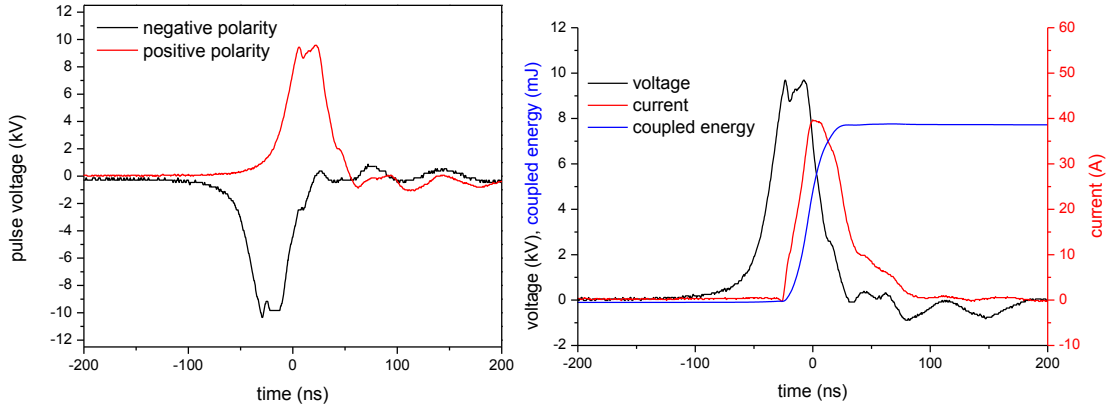


**Figure 3.4. Left: positive and negative polarity discharge pulse voltage waveforms in air at P = 100 Torr, at the DC input voltage of 490 V. Right: voltage, current and coupled energy waveforms for a negative polarity pulse at the same experimental conditions.**

Figure 3.5 shows voltage, current and coupled energy waveforms in $N_2$, air and their mixture with $CO_2$ at P = 100 Torr. It can be seen that breakdown voltage is approximately 10 kV and peak current is about 40-45 A for all mixtures. During the breakdown, the voltage drops by several hundred Volts, as the discharge current begins to rise. The energy coupled to the plasma is 7.5-8.0 mJ per pulse, and FWHM current pulse duration is approximately 50-60 ns.

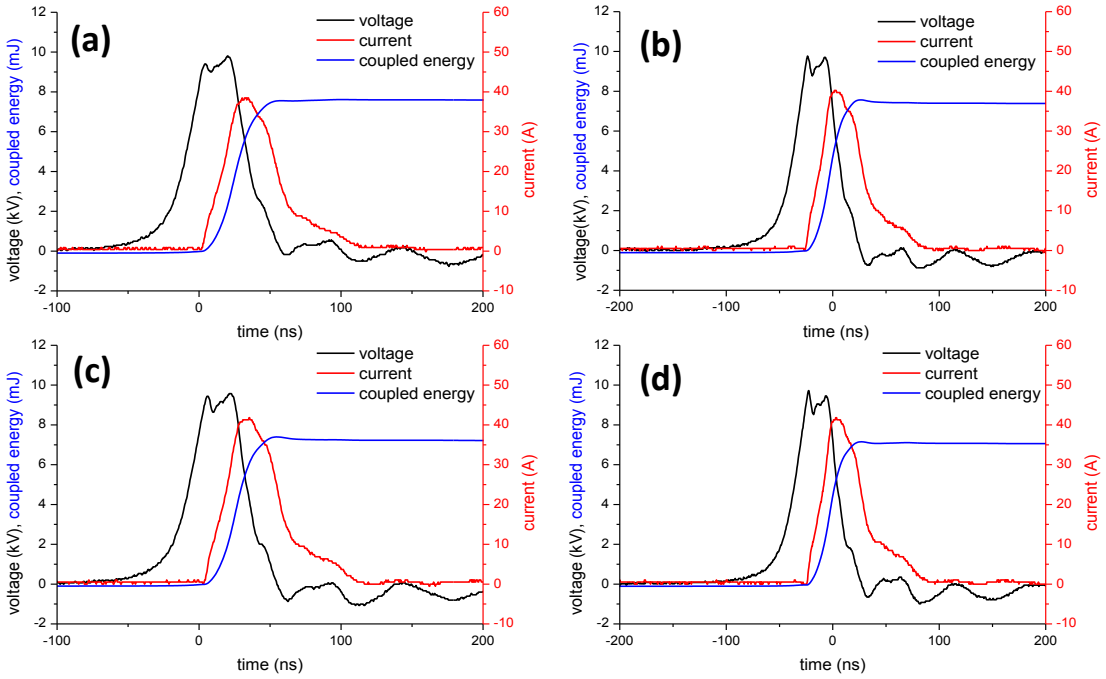


**Figure 3.5. Typical positive polarity ns pulse discharge voltage, current and coupled energy waveforms in (a) $N_2$, (b)10% $CO_2$-$N_2$, (c) air, and (d) 10% $CO_2$-air at P = 100 Torr. DC input voltage is 490 V, pulse repetition rate is 60 Hz.**

Figure 3.6 shows typical discharge voltage, current, and coupled energy waveforms in air and 3% $H_2$-air mixtures at higher DC input voltage of 510 V. At these conditions, the peak voltage, peak current and coupled pulse energy increase to about 12 kV, 50 A and 10.0 mJ/pulse, respectively.

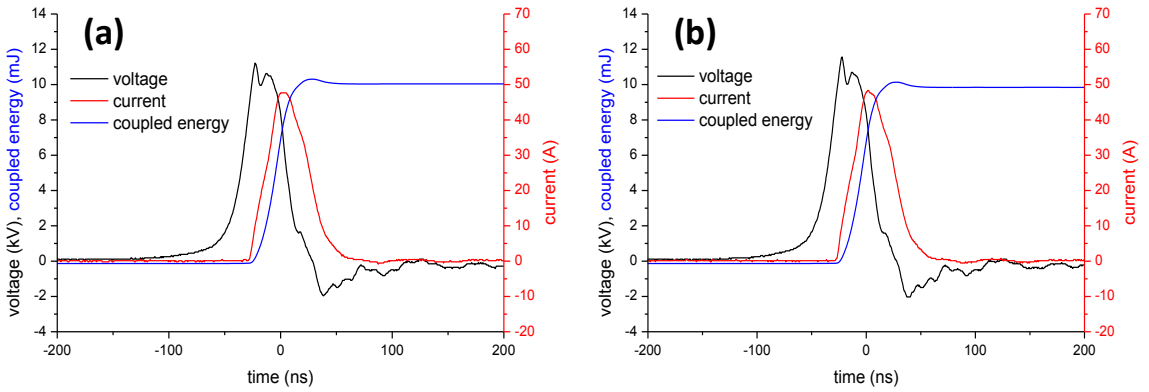


**Figure 3.6. Typical positive polarity ns pulse discharge voltage, current and coupled coupled energy waveforms in (a) air and (b) 3% $H_2$-air at P = 100 Torr. DC input voltage 510 V, repetition rate 60 Hz.**

Figures 3.7 – 3.10 show broadband plasma emission images in positive and negative polarity discharges in $N_2$, air, and their mixtures with 10% of $CO_2$ at P =100 Torr, at the conditions of Figure 3.5. In all images, the grounded electrode is on the left. In nitrogen and air, both single-shot and 100-shot average images appear similar. The plasma emission intensity along the filament centerline is somewhat lower, especially in air and in the 10% $CO_2$-air mixture, due to 1 mm laser diameter beam access ports in the electrodes. In 10% $CO_2$–$N_2$ and 10% $CO_2$–air mixtures, single shot images for both pulse polarities suggest that the bright region in the plasma filament moves relative to the holes in the electrodes shot-to-shot. The 100-shot average image in the 10% $CO_2$-air mixture suggests that the plasma filament is more diffuse compared to the image taken in air. The diameter of the diffuse plasma filament in $N_2$ and the 10% $CO_2$–$N_2$ mixture is approximately 3.0 mm, while in the 10% $CO_2$ –air mixture, the filament diameter increases to approximately 3.6 mm.

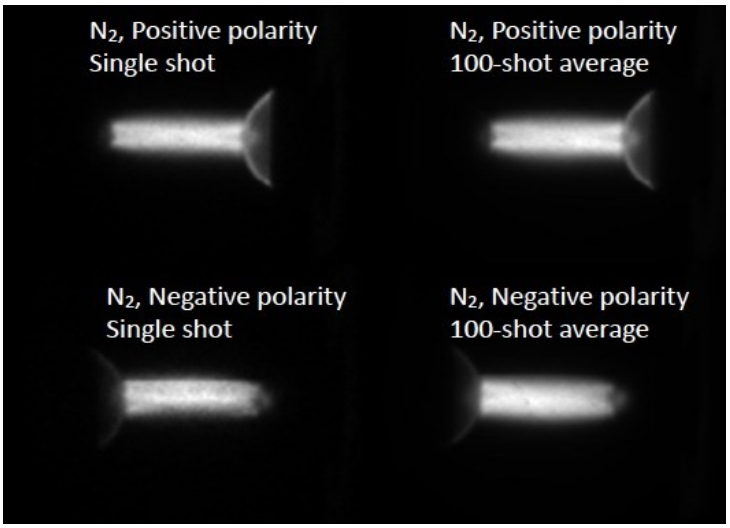


**Figure 3.7. Plasma emission images in $N_2$ at P = 100 Torr. Input DC voltage 490 V, coupled energy ~7.5 mJ/pulse. Camera gate is 100 ns.**

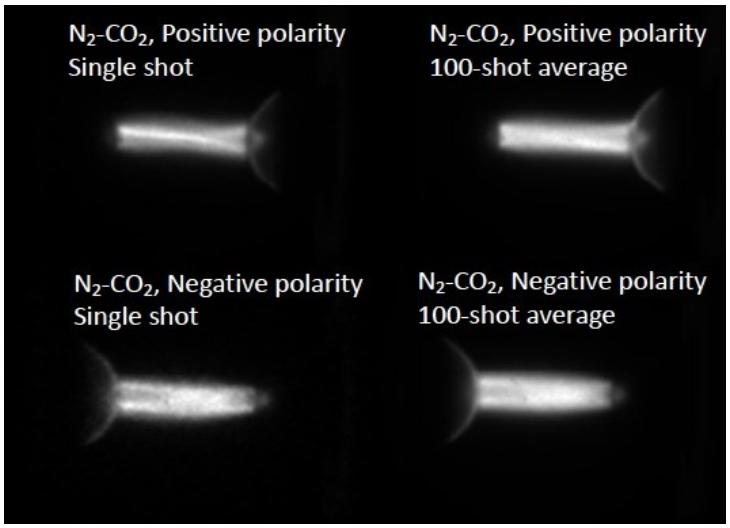


**Figure 3.8. Plasma images in the 10% $CO_2$-$N_2$ mixture at P = 100 Torr. Input DC voltage 490 V, coupled energy ~7.5 mJ/pulse. Camera gate is 100 ns.**

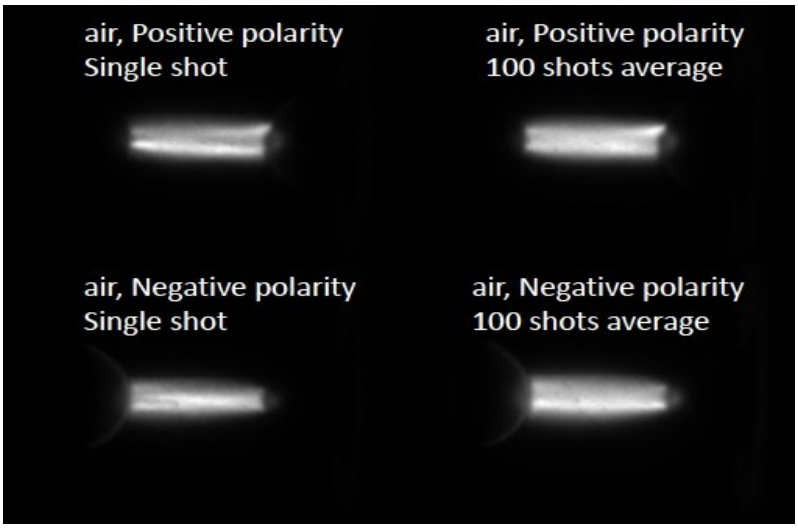


**Figure 3.9. Plasma images in air at P = 100 Torr. Input DC voltage 490 V, coupled energy ~7.5 mJ/pulse. Camera gate is 100 ns.**

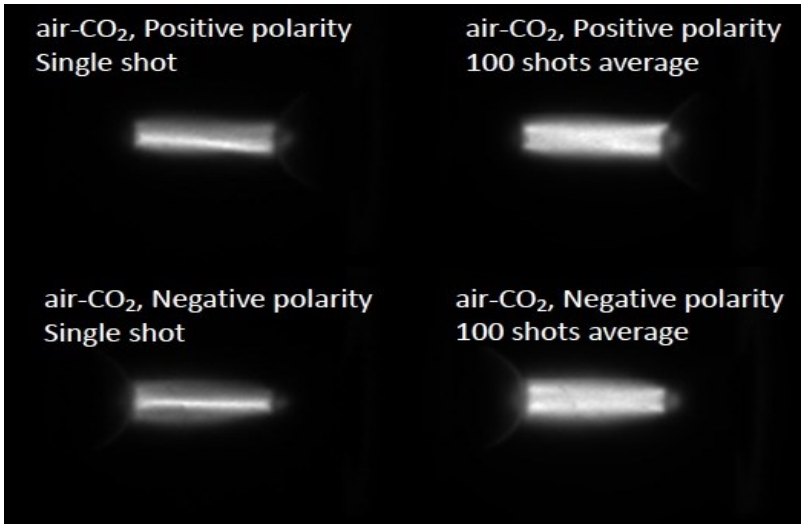


**Figure 3.10. Plasma images in the 10% $CO_2$-air mixture at P = 100 Torr. Input DC voltage 490 V, coupled energy ~7.5 mJ/pulse. Camera gate is 100 ns.**

In the experiments in $H_2$-air mixtures, the discharge pulse repetition rate is set to 10 Hz, to prevent accidental ignition of the mixture. Figure 3.11 shows single-shot and 100-shot average plasma images in different $H_2$-air mixtures. At DC input voltage of 490 V, plasma emission images are similar to those in 10% $CO_2$-$N_2$ and $CO_2$-air mixtures shown in Figures 3.7 – 3.10. Increasing the pulse energy from 7.5 mJ/pulse to 10.0 mJ/pulse results in the onset of a brighter, partially constricted filament. Figure 3.12 shows single-shot and 100-shot average plasma images in different $H_2$-air mixtures for positive pulse polarity. From single-shot images it can be seen that the discharge filament becomes partially constricted, producing a brighter region in the plasma. This effect appears to average out in 100-shot average images, which still indicate lower emission near the filament centerline.

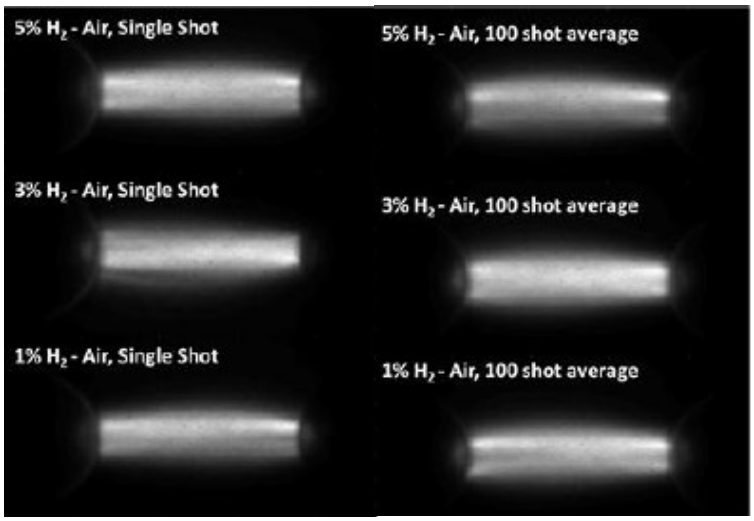


**Figure 3.11. Single-shot and 100-shot average plasma emission images in different $H_2$-air mixtures at P = 100 Torr. Input DC voltage 490 V; coupled energy ~7.5 mJ/pulse.**

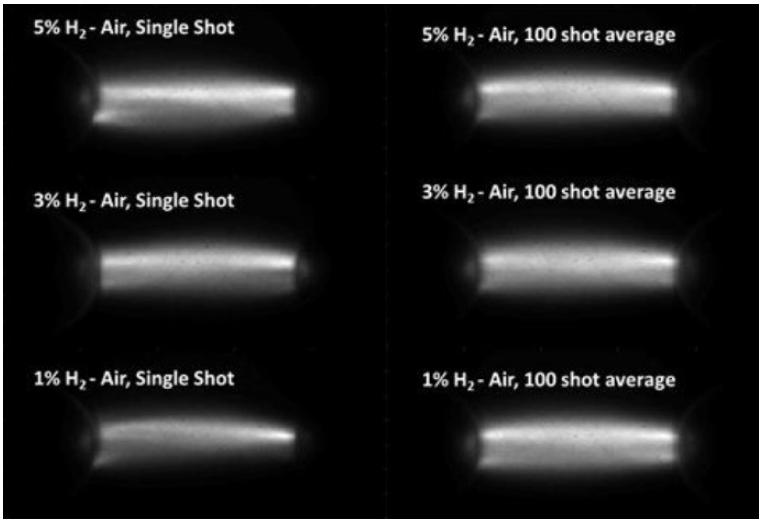


**Figure 3.12 Single-shot and 100-shot average plasma emission images in different $H_2$-air mixtures at P = 100 Torr. Input DC voltage 510 V; coupled energy 10.0 mJ/pulse.**

## 3.4. CARS Optical Setup

### 3.4.1 Ns Nd:YAG laser

In the present work, a Continuum Surelite SLIII-10 Nd:YAG laser is used as the broadband dye laser pumping source, as well as the CARS pump/probe beam source. The laser is operated at 10 Hz, with the output pulse FWHM of ~12 pm (0.4 $cm^{-1}$) without injection seeding, measured by High Finesse WS-U wavelength meter and pulse duration of ~10 ns, giving the CARS spectral resolution of 0.9-1.1 $cm^{-1}$. The Continuum injection seeder can be operated together with Nd:YAG laser, such that the output pulse FWHM can be reduced to 0.4 pm (0.015 $cm^{-1}$), improving CARS spectral resolution to 0.4-0.6 $cm^{-1}$. The

laser output energy varies depending on the Q-switch delay time, up to 425 mJ/pulse at 532 nm.

The laser can be operated using the internal trigger mode or it can be externally triggered by a delay generator. For external triggering, a +3.5V, 10 us duration square-shaped trigger pulse (into 50 Ω impedance) is needed to trigger the flash lamps. The same trigger pulse needs to be send to the laser control circuit at least 150 us after the first trigger pulse, to trigger the Q-switch. In the present experiments, the delay time for the Q-switch trigger varies between 320-360 us after the trigger for the flash lamps. At these conditions, the output laser pulse has the energy of 70-140 mJ per pulse at 532 nm, with the timing jitter of ± 0.5 ns.

### 3.4.2. Custom-made Broadband Dye Laser

The schematic diagram of the custom-built broadband dye laser, discussed in detail in reference [14], is shown in Figure 3.13. The 532 nm Nd:YAG laser output beam is split into two beams (with 90% to 10% ratio), and the 90% output energy beam is used to pump the broadband dye laser. After entering the laser, the 532 nm beam passes through another 80% to 20% beam splitter. The reflected 532 nm beam (with ~20% of the total pumping energy) is expanded by a -50 mm focal length cylindrical lens, and then focused by a 100 mm spherical lens at the oscillator cell as shown in Figure 3.13. A small portion of the dye fluorescence from the oscillator cell is reflected by a broadband high reflector, and passes through the oscillator cell again, generating the amplified spontaneous emission (ASE) from

the dye. ASE from the oscillator cell is directed to pre-amplifier and amplifier cells by prism and 607 nm mirror.

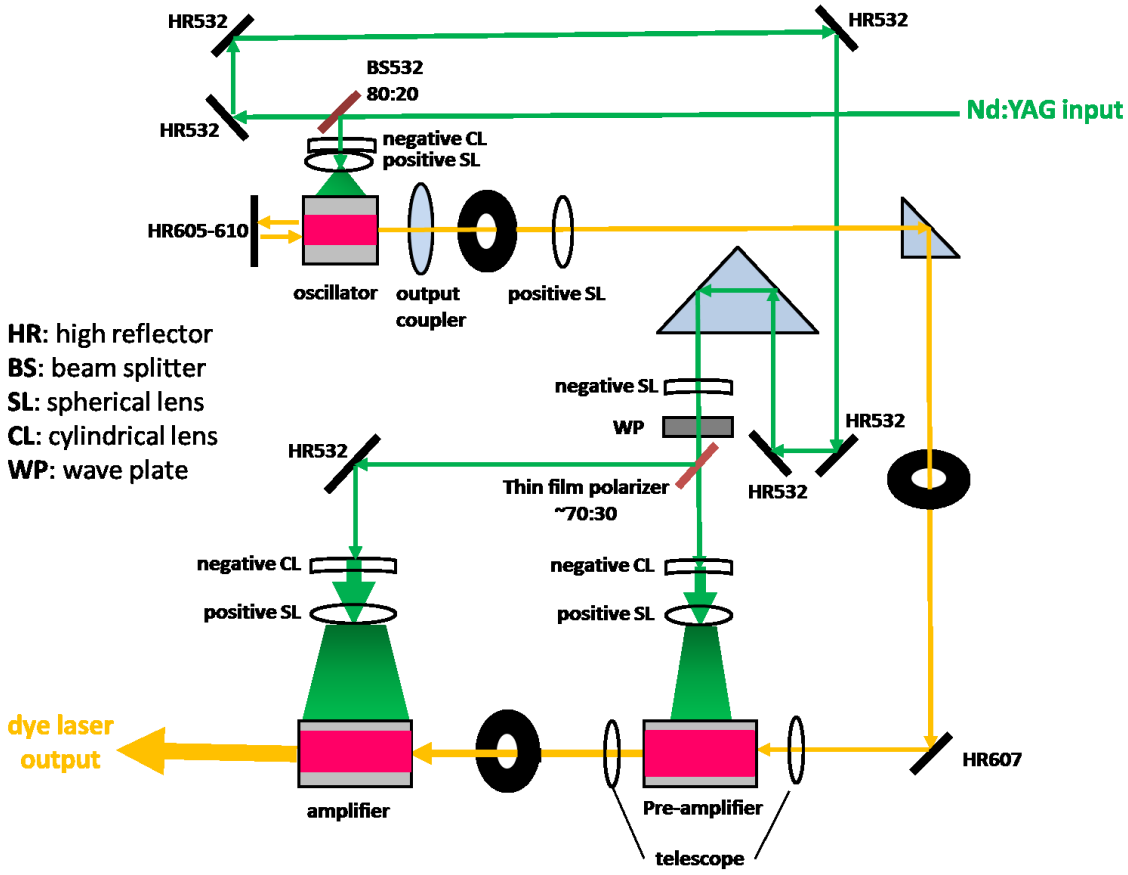


**Figure 3.13. Schematic of the broadband dye laser.**

The remaining 80% of the 532 nm beam is directed by a prism and several mirrors, and is split by a 70:30 thin film polarizer before the pre-amplifier cell, as shown in Figure 3.15. The lower energy pump beam (24% of the total) is aligned and focused at the pre-amplifier cell, while the higher energy pump beam (56% of the total) is focused at the amplifier cell. The ASE beam from the oscillator cell and the other two beams from the pre-amplifier and the amplifier cells overlap with each other to produce a Gaussian-profile output laser beam. Misalignment between the ASE beam and the beams from the pre-amplifier and amplifier cells would result in a high aspect ratio "cat's eye" output beam profile, instead of a nearly circular beam. The broadband dye laser output beam, centered at ~605 nm and with the spectral FWHM of 3 nm, is used as the Stokes beam in the collinear CARS system.

In the present setup, the dye laser pulse duration is similar to that of the pump laser. The conversion efficiency of the dye laser is strongly dependent on the composition of the dye, the age of the dye, the concentration of the dye, the flow rate of the dye through the cells, and the laser pulse energy. In the present experiments, Kiton Red 620 (KR620) and Rhodamine 640 (R640) dye mixture is used. To prepare the dye mixture, 500 mg of KR620 dye and 500 mg of R640 dyes need to be dissolved in a separate 500 mL volume of methanol. These are highly concentrated dye solutions that cannot be used directly in the experiment. The KR620 dye solution has a broadband spectral output centered at ~590 nm. Adding the R640 dye solution to the KR620 dye solution will red-shift the spectrum, while diluting the solution with a mixture of two dyes by methanol will blue-shift the spectrum. By adding the R640 dye to the solution, the center of the broadband output is moved to the 600-610 nm region, necessary for the detection of v = 0 to v = 4 vibrational bands of

molecular nitrogen (see Table 2.1). After shifting the dye output to the desired spectral region, methanol is added to the solution of KR620 and R640 dyes, to dilute the solution until the dye laser output energy reaches maximum. In the present experiments, the output laser beam has FWHM of ≈3 nm, centered at 604-606 nm (see Figure 3.14). The output energy and the conversion efficiency of the dye laser system at different pump laser pulse energies are shown in Figure 3.15. During the present experiments, the pulse energy of the Nd:YAG laser pumping the dye laser system was controlled at about 54 mJ, producing the output dye laser pulse energy of 5.8 mJ at the conversion efficiency of 10.5%.

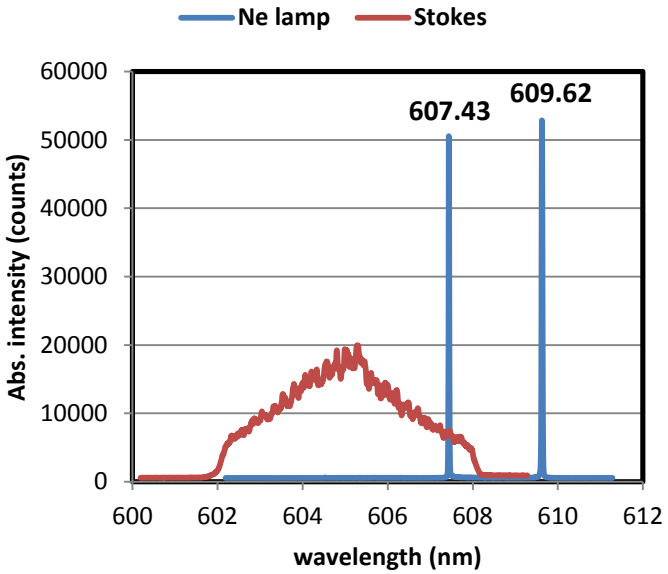


**Figure 3.14. Typical spectral output of the broadband dye laser using a R640 -KR620 mixture, plotted together with two Ne lamp lines.**

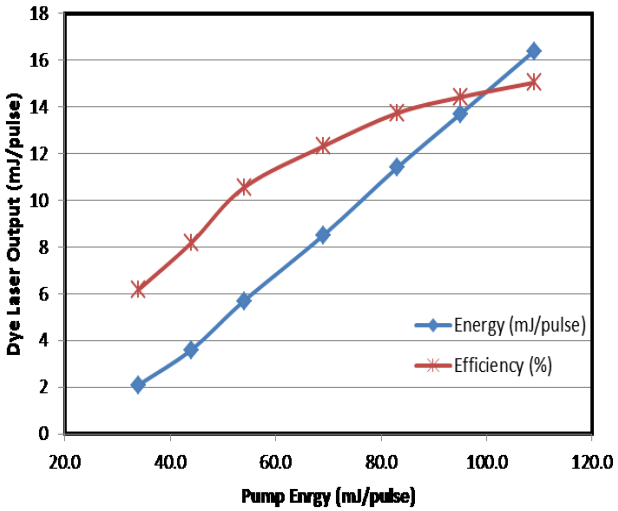


**Figure 3.15. Output pulse energy and conversion efficiency of the broadband dye laser system at different Nd:YAG laser pulse energies.**

### 3.4.3 CARS Experimental Setup

In the present experiments, the collinear CARS phase-matching geometry is used, since it generates much higher signal-to-noise and due to its relative simplicity. As discussed above, the output beam from the Nd:YAG laser is split into two beams with a 90:10 ratio, 90% of the Nd:YAG laser output energy is used to pump the broadband dye laser and the remaining 10% energy is used as the CARS pump/probe beam, respectively. The divergence of the pump/probe beam can be manipulated using different telescope lens pairs (in Figure 3.16 a lens pair with focal lengths of 66 mm and 125 mm is shown). By changing the divergence of the pump/probe beam, the length of the CARS probe region can be varied, depending on the experimental geometry. The output beam from the broadband dye laser, used as the CARS Stokes beam, is overlapped with the CARS pump/probe beam using the dichroic mirror R473, T532 & 607 placed before the discharge test cell (as shown

in Figure 3.16). After this, both beams are focused between two spherical electrodes 7 mm in diameter and 8 mm apart, through 1 mm diameter channels drilled along the center line of both electrodes, as shown in Figure 3.2, using a 2" diameter, 150 mm focal length spherical lens. After the discharge electrodes, another 2" diameter, 200 mm focal length is used to collimate the beams. The power of the pump/probe beam can be varied by using a 532 nm wave plate to make the power of the pump/probe beam approximately a factor of two higher than that of the Stokes beam. The 607 nm wave plate is used to rotate the polarization plane of the Stokes beam, such that the pump/probe beam and the Stokes beam have the same polarization, thereby maximizing the CARS signal. After the f = 200 mm lens, a dichroic mirror R473, T532 & 607 (see Figure 3.16) is used to dump most of the pump/probe beam and the Stokes beam, while reflecting the CARS signal beam. The remaining small fraction of the 532 nm beam and the CARS signal beam are directed to the spectrometer. A 100 mm focal length lens and a single band-pass filter are placed in front of the slit of the spectrometer, to focus the CARS signal beam at the slit and to block the remainder of the 532 nm beam. The spectrometer slit width is fixed at ~50 um.

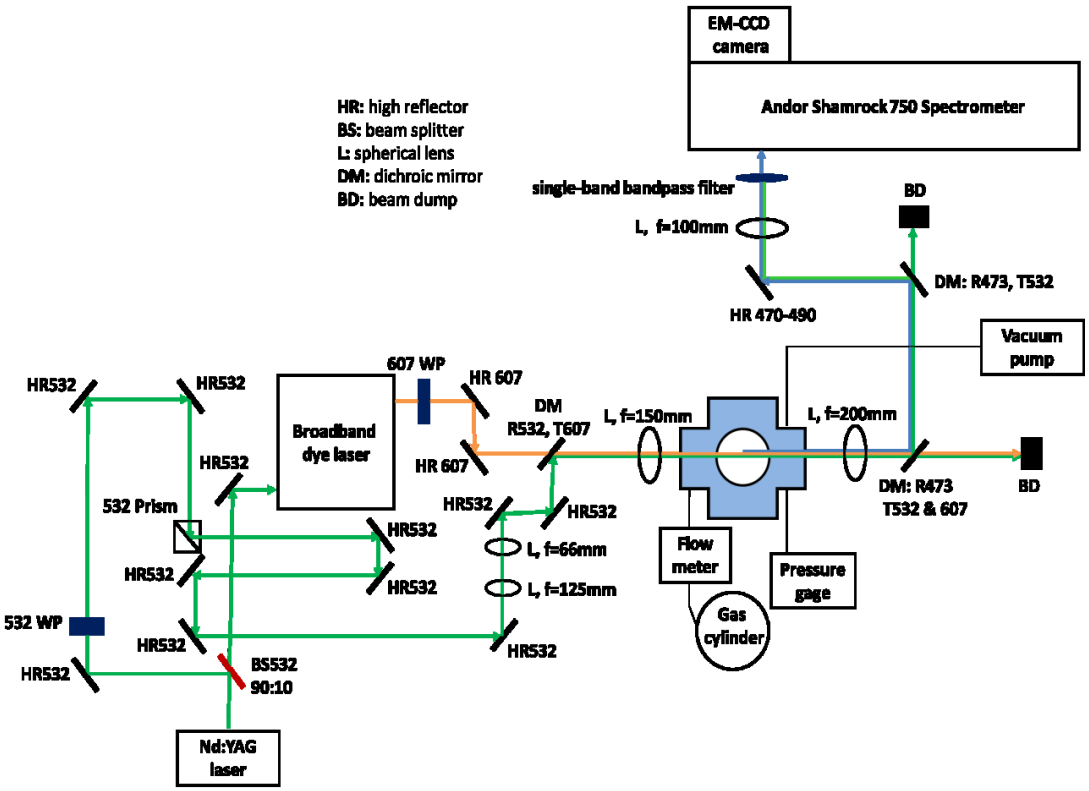


**Figure 3.16. Schematic diagram of the CARS system. The 532 nm and 607 nm beams are focused halfway between the discharge electrodes (see Figure 3.1). The dichroic mirror R473, T532 & 607 after the discharge cell transmits most of 532 nm and 607 nm beams toward the beam dump. A small fraction of the 532 nm beam is directed to the spectrometer, along with the CARS signal beam, and removed by a dichroic mirror R473, T532, and by a 513-528 nm band pass filter. The highest resolution grating (3600 l/mm) is used in the spectrometer to obtain high resolution CARS spectra.**

The spatial resolution of the present diagnostics in the direction of the laser beams is determined by traversing a microscope slide ~ 1 mm thick through the focal region of the beams between the discharge electrodes using a micrometer translation stage, and measuring the intensity of the non-resonant signal (NRS) produced from the microscope slide. In CARS measurements in a ns pulse discharge, a telescope lens pair with focal distances of 66 mm and 125 mm is used. The results of NRS distribution measurement are plotted in Figure 3.17, showing that 90% of the signal originates in the region approximately 3.5 mm long, which is considered to be the CARS probe length.

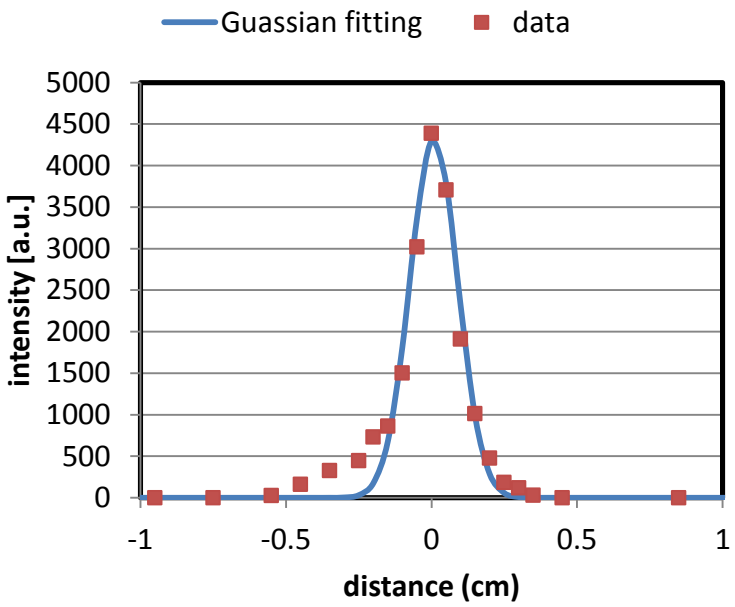


**Figure 3.17. CARS probe region used for measurements in a ns pulse discharge filament. The non-resonant background signal distribution shown in the figure is measured using the 66 mm and 125 mm lens pair. 90% of the CARS signal originates in a region 3.5 mm long.**

### 3.4.4 Data Collection System

The CARS signal collection system includes a spectrometer, an EM-CCD camera, and a computer controlling the spectrometer. Andor Shamrock 750 spectrometer, which has the focal length of 750 mm and three gratings installed in a grating turret, is used with an Andor Newton EM-CCD camera attached to the exit plane flange of the spectrometer. Three different gratings 600 l/mm, 1800 l/mm and 3600 l/mm, are mounted on the grating turret. The 3600 l/mm grating is chosen in this experiment in order to get the highest resolution spectra. The thermoelectric cooler in the EMCCD camera stabilizes the sensor temperature at -80$^{o}$C, using 20$^{o}$C external cooling water, to minimize the dark current signal from the camera. The EM-CCD camera also provides electron multiplying (EM) gain to amplify low-intensity signals. The integration time during the spectra collection and the EM gain factor are controlled by the Andor spectrometer software.

Figure 3.18(a) shows the mercury pen lamp spectral line profile measured by the spectrometer using the highest resolution grating. The Gaussian fitting for the line shape indicates FWHM is of approximately 1.0 cm$^{-1}$. This lineshape is used as the instrument function by the CARSFT code to generate synthetic spectra used for temperature inference. Figure 3.18(b) shows the mercury pen lamp line shape measured using the same grating, with an additional relay lens pair attached to the spectrometer exit port. It can be seen that the use of the relay lens pair result only in a slight improvement of the spectral resolution to 0.75 cm$^{-1}$. As a result, the relay lens pair has not been used in the present experiments.

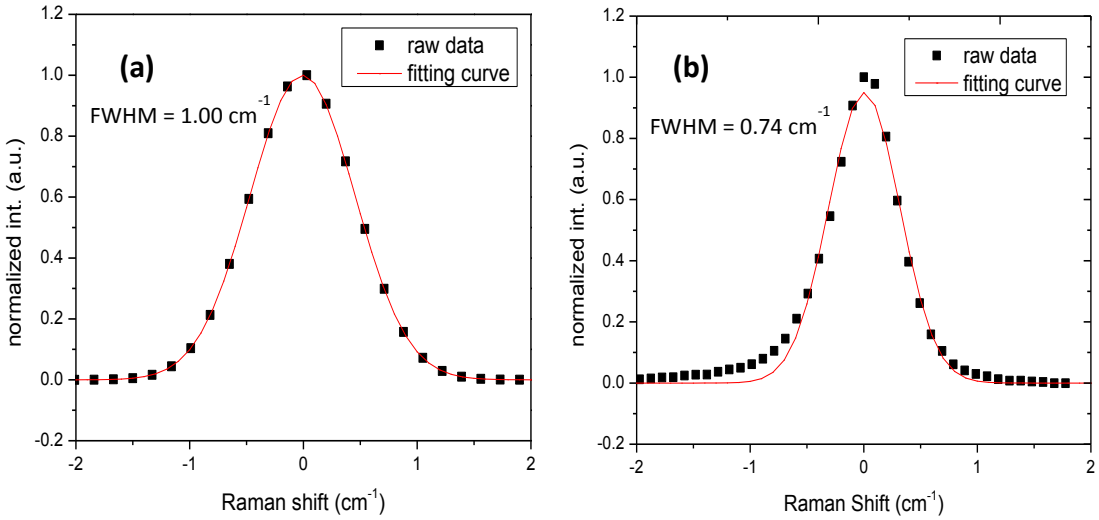


**Figure 3.18 Normalized Hg pen lamp line profile taken with a 3600 l/mm grating without (a) and with (b) the relay lens pair, illustrating the spectral resolution and the instrument function used by CARSFT synthetic spectrum code.**

### 3.5 Results and Discussion: Nitrogen, Air, and Mixtures with $CO_2$

#### 3.5.1 Vibrational Excitation and Vibrational Temperature

Figure 3.19 and Figure 3.20 show 600 laser shot accumulation CARS spectra for three different delay times after the discharge pulse in 100 torr $N_2$ and air, respectively. In Figure 3.20, it can been seen that vibrational levels up to $N_2$(v = 4) are detected at t = 4 μs. As discussed in Chapter 2, the area under the squareroot of the intensity of a CARS spectrum for a vibrational band with quantum number v is proportional to the difference between populations of vibrational levels v and v+1 (see Equations 2.14 and 2.15). In nitrogen, at t = 800 μs, the increase in normalized square-root peak intensities of vibrational bands for v =

1 and v = 2 is readily apparent, compared to t = 4 μs. At t = 4 ms, both v = 1 and v = 2 band intensities decrease, while the v = 3 peak disappears completely. In Figure 3.21, a similar trend is observed in air, showing that v = 1 and v = 2 vibrational band intensities increase from t = 10 us to 200 us. Similar to the data in nitrogen at t = 1 ms, the intensities of vibrational bands v = 1 and v = 2 decrease, and the v = 3 vibrational band completely disappears.

Figure 3.21 plots $N_2$(v=0-3) vibrational level populations inferred from the broadband CARS spectra in nitrogen, such that shown in Figure 3.19. It can be seen that $N_2$(v = 1, 2) relative populations steadily increase from t = 4 μs to ~ 1 ms before decaying on a ms time scale. This behavior was also observed in previous studies of ns discharges in nitrogen and air [3, 4].

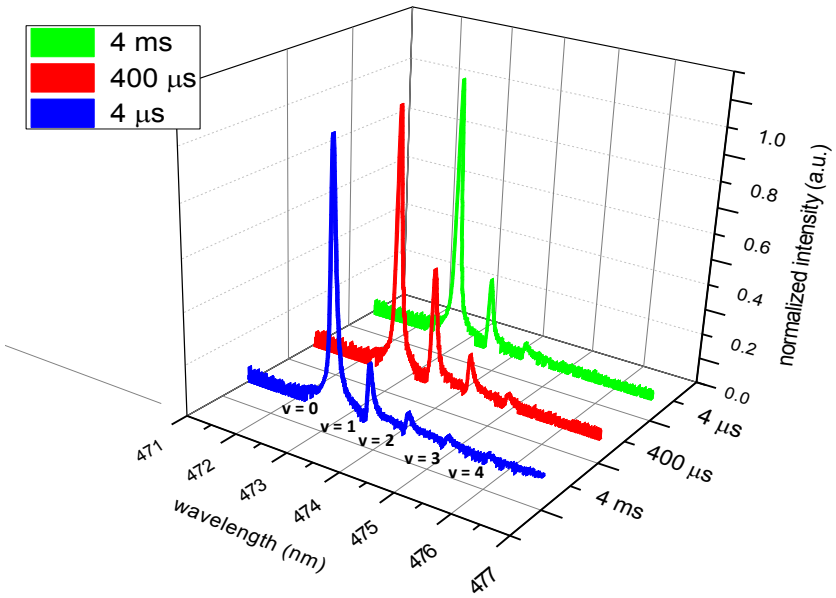


**Figure 3.19. Three normalized CARS spectra taken in 100 Torr of $N_2$ for three different delay times after the discharge pulse at the conditions of Figure 3.7, showing the time evolution of $N_2$ (v = 0-4) vibrational level populations.**

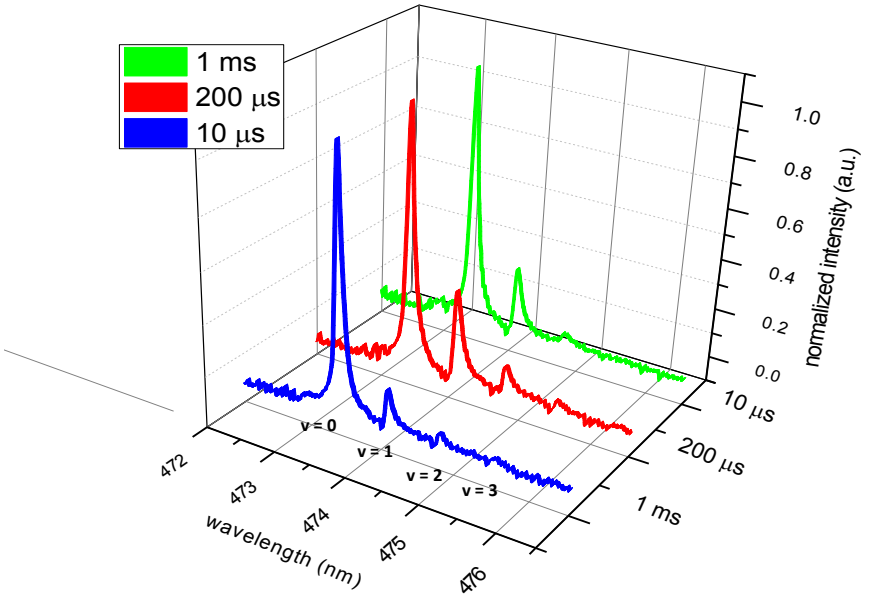


**Figure 3.20. Three normalized CARS spectra taken in 100 Torr of air for three different delay times after the discharge pulse at the conditions of Figure 3.9, showing the time evolution of $N_2$ (v = 0-3) vibrational level populations.**

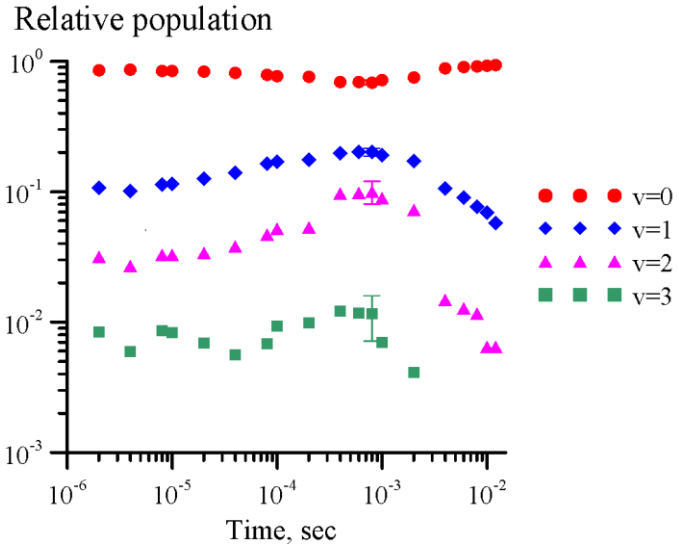


**Figure 3.21. Time evolution of relative populations of $N_2$ vibrational levels v = 0 -3 after the discharge pulse in $N_2$ at P = 100 Torr, for the discharge pulse coupled energy of 7.5 mJ/pulse. Discharge pulse repetition rate is 60 Hz.**

Since the conditions in the discharge afterglow appear to indicate significant vibrational nonequilibrium (see Figures 3.19-3.21), the $N_2$ first level vibrational temperature is used as a parameter quantifying non-equilibrium vibrational populations. The first-level vibrational temperature is defined as the slope of the vibrational distribution function (VDF) at v = 0,

$$T_{V01} = \frac{\theta_v}{\ln(f_0/f_1)} \qquad \text{(Equation 3.2)}$$

where $\theta_V$ = 3353 K is the energy difference between the ground state and the first excited vibrational state, and $\mathbf{f_0}$ and $\mathbf{f_1}$ are relative population of the ground state and the first excited state, respectively. The time evolution of $N_2$ vibrational temperature and the kinetic processes involved in nitrogen, air, and their mixtures with $CO_2$ are discussed in Section 3.5.3.

### 3.5.2 Rotational-translational temperature inference from CARSFT synthetic spectra

The rotational-translational temperature in the plasma is obtained from synthetic spectra generated by the Sandia CARSFT code [46]. Basically, the rotational-translational temperature is inferred from the partially resolved rotational structure of the v = 0 band of $N_2$ CARS spectra.

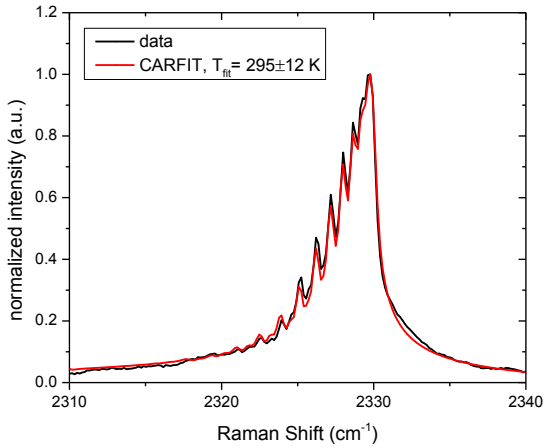


**Figure 3.22. Comparison of the experimental CARS spectrum, $N_2$ (v=0) vibrational band taken in room air, and best-fit CARSFT synthetic spectrum. Rotational-translational temperature inferred is T = 295 ± 12 K.**

Figure 3.22 shows comparison between a CARS spectrum taken in ambient air, with the Nd:YAG laser operating with injection seeding turned on, and CARSFT synthetic spectrum. To determine the uncertainty of temperature inference using CARSFT, 10 room air CARS spectra were taken, and rotational-translational temperature was inferred from each one of them. The mean value of the inferred temperature is 292 K, with the standard deviation of ±12K. The result is very close to ambient temperature in the lab, approximately 20°C (293 K). Figure 3.23 (a) shows two $N_2$(v = 0) band CARS spectra taken in a ns pulse discharge in a 10% $CO_2$ -$N_2$ mixture at P = 100 Torr, at different delay times, without injection seeding. Although in this case the spectral resolution of CARS spectra is noticeably lower, the rotational-translational temperature can be still inferred from the partially resolved rotational structure of the $N_2$(v = 0) vibrational band. It can be seen that at longer delay time after the discharge pulse (180 μs), the rotational structure of the $N_2$(v = 0) band is more pronounced, and individual rotational peaks can be identified, indicating higher

rotational-translational temperature. Figure 3.23 (b) shows comparison of the experimental spectrum with the best-fit synthetic spectrum generated by CARSFT.

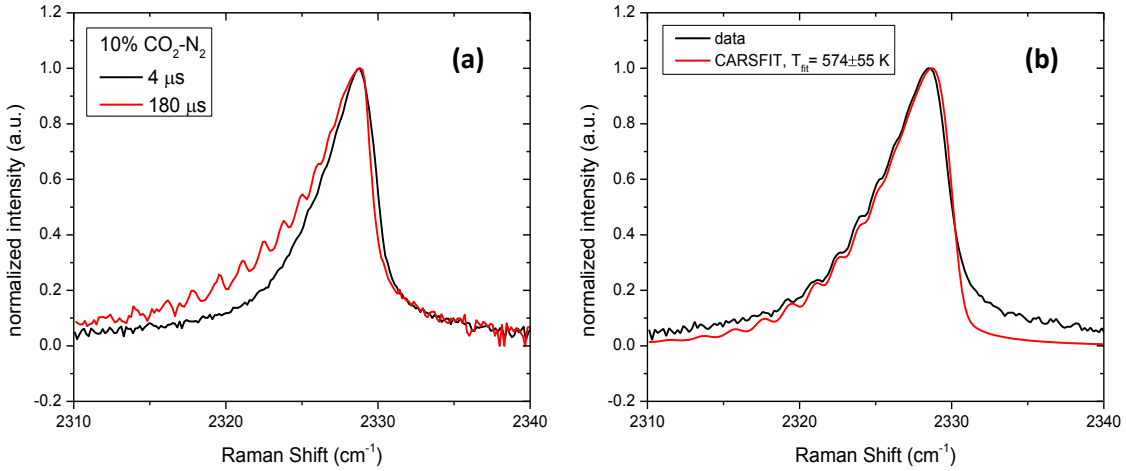


**Figure 3.23. (a) Sample CARS spectra of the $N_2$ (v=0) band taken in a ns pulse discharge in 10% $CO_2$-$N_2$ mixture at P = 100 Torr, at different delay times after the discharge pulse. (b) Comparison of the experimental spectrum in a ns pulse discharge in $N_2$ at P=100 Torr, at t= 800 µs, with best-fit CARSFT synthetic spectrum used for the rotational-translational temperature inference.**

Figure 3.24(a) shows two $N_2$(v = 0) band CARS spectra taken in a ns pulse discharge in a 10% $CO_2$-air mixture at P = 100 Torr, at different delay times after the discharge pulse, without injection seeding. Similar to the results in 10%$CO_2$-$N_2$ mixtrue, shown in Figure 3.23, it can be seen that at a longer delay time (180 µs) after the discharge pulse, the rotational structure of the $N_2$ (v = 0) band is more pronounced, individual rotational peaks can be identified, indicating higher rotational-translational temperature. Figure 3.24(b) shows comparison of the experimental spectrum in a ns pulse discharge with the best-fit

synthetic spectrum generated by CARSFT (best fit rotational temperature of T = 651 ± 60 K). Note that the spectral resolution of the CARS spectra taken in the 10% $CO_2$-air mixture is somewhat lower, compared to the spectra taken in the 10% $CO_2$-$N_2$ mixture (see Figure 3.23).

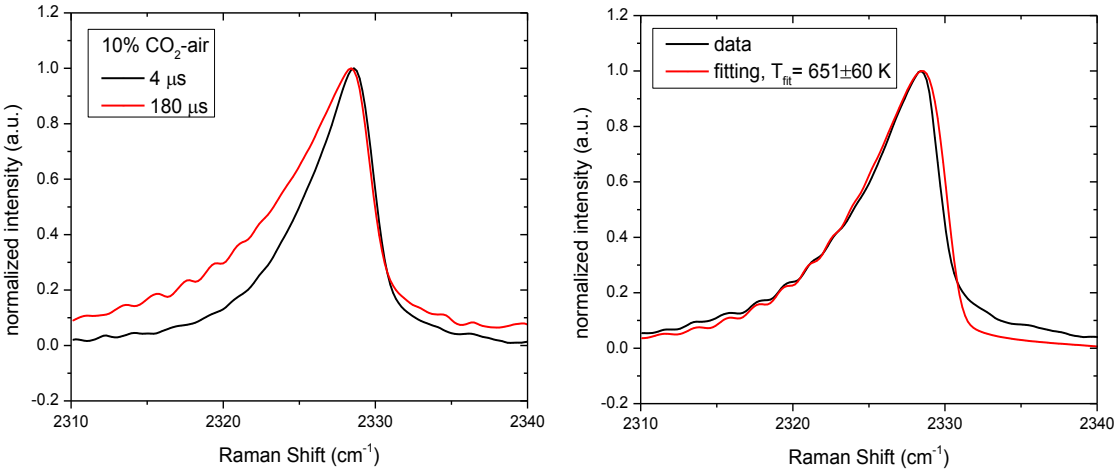


**Figure 3.24. (a) Sample CARS spectra of $N_2$(v=0) band taken in a ns pulse discharge in 10% $CO_2$-air mixture at P = 100 Torr, at different delay times after the discharge pulse. (b) Comparison of the experimental spectrum in a ns pulse discharge in air at P = 100 Torr, for t = 600 μs, and the best-fit CARSFT synthetic spectrum used for rotational-translational temperature inference.**

### 3.5.3 Time Evolution of Vibrational Temperature and Rotational-translational Temperature in $N_2$, Air and Their Mixtures with $CO_2$

Figure 3.25 shows the time-resolved first-level $N_2$ vibrational temperature, defined by Equation 3.1, in the afterglow of a ns discharge in $N_2$ at P = 100 Torr. Master equation kinetic modeling calculations [5] demonstrated that after the initial $N_2$ vibrational excitation by electron impact during the discharge pulse,

$$N_2 + e \rightarrow N_2 (v>0) + e \qquad \text{(Equation 3.3)}$$

which creates markedly "bi-modal" initial vibrational distribution, $N_2$ vibrational level populations at w ≥ 2 are redistributed by the downward vibration-vibration (V-V) exchange,

$$N_2(w) + N_2(v = 0) \rightarrow N_2(w - 1) + N_2(v = 1) \qquad \text{(Equation 3.4)}$$

with the room temperature rate coefficient for w = 1 of $k_{VV} = 1.5 \times 10^{-14}$ $cm^3 s^{-1}$ [47, 48], which reduces the populations of vibrational levels with w ≥ 2 and increases the population of the vibrational level v = 1. This downward V-V exchange after the discharge pulse, which increases the first level vibrational temperature, is readily apparent in Figure 3.25. It can be seen that the initial vibrational temperature in nitrogen is $T_V \approx 1600$ K at t = 1-2 us, due to vibrational excitation by electron impact during the discharge pulse (see Equation 3.3). Then, the downward V-V exchange dominates in the discharge afterglow, increasing the relative population of vibrational level v = 1 while decreasing relative populations of vibrational levels w > 2. The $N_2$ vibrational temperature increases from 1600 K at t = 2 μs to 2700 K at t = 800 μs, before decreasing at t > 1 ms (see Figure 3.25). Based on the $N_2$ vibrational populations plotted in Figure 3.21, the characteristic time for the $N_2$-$N_2$ V-V

exchange for w = 2 is $\tau_{VV} = \frac{1}{2k_{VV} \cdot n(N_2) \cdot f_1/f_2} \approx 40$ μs, where $n(N_2)$ is the number density of nitrogen molecules, and $f_2$ and $f_1$ are the relative populations of w=2 and w=1, respectively. This estimate is qualitatively consistent with the time scale for vibrational population rise detected in the experiment (see Figure 3.25). After t = 1 ms, the vibrational temperature starts to decrease due to the radial diffusion of vibrationally excited molecules out of the plasma filament, with the characteristic time of $\tau_{diff} \sim \frac{(d/2)^2}{D} \sim 1 - 3$ ms, where d is the diameter of plasma, and D is the diffusion coefficient. The characteristic time for vibrational-translational (V-T) self-relaxation of nitrogen at the present conditions is estimated to be on the order of $\tau_{VT}(N_2 - N_2) \sim 10$ ms [5, 50], much longer compared to the radial diffusion time scale.

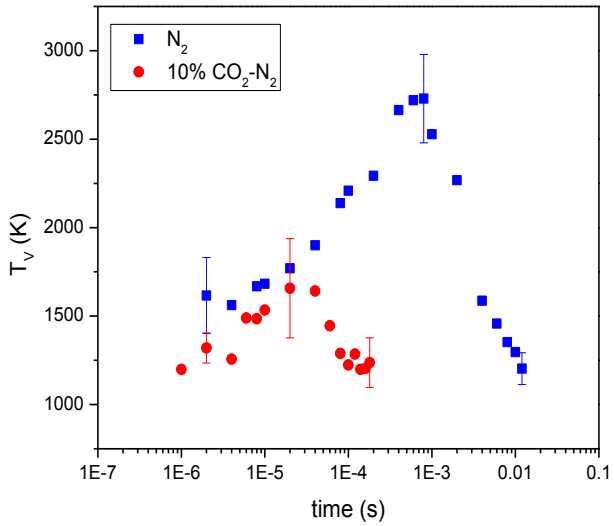


**Figure 3.25. Time-resolved first-level $N_2$ vibrational temperature after the discharge pulse inferred from the CARS spectra in nitrogen and 10% $N_2$-$CO_2$ mixture at P = 100 Torr.**

From Fig. 3.25, it is apparent that adding 10% $CO_2$ to $N_2$ results in a much more rapid $N_2$ vibrational relaxation, on the time scale of $\tau_{vib}$ ($N_2$) ~ 50-100 μs. In $N_2$-$CO_2$ mixtures, lower initial vibrational temperature, $T_V$ ~ 1200 K, is detected at t = 1-2 μs after the beginning of the discharge pulse, since some of the discharge coupled energy is stored in $CO_2$ vibrational and electronic energy modes. At t = 20 – 60 μs after the beginning of the discharge pulse, the vibrational temperature increases due to the downward V-V' energy transfer between $N_2$ molecules, trend similar to the one as observed in nitrogen. At t = 50-100 μs, rapid V-V' energy transfer between vibrational by excited nitrogen molecules and $CO_2$ asymmetric stretch vibrational mode dominates in the discharge afterglow, causing rapid $N_2$ vibrational relaxation (see Figure 3.25).

At these conditions, the characteristic time for the rapid near-resonance V-V' energy transfer from $N_2$ to $CO_2$ asymmetric stretch mode (ν3),

$$N_2(v = 1) + CO_2(000) \rightarrow N_2(v = 0) + CO_2(001), \qquad \text{(Equation 3.5)}$$

with the room temperature rate coefficient of $k_{VV'} = 5x10^{-13}$ $cm^3s^{-1}$ [27], is an order of magnitude shorter, $\tau_{VV'} \sim 1/ [k_{VV'} \cdot n(CO_2)] \sim 5$ μs. This suggests that the net rate of vibrational energy relaxation is controlled by intra-molecular $CO_2$ energy re-distribution from the asymmetric stretch to symmetric stretch (ν1) and bending (ν2) modes,

$$CO_2(001) + M \leftrightarrow CO_2(100, 020, 010) + M, \qquad \text{(Equation 3.6)}$$

followed by the rapid V-T relaxation of to the bending mode,

$$CO_2(100) + M \rightarrow CO_2(010) + M + \text{heat}, \qquad \text{(Equation 3.7)}$$

where M = $CO_2$ or $N_2$. Based on $CO_2$ (ν2) V-T relaxation rates from the literature [27], the estimated $CO_2$ vibrational energy relaxation time is $\tau_{VT}$ ($CO_2$-M) ~ 200 μs, consistent with the present observations.

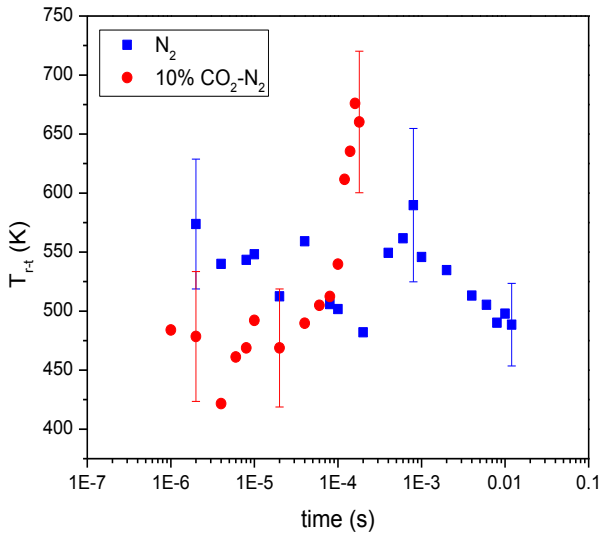


**Figure 3.26. Time-resolved rotational-translational temperature after the discharge pulse inferred from the CARS spectra in nitrogen and 10% $CO_2$–$N_2$ mixture at P = 100 Torr. The uncertainty bars correspond to 20 % increase in CARSFT residual relative to the minimum value that corresponds to the "best-fit" temperature.**

Figure 3.26 plots the rotational-translational temperature after the discharge pulse in nitrogen and in the 10% $CO_2$-$N_2$ mixture, inferred from the rotational structure of $N_2$(v = 0) band CARS spectra using best fit CARSFT synthetic spectra. It can be seen that in nitrogen at t = 2 μs to 1 ms, the temperature remains relatively flat, at T ~ 550 K, and decays after t = 10 ms due to the radial diffusion out of the discharge filament. In the 10% $CO_2$-$N_2$ mixture, the temperature starts from a somewhat lower value at T ~ 450 K, and exhibits a well-

pronounced steady rise at t = 4 – 400 μs, which appears to accelerate at t > 80 μs, and peaks at T = 670 K. The rapid temperature rise in the $CO_2$-$N_2$ mixture, on the time scale of ~ 100 μs, is consistent with the time scale of the $CO_2$ bending mode V-T relaxation (see Equation 3.7), which is likely to control the net rate of $N_2$ vibrational relaxation rate in the presence of $CO_2$. Relatively high temperatures at short delay times after the discharge pulse, T ≈ 570 K in nitrogen and T ≈ 470 K in $CO_2$-$N_2$ mixture at t = 2 μs (see Figure 3.26) may be due to the residual heating of the relatively slow flow in the cell by the previous discharge pulses, as well as due to the "rapid heating" processes occurring on a sub-microsecond time scale, which are not resolved in $N_2$ and $CO_2$-$N_2$ but detected in air and $CO_2$-air mixtures, as discussed below.

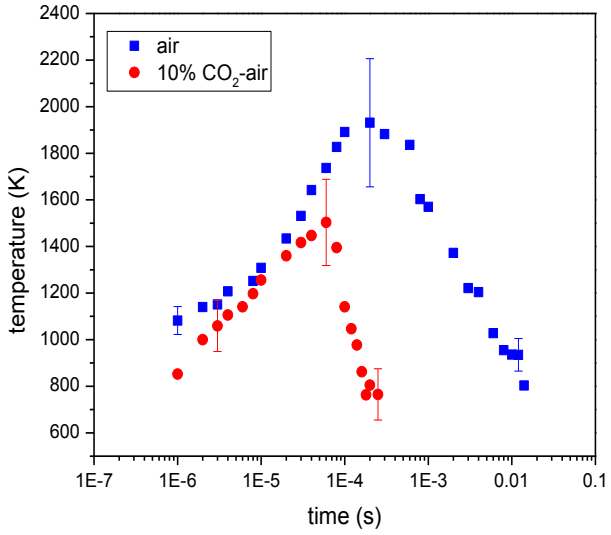


**Figure 3.27. Time-resolved first level vibrational temperature after the discharge pulse inferred from the CARS spectra in air and 10% $CO_2$–air mixture at P = 100 Torr.**

Figure 3.27 shows the $N_2$ first-level vibrational temperature in air and a 10% $CO_2$-air mixture. It can be seen that at $t \leq 3$ μs, $N_2$ first level vibrational temperature is lower in air and the air-$CO_2$ mixture, compared to $N_2$ and the $N_2$-$CO_2$ mixture. Some of the trends observed in air, such as vibrational temperature increase from the end of the discharge pulse, $T_V \sim 1100$ K at t = 200 ns, to $T_V \sim 1900$ K at t = 200 μs, are similar to the results in $N_2$ (see Figure 3.25). As shown by the kinetic modeling calculations [5], this behavior is also controlled by the downward $N_2$-$N_2$ V-V exchange process of Equation 3.3. However, both the initial and the peak values of the vibrational temperature are significantly lower compared to the results obtained in nitrogen. Since pulse peak voltage, current, and coupled energy waveforms in nitrogen and air are very close, this indicates that in air, lower discharge energy fraction goes to $N_2$ vibrational excitation by electron impact, compared to that in nitrogen. Also, vibrational temperature decay after the discharge pulse in air begins sooner, at t = 200 μs compared to t = 800 μs in nitrogen (compare with Figure 3.25). As shown in kinetic modeling calculations [5], vibrational relaxation in a ns pulse discharge in air is controlled by the $N_2$ vibrational relaxation by O atoms,

$$N_2(v = 1) + O \rightarrow N_2(v = 0) + O + \text{heat} \qquad \text{(Equation 3.8)}$$

produced primarily during collisional quenching of electronically excited $N_2$ molecules (generated by electron impact during the discharge pulse) by molecular oxygen,

$$N_2{}^*\left(A^3\Sigma_u^+, B^3\Pi_g, C^3\Pi_u, a^1\Sigma_u^-\right) + O_2 \rightarrow N_2\left(X^1\Sigma_g^+\right) + O + O \qquad \text{(Equation 3.9)}$$

Although in the present work O atom number density has not been measured, the kinetic model used in Ref. [5] is in good agreement with both O atom number density and $N_2$ vibrational level populations measured in our previous work [4], providing confidence in

the modeling predictions. Adding 10% $CO_2$ to air causes rapid $N_2$ vibrational relaxation, resulting in the reduction of vibrational temperature on the time scale of t = 50-200 μs (see Figure 3.27). The trend of vibrational temperature reduction on this time scale is similar to the results obtained in the 10% $CO_2$-$N_2$ mixture plotted in Figure 3.25. The similarity between these data sets suggests that in both cases, rapid vibrational relaxation of nitrogen is also caused by the near-resonance V-V' energy transfer from $N_2$ to $CO_2$ asymmetric stretch mode (see Equation 3.5), followed by the intramolecular vibrational energy redistribution in $CO_2$ and the V-T relaxation of the $CO_2$ bending mode (see Equations 3.6 and 3.7).

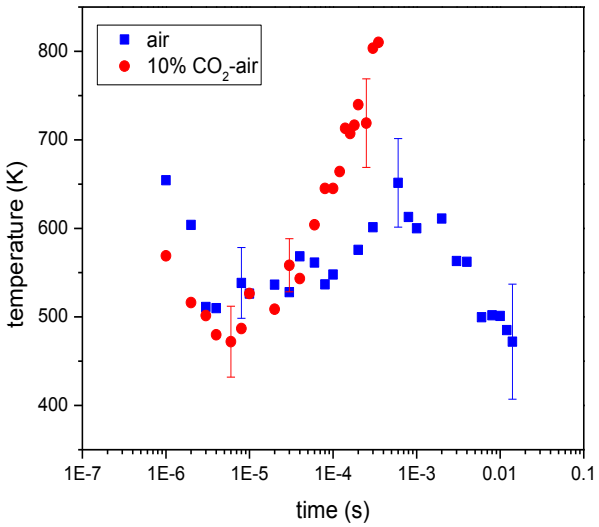


**Figure 3.28. Time-resolved rotational-translational temperature after the discharge pulse inferred from CARS spectra in $N_2$ and 10% $CO_2$–air mixture at P= 100 Torr. The uncertainty bars are evaluated in the same way as in Figure 3.27.**

Figure 3.28, which plots rotational-translational temperature after the discharge pulse in air and in the 10% $CO_2$-air mixture, indicates that kinetics of energy thermalization over a wide range of time scales after the discharge pulse, t ~ 100 ns – 10 ms, is somewhat more complex compared to the results obtained in nitrogen and in the 10% $CO_2$-$N_2$ mixture (see Figure 3.25). The results clearly indicate a well-defined "rapid" temperature rise on the time scale of t ~ 0.1 – 1 μs (shorter compared to the acoustic time scale of $\tau_{acoust} \sim d/2a \sim 2$-3 μs, where a ~ 0.5 mm/μs is the speed of sound at T = 500 K). This effect is observed both in air (heating from T ~ 510 K to T ~ 660 K) and in $CO_2$-air (heating from T ~ 490 K to T ~ 570 K). The results are consistent with our previous temperature measurements in a ns pulse discharge in air at 100 Torr [4] and kinetic modeling calculations [5], indicating that the rapid heating in air is dominated by quenching of $N_2$* molecules by oxygen molecules (see Equation 3.9) on the same time scale of t ~ 0.1 – 1 μs. In the present measurements in nitrogen and 10% $CO_2$-$N_2$ mixture, this effect has not been detected, both because "rapid heating" in nitrogen is considerably slower [5], and since $N_2$ (v=0) vibrational band in CARS spectra at t < 2 μs was saturated.

At t ~ 1 – 6 μs, the results indicate a well-pronounced temperature drop, to T ≈ 500 K in air and to T ≈ 470 K in $CO_2$-air, which has not been observed in our previous measurements in ns pulse filament discharges but has been detected in Ref. [18]. This rapid temperature reduction is most likely due to the near-adiabatic gas dynamic expansion of the filament heated on the sub-acoustic time scale, which has been predicted previously by the kinetic modeling, although with a lower magnitude compared to rapid heating, $\Delta T_{cool} \approx 50$ K vs. $\Delta T_{heat} \approx 200$ K [5].

A gradual temperature rise observed in air on the time scale of t = 6 – 600 μs, is qualitatively consistent with our previous measurements and kinetic modeling calculations [5]. It is due to the energy release during the V-T relaxation of nitrogen by O atoms (see Equation 3.8), generated during $N_2$* quenching by oxygen molecules (see Equation 3.8). Finally, temperature reduction at t > 1 ms is due to radial diffusion, similar to nitrogen (see Figure 3.27). In a 10% $CO_2$-air mixture, the data indicate a significant steady temperature rise at t = 20 – 200 μs, from T ~ 470 K to T ~ 760 K, at a much faster rate compared to air. Comparing it with the $N_2$ vibrational temperature reduction at these conditions (at t = 50-200 μs, see Figure 3.27), it is apparent that heating on this time scale is caused by the nitrogen vibrational energy transfer to $CO_2$, followed by $CO_2$ V-T relaxation, similar to the results in a 10% $CO_2$-$N_2$ mixture.

Summarizing the results of CARS measurements in diffuse filament ns pulse discharges in nitrogen, air, and their mixtures with $CO_2$, it can be concluded that adding $CO_2$ to nitrogen or air results in the accelerated vibrational relaxation of nitrogen and resultant temperature rise of the mixture, with the characteristic time of net relaxation thermalization process of $CO_2$, $\tau_{relax}$ ~ 1 ms·Torr. This suggests that adding $CO_2$ to nonequilibrium compressible flows of nitrogen or air may significantly change temperature and pressure distributions in the flow on this time scale, as well as the velocity field, as was indeed observed in Ref. [12].

### 3.6 Results and Discussion: Lean $H_2$-air Mixtures

#### 3.6.1 Time-resolved Vibrational Temperature and Rotational-translational Temperature

Figure 3.29 shows $N_2$(v = 0 - 2) vibrational level populations inferred from the broadband CARS spectra obtained without Nd:YAG laser injection seeding in a ns discharge pulse in a 3% $H_2$-air mixture, at t = 10 μs, 200 μs and 2 ms after the discharge pulse.

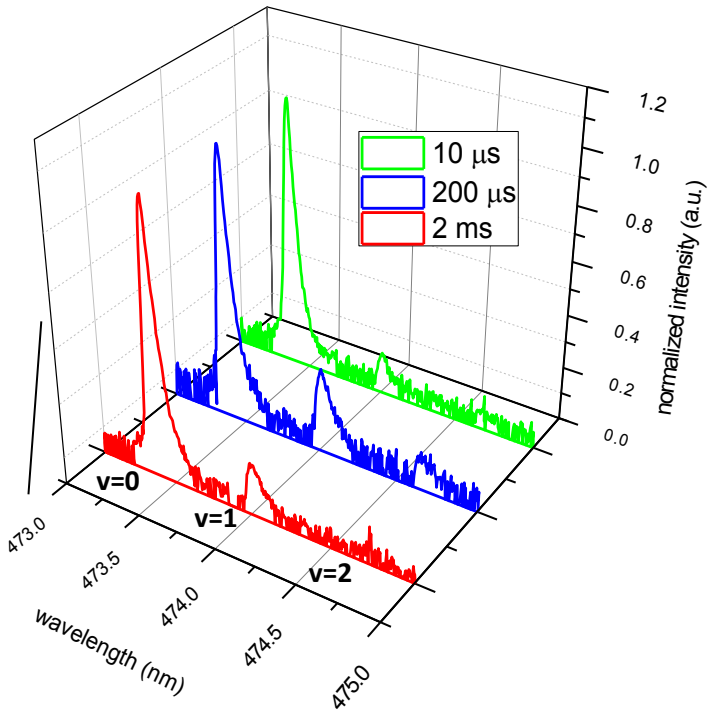


**Figure 3.29. Broadband CARS spectra $N_2$ (v = 0 - 2) taken in a ns pulse discharge in a 3% $H_2$-air mixture at P = 100 torr, at three different delay times after the discharge pulse. Pulse coupled energy is 7.5 mJ/pulse.**

CARS signal-to-noise ratio in $H_2$-air mixtures is somewhat lower compared to that detected in a ns pulse discharge in nitrogen and air at similar coupled energy, such that for $N_2$ vibrational bands only up to v = 2 can be detected (compare Figures 3.19 and 3.29). This is due to the higher electromagnetic interference (EMI) from the discharge. At t = 200 μs, the increase in normalized square-root peak intensities of v = 1 and v = 2 vibrational bands is readily apparent, compared to the spectrum take at t = 10 μs. At t = 2 ms, v = 1 band intensity decrease while v = 2 peak almost disappears.

Fig. 3.30 plots $N_2$(v = 0) vibrational band spectra in air and in the 3% $H_2$-air mixture, taken at t = 600 μs after the discharge pulse with Nd:YAG laser injection seeding, as well as best-fit CARSFT synthetic spectra. It can be seen that with injection seeding, the rotational structure of the v = 0 vibrational band is more pronounced, compared to the spectra plotted in Figure 3.23 and Figure 3.24, taken without injection seeding.

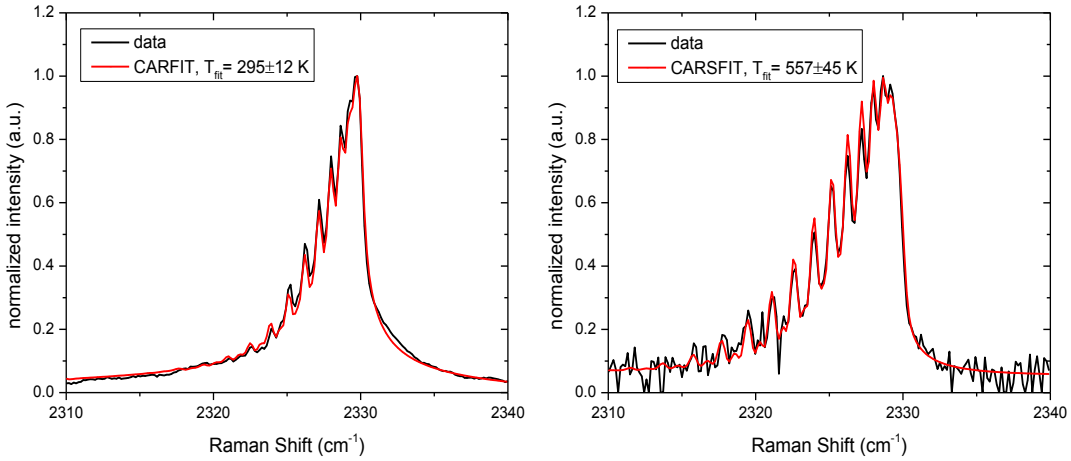


**Figure 3.30. Left: Comparison of the experimental CARS spectrum and best fit CARSFT synthetic spectrum used for the rotational-translational temperature inference in ambient air. Right: Comparison of the experimental CARS spectrum and best-fit CARSFT synthetic spectrum used for the rotational-translational temperature inference in a 3% $H_2$- air mixture at P = 100 Torr, at t = 600 μs after the discharge pulse. Coupled discharge pulse energy is 7.5 mJ/pulse.**

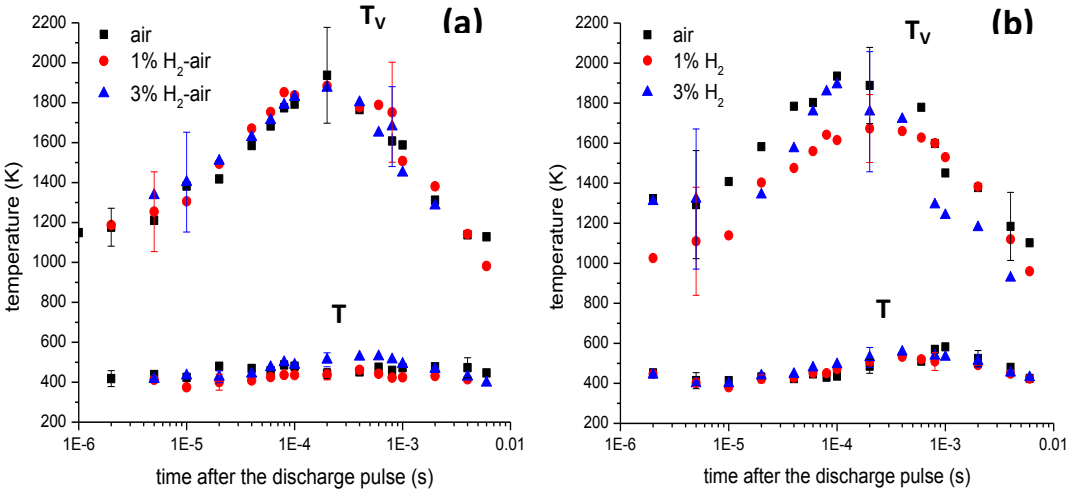


**Figure 3.31. Time-resolved $N_2$ vibrational temperature and rotational-translational temperature inferred from the CARS spectra in a ns pulse discharge in air and $H_2$-air mixtures at P= 100 Torr. Discharge pulse coupled energy is (a) 7.8 mJ/pulse and (b) 10.0 mJ/pulse.**

Figure 3.31 plots time-resolved $N_2$ first-level vibrational temperature and rotational-translational temperature in a ns pulse discharge in air and $H_2$-air mixtures at P = 100 Torr, at the coupled energy of 7.8 mJ/pulse and 10.0 mJ/pulse, respectively. It can be seen that in air, the vibrational temperature increases from approximately 1200 K at t = 1 μs to 1950 K at t = 100 μs, due to the downward V-V energy exchange discussed in Section 3.5 (see Equation 3.4), which reduces high $N_2$ vibrational level populations and increases $N_2$ (v = 1) population. Kinetic modeling calculations [5] also show that vibrational relaxation in a ns pulse discharge in air is controlled by the $N_2$ relaxation by O atoms, produced primarily during collisional quenching of electronically excited $N_2$ molecules generated by electron impact during the discharge pulse, see Equations 3.8 and 3.9. This results in the vibrational temperature reduction at t > 100 μs. Vibrational temperature decay at t > 1 ms is due to the radial diffusion from the filament [5]. At the coupled energy of 7.8 mJ/pulse, $N_2$ vibrational temperatures in $H_2$-air mixtures and in air are fairly close (see Figure 3.31(a)), indicating that at the present conditions the effect of $N_2$ vibrational relaxation by H atoms and water vapor is fairly insignificant.

A similar trend is observed in air and $H_2$-air mixtures at a higher discharge coupled energy, 10 mJ/pulse. At these conditions, reproducibility of the data becomes worse, most likely because the discharge becomes less stable. According to Figure 3.31, rotational-translational temperature in the discharge and the afterglow remains relatively low temperature, 400 – 600 K for both coupled energies, indicating strong vibrational nonequilibrium.

Time evolution of the rotational-translational temperature in air and in $H_2$-air mixtures at the discharge coupled energy of 10 mJ/pulse is illustrated in greater detail in Figure 3.32. At t = 2 – 10 μs, the results indicate a transient temperature reduction, which follows a "rapid" temperature rise on the time scale of t = 0.1 – 1 μs detected in our previous temperature measurements in a ns pulse discharge in air at 100 Torr [6] and in kinetic modeling calculations [5]. This effect is caused by rapid heating in air, dominated by the quenching of electronically excited $N_2$ molecules by atomic oxygen, with subsequent gasdynamic expansion of the filament resulting in a transient temperature drop. A gradual temperature rise at t = 10 μs – 1 ms, up to T = 530 – 580 K (See Figure 3.32), is also consistent with our previous measurement [6] and modeling predictions [5] in air, and is due to energy release during vibrational-translational (V-T) relaxation of nitrogen by O atoms, generated during quenching of electronically excited $N_2$ molecules by $O_2$ (Equation 3.8). Finally, temperature reduction at t > 1 ms is due to radial diffusion. Temperatures are measured in air and $H_2$ –air mixtures at the same delay time after the discharge are within several tens of degrees (see Figure 3.32), indicating that the effect of energy release in chemical reactions of hydrogen oxidation is relatively minor.

Summarizing, CARS measurements of $N_2$ vibrational populations and temperature after the discharge pulse in air and in $H_2$-air mixtures demonstrate that strong vibrational nonequilibirum is sustained at the present experimental conditions, up to $T_V \approx 1900$ K and T $\approx 500$ K at t = 200 μs.

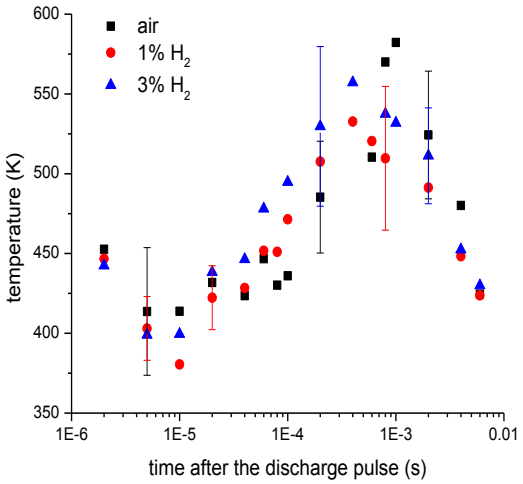


**Figure 3.32. Time-resolved rotational-translational temperature inferred from the CARS spectra in a ns discharge pulse in air and $H_2$-air mixtures at P = 100 Torr. The discharge coupled energy is 10.0 mJ/pulse.**

### 3.6.2 OH Number Density Measurements by Laser-induced fluorescence (LIF)

To study the possible effect of $N_2$ vibrational excitation on kinetics of radical species reactions in $H_2$-air mixtures excited by a ns pulse discharge, time-resolved absolute number density of OH was measured by Laser-Induced Fluorescence (LIF). These measurements have been done in a closely related but separate study [17, 44], in the same discharge cell that has been used for CARS measurements in air and $H_2$-air mixtures.

Laser induced fluorescence is a laser diagnostics technique that is widely used for in situ measurements of atomic and radical species in nonequilibrium reacting flows. In the present experiments studying vibrational energy transfer and kinetics of plasma chemical kinetics in lean $H_2$-air mixtures excited by a ns pulse discharge, single-photon LIF is used to

measure absolute, time-resolved number density of OH radicals, which plays an important role in kinetics of low-temperature plasma chemical fuel oxidation. Figure 3.33 shows the energy diagram of OH LIF kinetic processes. Basically, ground electronic state OH ($X^2\Pi$, v'=0) molecules are excited to an excited electronic state, OH ($A^2\Sigma$, v"=0) by absorbing a single photon from a pump beam. Excited OH ($A^2\Sigma$) molecules decay by fluorescence back to the ground electronic state and are also quenched collisionally, as indicated in Figure 3.33. In this work, resonant LIF is used, such that the fluorescence wavelength is the same as the pump laser wavelength = 308 nm. The absolute OH number density can be inferred from the fluorescence signal intensity, by absolute calibration using a signal with a known intensity, Rayleigh scattering.

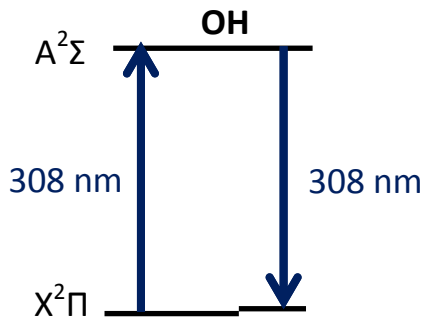


**Figure 3.33. OH LIF energy diagram.**

The schematic of the OH LIF laser diagnostic setup, shown in Figure 3.34, is discussed in greater detail in Ref. [44]. Briefly, the 532 nm output from a Nd:YAG laser (Continuum Model Powerlite 8010) is used to pump a tunable dye laser (Model Continuum ND6000), generating output at 615 nm, which is frequency-doubled in a type-I BBO crystal.

Two dichroic mirrors are used to separate the 308 nm second harmonic from the 615 nm fundamental (see Figure 3.34), creating a delay line. In this line, a half wave plate and polarizer combination is used to reduce the energy of the 308 nm beam. A Pellin-Broca prism separates the second harmonic from the remaining fundamental, and an identical prism is set symmetrically, to compensate for alignment changes of the 308 nm beam, as shown in Figure 3.35. The 308 nm beam is then focused into the same six-arm cross discharge cell as used in CARS measurements (see Figure 3.1), using a f = 500 mm lens. The beam passes through the holes in the electrodes, as shown in Figure 3.3. The measurement volume is kept in the intermediate field of the focused pump beam, to prevent non-linear effects or laser induced breakdown. The fluorescence is collected at 90̊, through a 2 inch UV fused silica window. A band pass filter (UG11 Colored Glass UV-Passing Filter, bandpass 275 – 375 nm), is placed in front of the camera lens to collect the fluorescence signal of the OH ($A^2\Sigma^+$, v'=0) → ($X^2\Pi$, v"=0) emission band at ~ 308 nm. The use of the resonant LIF increases interference due to the pump laser beam scattering off the electrodes. This effect is reduced by gating the ICCD camera. The 200 ns camera gate delay is set 3 ns after the end of the laser pulse, significantly reducing the laser scattering noise. The wavelength of the laser beam pumping the OH absorption transition, $R_2$ (2.5), λ = 307.792 nm, is monitored by a High Finesse Angstrom WE/6 wave meter, and the laser pulse energy, 3 – 5 μJ/pulse, is measured by a Scientech P09 power meter. In all present measurements, the laser energy is kept well below the saturation threshold, in the linear regime for OH LIF (≤ 8 μJ/pulse), to minimize photoionization and photo-dissociation.

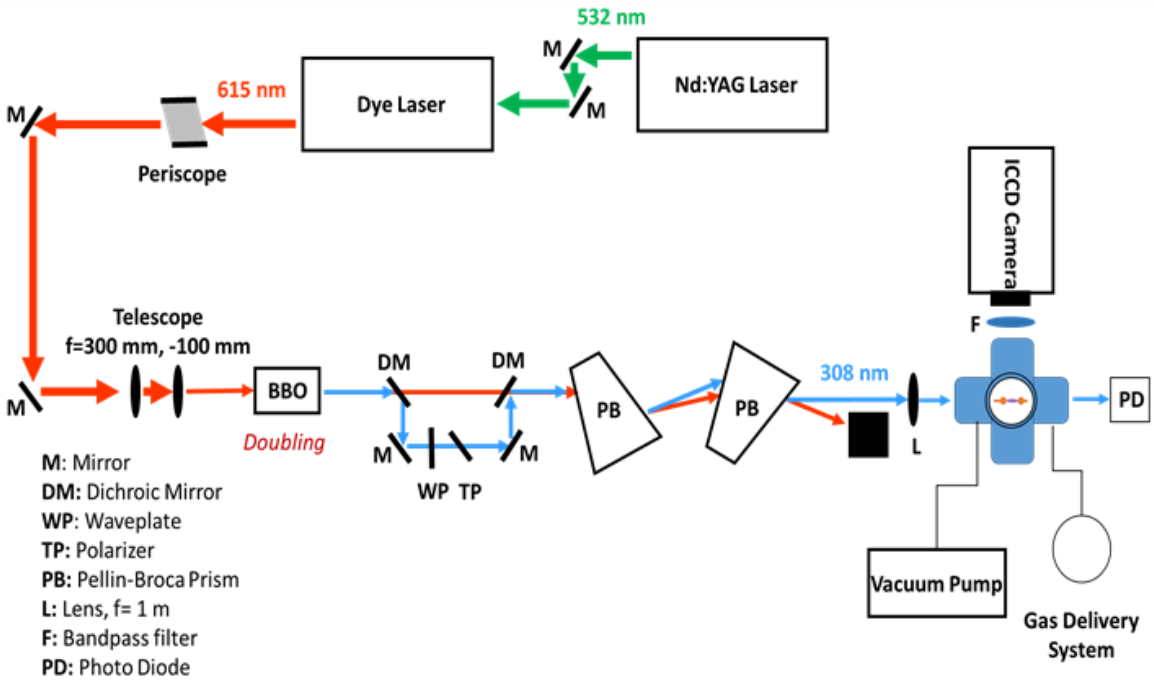


**Figure 3.34. Schematic of OH LIF optical diagnostic setup [44].**

The fluorescence signal is put on an absolute scale by measuring the fluorescence quenching rate, the convolution integral of the laser linewidth, and the absorption transition linewidth, and the efficiency of the signal collection optical system. The fluorescence quenching rate is measured directly at each set of experimental conditions, at t = 90 – 100 μs after the discharge pulse, when the fluorescence signal is near maximum. For this, the camera gate (5 ns wide) is shifted relative to the laser pulse, measuring the fluorescence signal decay. The quenching rate was inferred from the best exponential fit to the signal integrated over the central part of the discharge filament 4 mm long, the same region as used for [OH] measurements. Quenching rate inferred from the fluorescence decay signal integrated over the entire filament (8 mm long) was essentially the same (less than 1% difference). The convolution integral is measured in several $H_2$-air mixtures at t =

100 μs after the discharge pulse, by scanning the laser wavelength across the entire OH absorption transition and measuring the fluorescence signal at 10 different wavelengths. During the rest of the measurements, the laser is parked at the center of the absorption transition. The signal collection efficiency is determined via Rayleigh scattering calibration. For this, the cell is filled with nitrogen, and the scattering signal off nitrogen molecules is collected by the same optical system as the fluorescence signal. By keeping the laser pulse energy constant and varying the nitrogen pressure in the cell, the scattering signal intensity is measured vs. the number density, exhibiting a linear trend. The slope of this line provides the signal collection efficiency used for absolute calibration of the LIF signal. Gas temperature necessary to calculate the Boltzmann factor in the expression for the fluorescence intensity is taken from the CARS measurements discussed in Section 3.6.1.

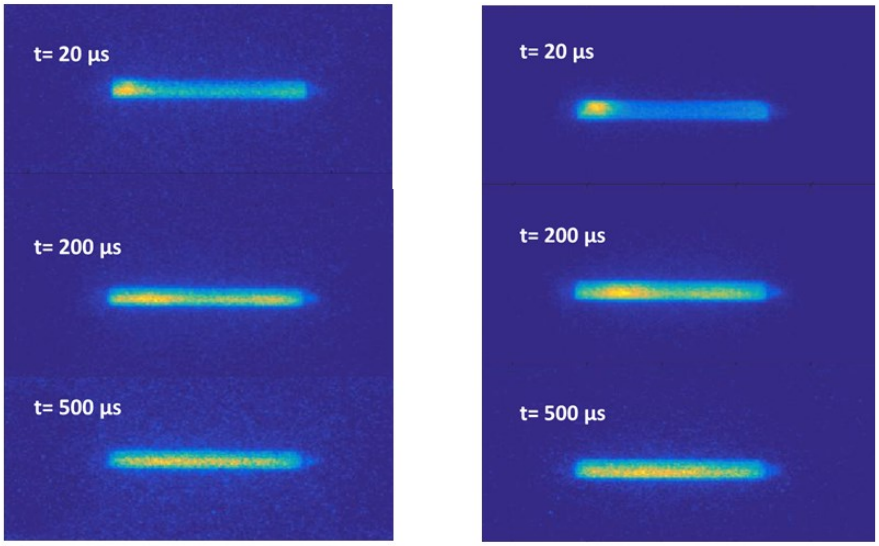


**Figure 3.35. OH LIF images in 3% $H_2$-air mixtures at P = 100 Torr, at different delay times after the discharge pulse. Grounded electrode on left, camera gate 200 ns, 100 shot accumulation. Left: coupled pulse energy 7.5 mJ/pulse, right: coupled pulse energy 10.0 mJ/pulse.**

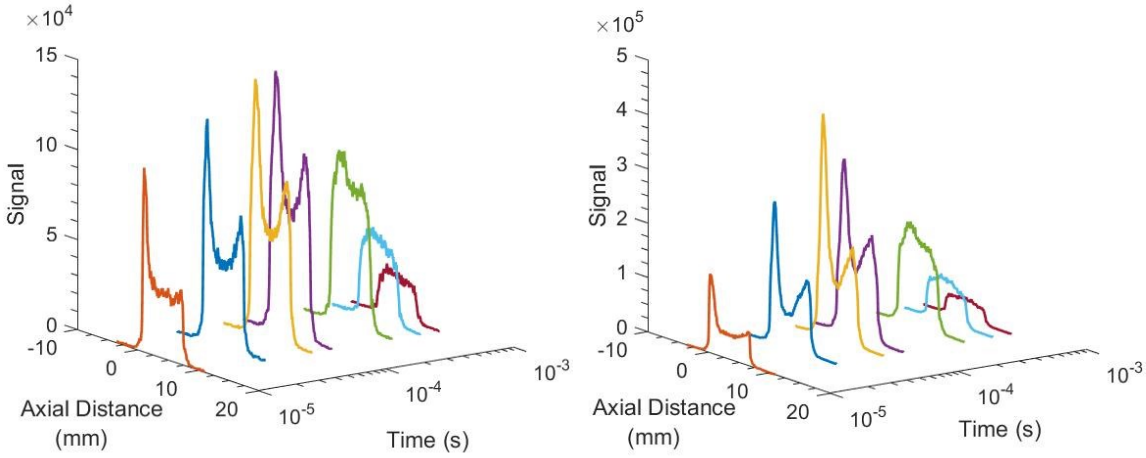


**Figure 3.36 OH LIF signal intensity distributions along the filament centerline in 3% $H_2$-air mixtures at P=100 Torr, at the conditions of Figure 3.35. Left: coupled pulse energy 7.5 mJ/pulse, right: coupled pulse energy 10.0 mJ/pulse. Grounded electrode is at x = 0 mm.**

Figure 3.35 shows OH LIF images taken in the 3% $H_2$-air mixture at P = 100 Torr, at different delay times after the discharge pulse, and at two values of discharge pulse energy, 7.5 mJ/pulse (left) and 10.0 mJ/pulse (right). Similar to plasma emission images shown in Figures 3.9 – 3.12, the grounded electrode is on the left. These images are accumulated over 100 laser shots, at a camera gate of 200 ns. From Figure 3.36, it is apparent that laser scattering off the electrodes is a minor factor. Time evolution of the OH LIF signal intensity distribution along the discharge filament centerline (integrated over the transverse region with 1 mm height) at these conditions is also illustrated in Figure 3.36.

From Figure 3.35, it can be seen that at short delay times after the discharge pulse, t ~ 10 μs, the LIF signal peaks near the grounded electrode (at x = 0 mm), with a lower intensity peak near the high-voltage electrode, t = 10 – 100 μs. The effect becomes more pronounced as the discharge pulse energy is increased from 7.5 mJ/pulse to 10 mJ/pulse (see Figure 3.37). This indicates that the specific energy loading into the plasma near the electrodes is higher compared to the rest of the discharge gap. At t > 100 μs, these maxima become less pronounced and gradually disappear, as shown in Figure 3.36. At t = 200 μs, LIF signal intensity between the discharge electrodes is more uniform and decays after t > 500 μs. Images taken in 1% and 5% $H_2$-air mixtures show the same trend.

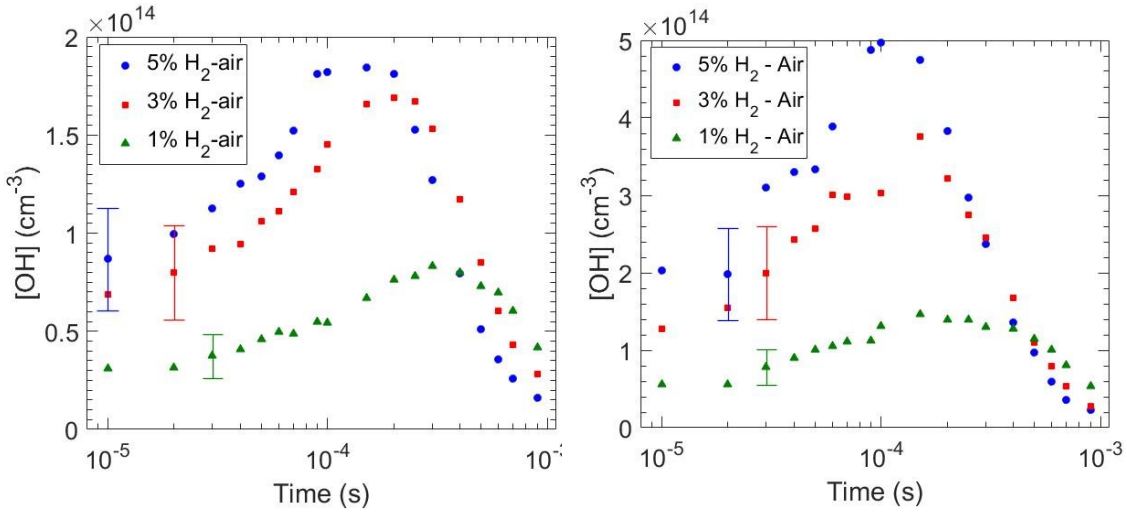


**Figure 3.37. Absolute OH number density integrated over the discharge filament vs. time delay after the discharge pulse in $H_2$-air mixtures. Left: coupled pulse energy 7.5 mJ/pulse; right: coupled energy 10.0 mJ/pulse.**

Figure 3.37 plots the absolute OH number density vs. time delay after the discharge pulse in three different $H_2$-air mixtures, at discharge coupled energy of 7.5 mJ/pulse and 10 mJ/pulse. OH number density is inferred from the LIF signal distributions, such as shown in Figures 3.35 and 3.36, integrated over the central region of the discharge filament region 4mm long, and calibrated using the procedure discussed in Ref. [44]. Gas temperature in the discharge afterglow, used to calculate absolute OH number density, is taken from CARS measurements in air at the same discharge pulse energy (see Figures 3.31 and 3.32). The combined uncertainty of the inferred OH number density is estimated to be ± 30%, with the uncertainty in the Rayleigh scattering calibration being the dominant factor.

### 3.6.3 Comparison with Kinetic Modeling Predictions

The quasi-zero-dimensional kinetic model is discussed in detail in our previous work [5]. Briefly, the model incorporate electron impact processed for $N_2$, $O_2$ and $H_2$, with cross sections taken from LXCat database [49]; reactions of excited electronic states of $N_2$, $O_2$, N and O [50-54]; air plasma chemistry [50]; state-specific vibration-translational (V-T) relaxation of nitrogen and vibrational-vibrational (V-V) energy transfer for $N_2$-$N_2$ [55]; and a mechanism of "conventional" hydrogen-oxygen chemical reactions [56] . Electron impact excitation of elecronic states of hydrogen is assumed to result in their dissociation. Vibrational excitation of $O_2$ is neglected, due to the low discharge input energy fraction, and $O_2$ is assumed to be rapidly thermalized. Effects of diffusion, conduction heat transfer, and convection are incorporated as quasi-zero-dimensional corrections.

The model is exercised using a combination of Boltzmann equation solver for plasma electrons Bolsig+ [57], predicting electron impact rate coefficients vs. electron temperature, and ChemKin-Pro, solving a set of species concentration equations, electron energy equation (a moment of Boltzmann equation), and heavy species energy equation. The Boltzmann solver is called only once for every set of experimental conditions (i.e. initial mixture composition), and electron impact rate coefficients are evaluated for a wide range of electron temperatures. The model also incorporates an interface pre-processor merging electron impact processes (with rate coefficients predicted by the Boltzmann solver), plasma chemical reactions, and conventional chemistry reactions, and assembling the input reaction kinetics data file in ChemKin format. The discharge power waveform coupled to

the plasma (used as the source term in the electron energy equation) is obtained from the measurements of discharge voltage and current waveforms, such as plotted in Figure 3.6.

Time-resolved discharge power, used as one of the model entries, is obtained from the experimental current and voltage waveforms (see Figure 3.6), with the power waveform scaled to account for the cathode voltage fall, which significantly reduces the energy coupled to the plasma outside the cathode layer [55]. Plasma filament diameter used in the model, d = 3.6 mm, is set to be the same as the FWHM of the plasma emission intensity determined from the ICCD images such as shown in Figure 3.11 and 3.12. Radial diffusion of species out of the discharge filament is accounted for as a zero-dimensional correction. Pressure variation in the filament due to sub-acoustic time scale heating and subsequent gas dynamic expansion is incorporated as discussed in Ref. [55].

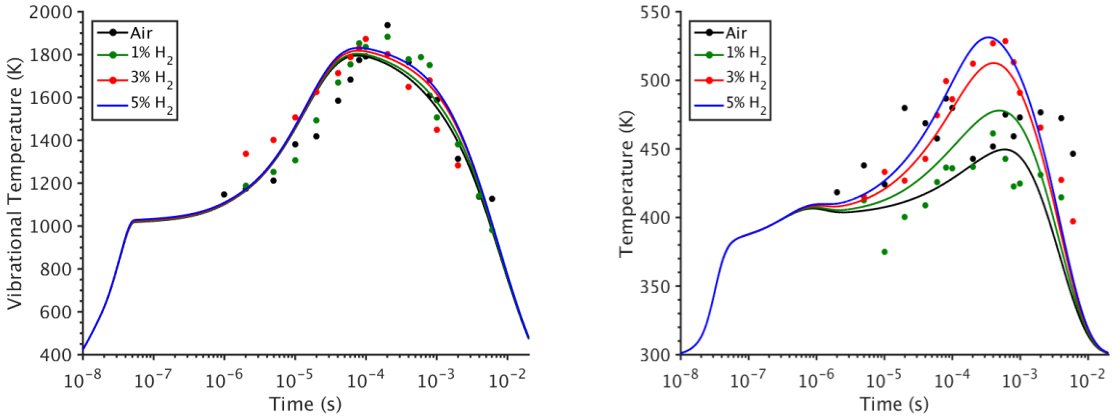


**Figure 3.38. Comparison of experimental and predicted $N_2$ vibrational temperature (left) and gas temperature (right) vs. time delay after the discharge pulse in air, 1%, and 3% $H_2$-air mixtures, at P = 100 Torr. Coupled pulse energy is 7.5 mJ/pulse.**

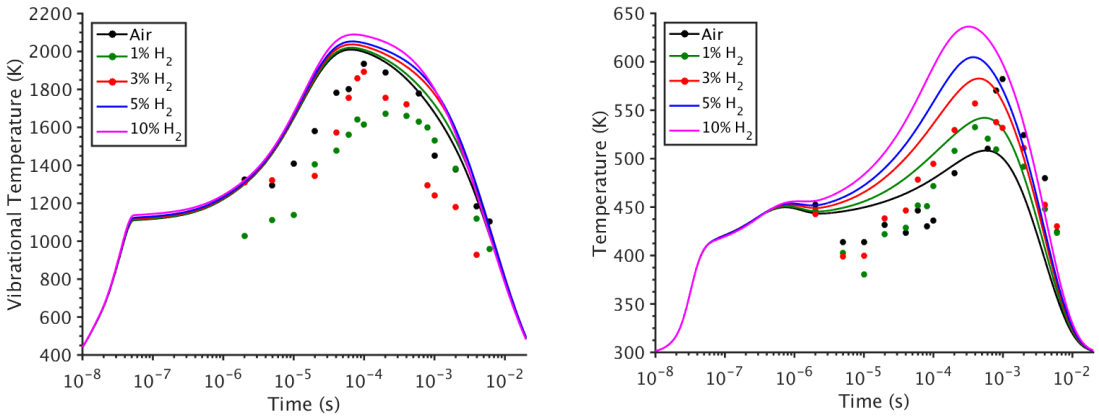


**Figure 3.39. Comparison of experimental and predicted $N_2$ vibrational temperature (left) and gas temperature (right) vs. time delay after the discharge pulse in air, 1%, and 3% $H_2$-air mixtures, at P = 100 Torr. Coupled pulse energy is 10 mJ/pulse.**

Figure 3.38 and Figure 3.39 compare experimental and predicted $N_2$ vibrational temperature (left) and gas temperature (right) vs. time delay after the discharge pulse in air, 1%, and 3% $H_2$-air mixture, at the coupled energy of 7.5 mJ/pulse and 10 mJ/pulse. It can be seen that the kinetic modeling predictions are in good agreement with the experimental data, indicating that the model correctly reproduces the effect of dominant energy thermalization processes over a wide range of time (1 μs – 10 ms). As discussed qualitatively in Section 3.5, $N_2$ vibrational temperature rise after the discharge pulse at t ~ 1 – 200 μs is caused by the "downward" $N_2$-$N_2$ V-V energy exchange, which depopulates high $N_2$ vibrational levels and increases the population of vibrational level v = 1, thereby increasing the "first-level" vibrational temperature defined by Equation 3.2. At t > 200 μs, vibrational temperature decays primarily due to the V-T relaxation by O atoms. The model also reproduces the trend for the temperature rise caused by the $N_2$-$N_2$ V-V exchange and $N_2$-O V-T relaxation in air, and by chemical energy release due to oxidation of hydrogen in

plasma chemical reactions in $H_2$-air mixtures. At t > 1 ms, the temperature decreases due to the radial diffusion. At the present conditions, V-V' energy exchange and V-T relaxation of $N_2$ by $H_2$ molecules,

$$N_2\ (v=1) + H_2\ (w = 0) \rightarrow N_2\ (v=0) + H_2\ (w=1) \qquad \text{(Equation 3.10)}$$

$$N_2\ (v=1) + H_2 \rightarrow N_2\ (v=0) + H_2 + \text{heat} \qquad \text{(Equation 3.11)}$$

$k_{VV'} = 1\times10^{-16}$ ($cm^3s^{-1}$) [58] and $k_{VT}$ ($N_2$-$H_2$) = $4\times10^{-16}$ ($cm^3s^{-1}$) [59], are relatively slow, such that they can be neglected.

Although H atoms generated during the discharge pulse, by electron impact dissociation and by quenching of the excited electronic states of nitrogen,

$$H_2 + e \rightarrow H + H + e, \qquad \text{(Equation 3.12)}$$

$$N_2{}^*(A^3\Sigma, B^3\Pi, C^3\Pi, a1\Sigma) + H_2 \rightarrow N_2\left(X^1\Sigma_g^+, v\right) + H + H, \qquad \text{(Equation 3.13)}$$

may contribute to $N_2$ relaxation, the kinetic modeling predictions indicate that the H atom number density is approximately two orders of magnitude lower than that of O atoms, such that V-T relaxation of $N_2$ by O atoms is the dominating vibrational relaxation process (see Equation 3.8). As a result, peak values of $N_2$ vibrational temperature in air and in $H_2$-air mixtures are fairly close, as shown in Figure 3.39(a). Increasing the discharge coupled energy from 7.5 mJ/pulse to 10.0 mJ/pulse does not change the dominant trends in the vibrational temperature evolution (compare Figures 3.38(a) and 3.39(a)). However, as can be seen in Figure 3.39 (a), at the higher discharge pulse energy, the kinetic model appears to overpredict the discharge energy fraction going to $N_2$ vibrational excitation by electron

impact, as well as the peak vibrational temperature. Both the effects of transient gas temperature reduction at t ~ 2 – 10 μs, caused by the gasdynamic expansion of the filament following its heating on sub-acoustic time scale [5], and the rate of the subsequent temperature rise caused by vibrational relaxation in air and by chemical energy release due to hydrogen oxidation in $H_2$-air mixtures are overpredicted. This is most likely due to an inaccurate representation of the time-dependent reduced electric field in the plasma by the present quasi-zero-dimensional model [45], which does not take into account kinetic processes in the cathode layer. However, peak temperature predicted by the model, up to T ~ 600 K at t = 300 μs, is consistent with the data (see Figure 3.39 (b)).

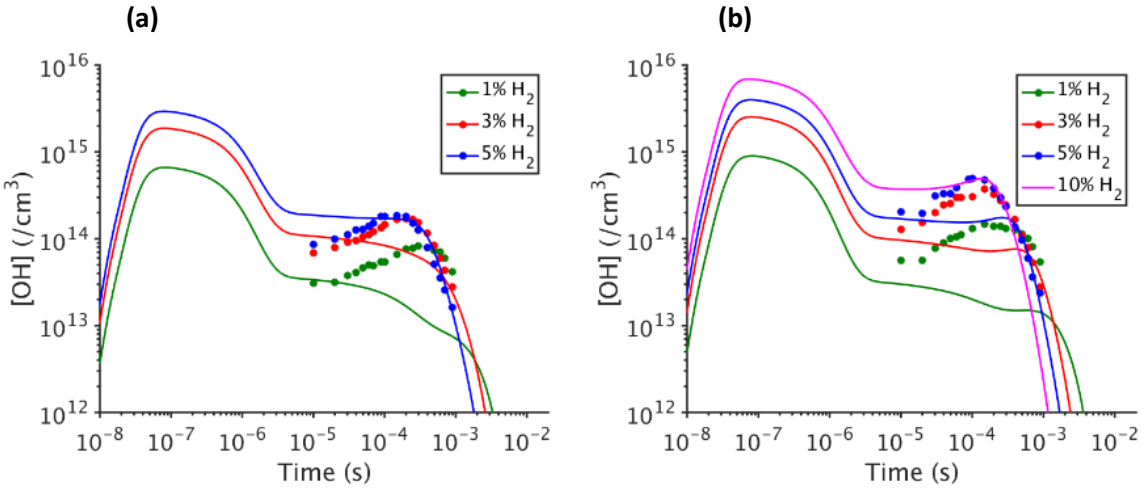


**Figure 3.40. Comparison of experimental and predicted absolute OH number density after the discharge pulse in air and $H_2$-air mixtures, at P = 100 Torr. Coupled energy (a) 7.5 mJ/pulse and (b)10.0 mJ/pulse.**

Figure 3.40 compares the experimental data and the modeling predictions for time-resolved absolute OH number density after the discharge pulse in three different $H_2$-air mixtures, with the discharge coupled energy of 7.5 mJ/pulse and 10.0 mJ/pulse, respectively. At the lower pulse energy of 7.5 mJ/pulse, the model reproduces peak OH number density for a 3% $H_2$-air mixture, but underpredicts peak OH number density for 1% $H_2$-air mixture and overpredicts it for 5% $H_2$-air mixture (see Figure 3.40(a)). In all three mixtures at 7.5 mJ/pulse, the model fails to reproduce the rise in the OH number density at t = 10 – 200 μs. Although a gradual temperature rise on this time scale is observed in the CARS temperature measurements (see Figure 3.31), the rates of OH formation reactions are still too slow to explain the overshoot in the OH number density. Since at the present conditions the discharge filament is generated slightly off the symmetry axis (see Figures 3.11 and 3.12), it is possible that the overshoot is caused by rapid diffusion of H atoms from the filament centerline into the line of sight of the LIF laser beam, on the time scale of several tens of μs, thus accelerating the rate of reaction,

$$H + O_2 \rightarrow OH + O \qquad \text{(Equation 3.14)}$$

and resulting in OH number density overshoot.

At the coupled energy of 10.0 mJ/pulse, note that the temperature maxima predicted by the model in 1-5% $H_2$-air mixtures approximately coincide in time with the transient maxima in OH number density, predicted at t ~ 300 μs – 1 ms (compare Figures 3.39(b) and 3.40(b)). This occurs primarily due to a significant increase of the rate coefficient the reaction of Equation 3.14, which is strongly temperature dependent, $k = 1.62\times10^{-10}\exp(-7470/T)$ $cm^3/s$ [60].

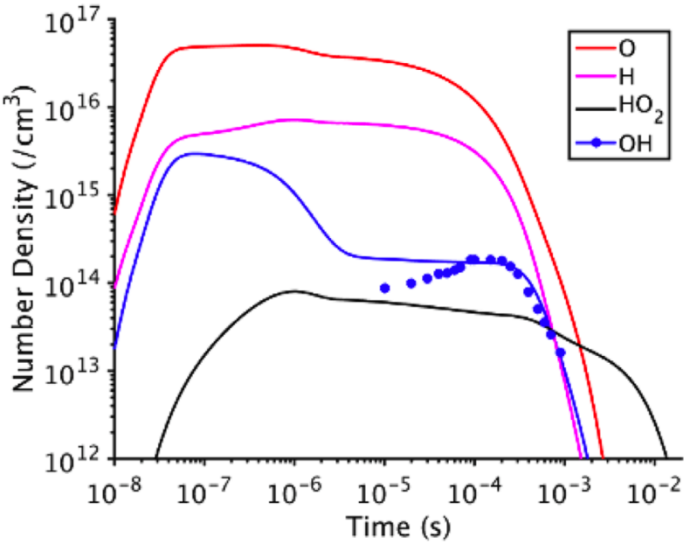


**Figure 3.41. Predicted radical species number densities and measured OH number density vs. time delay after the discharge pulse in a 5% $H_2$-air mixture at P = 100 Torr. Coupled energy is 7.5 mJ/pulse.**

Figure 3.41 plots dominant radical species number densities (ground state $O(^3P)$ atoms, H atoms, OH, and $HO_2$) vs. time delay after the discharge pulse in a 5% $H_2$-air mixture, Both O atoms and H atoms are generated in the discharge by the electron impact dissociation of molecular oxygen and hydrogen, as well as by collisional quenching of electronically excited nitrogen molecules, $N_2$*, by $O_2$ and $H_2$. A strong overshoot of OH number density predicted by the model on a ~ 100 ns time scale is due to OH formation in a reaction of electronically excited $O(^1D)$ atoms with molecular hydrogen,

$$O(^1D) + H_2 \xrightarrow{k_1} OH + H, \qquad \text{(Equation 3.15)}$$

On the time scale of t ~ 1μs, OH decays by the reaction with hydrogen,

$$OH + H_2 \overset{k_2}{\rightarrow} H_2O + H \qquad \text{(Equation 3.16)}$$

which is also an additional source of H atoms. On the time scale of t ~ 3 – 300 μs, OH is formed by reactions

$$H + O_2 + M \overset{k_3}{\rightarrow} HO_2 + M \qquad \text{(Equation 3.17)}$$

$$O + HO_2 \overset{k_4}{\rightarrow} OH + O_2 \qquad \text{(Equation 3.18)}$$

$$H + O_2 \overset{k_5}{\rightarrow} OH + O \qquad \text{(Equation 3.19)}$$

and decays by the reaction

$$OH + O \overset{k_6}{\rightarrow} H + O_2 \qquad \text{(Equation 3.20)}$$

as well as by the reaction of Equation 3.16. Using a quasi-stationary approximation, OH number density on this time scale can be described by the following equation,

$$[OH] \sim \frac{[H][O_2](k_3 \cdot [M] + k_5)}{[O] \cdot k_6 + [H_2] \cdot k_2} \qquad \text{(Equation 3.21)}$$

which is in very good agreement with the full kinetic model prediction. From Equation 3.21, it can be seen that the OH number density in the afterglow basically follows the number density of O and H atoms (the latter is also strongly affected by the radial diffusion from the filament at t > 100 μs), as well as the gas temperature, which affects the reaction rate coefficients of OH formation and decay (primarily Equation 3.19).

Adding the reaction of vibrational energy transfer from $N_2$ to $HO_2$ (Equation 3.1), to the kinetic model demonstrated that it does not enhance the rate of OH production. Basically, at the present conditions nearly every $HO_2$ radical formed by a three-body reaction (Equation 3.17) is rapidly converted to OH by Equation 3.18. Since the reaction of

vibrational energy transfer from $N_2$ to $HO_2$ competes directly with this process, it results in net reduction of OH number density on the time scale of 10 – 100 μs. Therefore at the present conditions, the role of vibrational energy transfer from $N_2$ to $HO_2$ and OH kinetics remains insignificant.

The kinetic model also includes kinetics of vibrationally hydrogen molecules to estimate OH formation by the reaction of O atoms with $H_2(v)$:

$$O + H_2(v) \rightarrow OH + H. \qquad \text{(Equation 3.22)}$$

Vibrationally excited $H_2(v)$ is generated by electron impact during the discharge,

$$H_2 + e \rightarrow H_2(v) + e, \qquad \text{(Equation 3.23)}$$

followed by V-V energy transfer between $H_2(v)$ molecules and V-T relaxation by O atom

$$H_2(v) + H_2(w) \rightarrow H_2(v-1) + H_2(w+1) \qquad \text{(Equation 3.24)}$$

$$H_2(v) + O \rightarrow H_2(v-1) + O + \text{heat} \qquad \text{(Equation 3.25)}$$

However, the modeling predictions demonstrated that although reaction of Equation 3.22 occurs on the same time scale as the OH overshoot, a few hundred μs, its effect on the OH production is fairly insignificant, mainly due to the rapid relaxation of $H_2$ generated in the discharge by O atoms, $[O] \approx 5\times10^{16}$ $cm^{-3}$ (see Figure 3.41).

# Chapter 4. Characterization of Microwave Discharge in Nitrogen and Carbon Dioxide

## 4.1. Introduction

As discussed in Chapter 1, energy efficiency of $CO_2$ dissociation in thermal plasmas is limited by equipartition of energy among the molecular energy modes. Energy-efficient $CO_2$ dissociation in thermal plasmas also requires rapid cooling of the reaction products, to reduce the effect of reverse reactions. In non-thermal equilibrium plasmas, energy efficiency of $CO_2$ dissociation can be improved significantly if the discharge energy is channeled into $CO_2$ vibrational energy modes.

The objective of the present work is to characterize microwave discharge plasmas sustained in nitrogen and $CO_2$ (specifically, to measure vibrational and translational-rotational temperatures) by CARS spectroscopy. Nitrogen is chosen as one of the representative test gases since it is readily accessible to CARS measurements and because the discharge energy fraction going into $N_2$ vibrational excitation by electron impact is typically very high, comparable with that in $CO_2$ plasmas [23]. Also, vibrational relaxation rates in nitrogen are significantly slower compared to that of $CO_2$, such that vibrational temperature and rotational-translational temperature measurements in nitrogen would provide an upper bound estimate of vibrational nonequilibrium in $CO_2$. Finally, due to the rapid vibrational energy transfer from $N_2$ to the asymmetric stretch vibrational mode of $CO_2$ (see Chapter 3), plasma chemical dissociation of $CO_2$ in $N_2$-$CO_2$ mixtures is one of the possible experimental embodiments of this process.

## 4.2 Microwave Discharge Reactor

The microwave discharge reactor used in the present work consists of the following four parts: loop coupler, 3-stub tuner, applicator, and the discharge test section, as shown in Figure 4.1 and Figure 4.2. The loop coupler is a rectangular cross section aluminum waveguide WR-340 with cross section dimensions of 86.4 × 43.2 $mm^2$, connected to a 2.45 GHz InitSF microwave plasma generator by four N-type coaxial cables [25, 28], used to power the microwave discharge. The microwave generator can be operated in either cw or pulsed mode, generating a microwave discharge in a transverse magnetic mode $TM_{10}$ in a rectangular shape cavity with a quartz tube, 30 mm outer diameter and 15 cm long, inserted into the cavity. The 3-stub tuner, with movable stubs made of copper cylinders, is used to adjust the impedance of the load in order to minimize the power reflected back to the microwave generator. The microwave electric field in the cavity and the power coupled to the plasma are calculated from the input power of the microwave generator and reflected power going back to the microwave generator, using ANSYS HFSS electromagnetic software package [61]. These calculations also predict that more than 95% of the incident microwave power is coupled to the plasma.

The applicator, made of aluminum, has a circular port 30 mm in diameter, through which a 15 cm long quartz tube of the same outside diameter is inserted (see Figure 4.1). The microwave discharge plasma is generated inside the quartz tube. The discharge test section is comprised of the quartz tube with the inside diameter 27 mm, a flow injection flange with an optical access window made of quartz, and an aluminum exhaust tube with the second optical access window, also made of quartz, as shown in Figure 4.1. The flow injection flange, which has two tangential injection nozzles, is connected to one end of the

quartz tube (see Figure 4.2). When the flow enters the quartz tube through the injection nozzles, a swirling flow is generated, enhancing convection cooling of the tube wall. At the design operating conditions, the microwave discharge plasma is generated near the center of the quartz tube, away from the walls. Due to a relatively high leak rate of the discharge reactor (~4 Torr/min), the discharge is operated at a high flow rate of 10-15 SLM, to reduce the impurity level in the discharge section. The aluminum tube, 25 cm long and 27 mm inner diameter, is attached to the exit end of the quartz tube and is connected to vacuum pump (model GE 5KC47RG723X). Two quartz windows, one in the injection flange and the other in the exhaust tube, provide optical access to the plasma, used for CARS diagnostics. Additional optical access is provided by a circular port at the end of the applicator, labeled in Figure 4.2, through which plasma emission spectra can be taken. Both the injection flange and the exhaust tube are cooled by water, to prevent their overheating and damaging the vacuum seal O-rings between the flange, the exhaust tube, and the quartz tube.

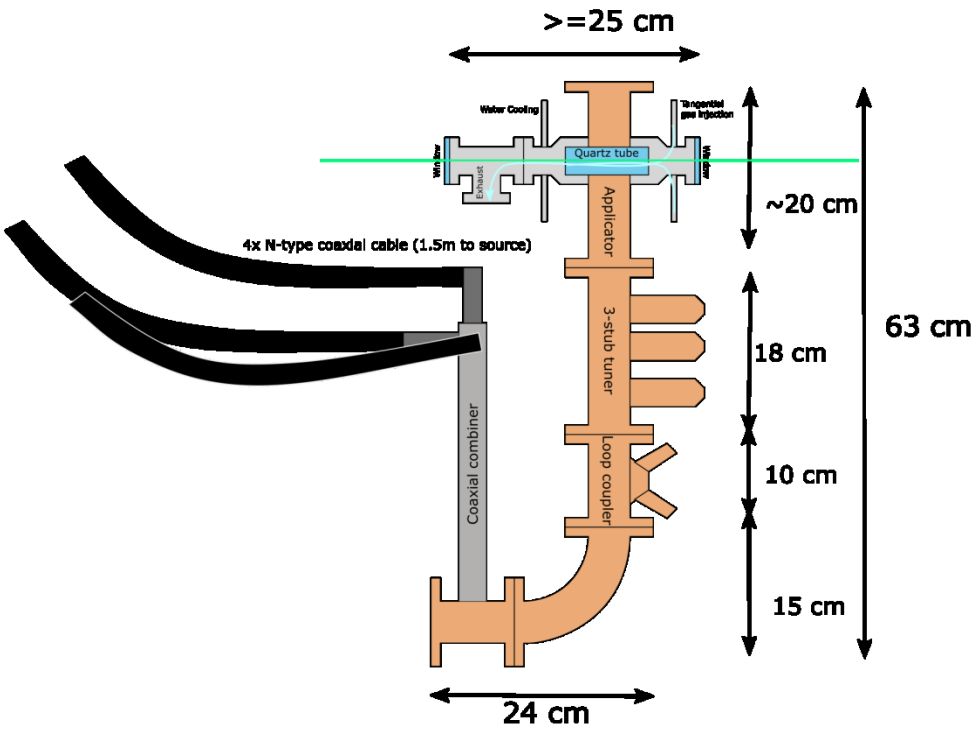


**Figure 4.1. Schematic of the microwave discharge reactor.**

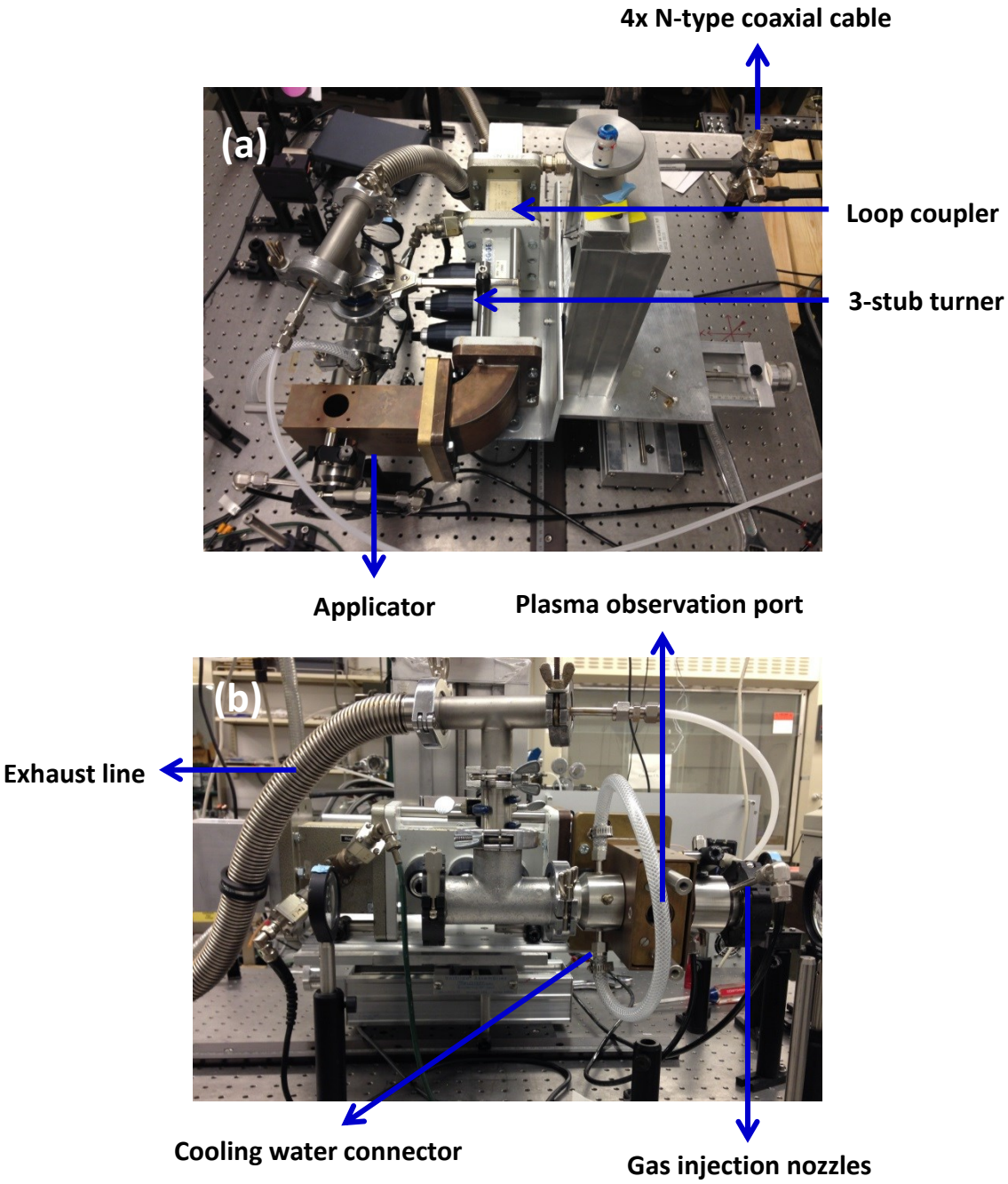


**Figure 4.2. Photographs of (a) microwave plasma generator and (b) discharge test section.**

### 4.3. CARS Optical Setup

The optical setup for the CARS system used for the measurements in the microwave discharge reactor is the same as described in Section 3.4, with the exception of a telescope lens pair placed in the optical path of the pump/probe beam before the focusing lens with a 150 mm focal distance, to increase the diameter of the beam, as shown in Figure 4.3. The lens pair used in the studies of a diffuse filament by a ns pulse discharge (Chapter 3) is composed of two positive lenses with focal lengths of 66 mm and 125 mm (see Figure 3.16). In order to achieve a longer CARS probe length, in the studies of a microwave discharge in $N_2$ and $CO_2$, the composition of a negative lens (f = -150 mm) and a positive lens (f = 100 mm) is used. The spatial resolution of CARS measurements at these conditions is determined by traversing a microscope slide glass 1 mm thick in the direction of the laser beams. The results are shown in Figure 4.4, indicating that 95% of the CARS signal is generated over a distance of approximately 17 mm. In the CARS signal collection optical path, a mechanical chopper wheel is placed before the spectrometer slit, such that the plasma emission is reduced by more than 90%, thus allowing a longer CARS spectra integration time. The chopper wheel driver generates a 10 Hz sync out signal, which is used as the "master clock" externally triggering the DG 656 delay generator, to produce two 10 us duration square-shaped signals to trigger the flash lamp and the Q-switch of the Nd:YAG laser. By varying the time delay between the microwave discharge pulse and the signals sent to trigger the laser, the CARS signal from the microwave discharge plasma can pass through the chopper wheel blocking the plasma emission and reach the spectrometer.

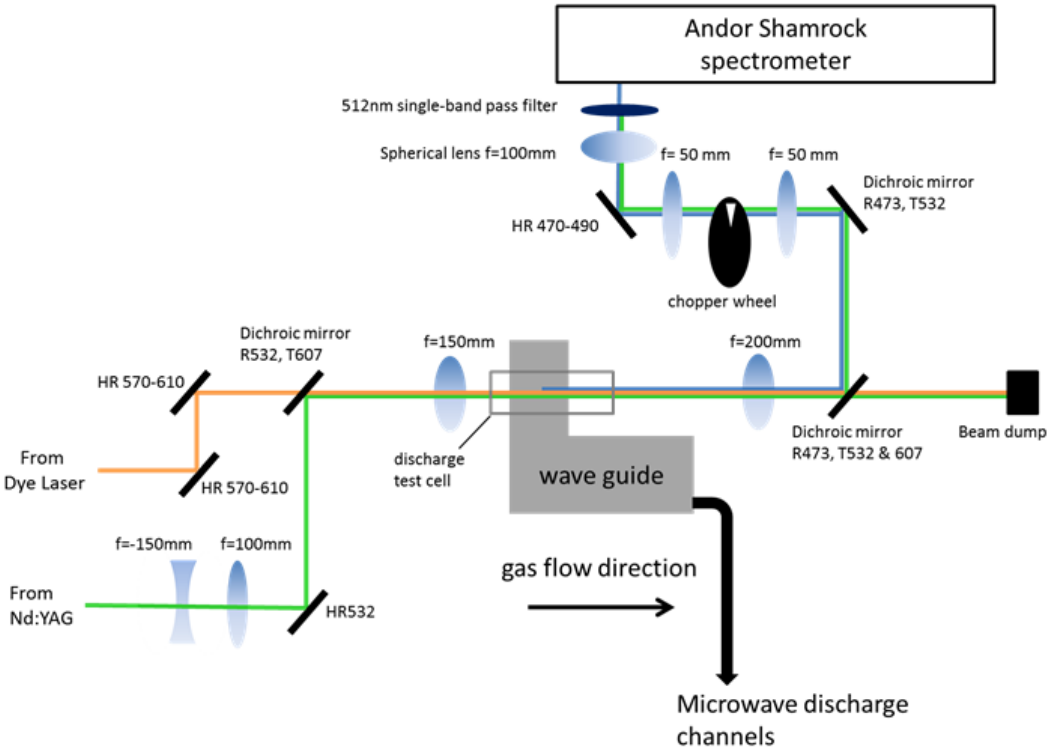


**Figure 4.3. Schematic of the CARS setup for the measurements in a microwave discharge in $N_2$ and $CO_2$.**

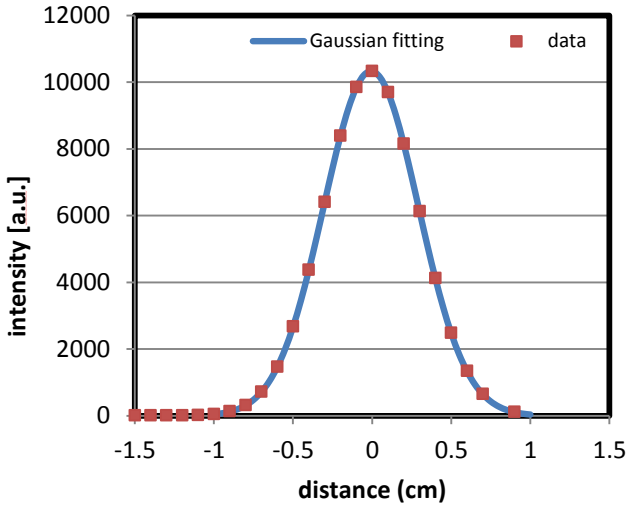


**Figure 4.4. Axial distribution of the non-resonant signal from a 1 mm thick microscope slide glass moved along the direction of the laser beams, illustrating that 95% of the CARS signal originates over a 17 mm long region. The focal lengths of the telescope lens pair are -150 mm and 100 mm, respectively.**

For CARS measurement in a microwave discharge in nitrogen, Kiton Red 620 (KR620) and Rhodamine 640 (R640) dye mixture is used in the broadband dye laser, producing broadband output with the wavelength ranging from 602 to 609 nm, centered approximately at 605 nm (see Figure 3.14). Figure 4.5 shows the broadband dye laser output spectrum, obtained by taking a non-resonant signal (NRS) generated in 1 atm argon in the quartz tube of the discharge section (with the discharge turned off). Changing the dye to a mixture of Rhodamine 590 (R590) and Rhodamine 610 (R610) gives access to the $CO_2$ symmetric vibrational stretch mode (100 → 000, Raman shift of 1338 $cm^{-1}$).

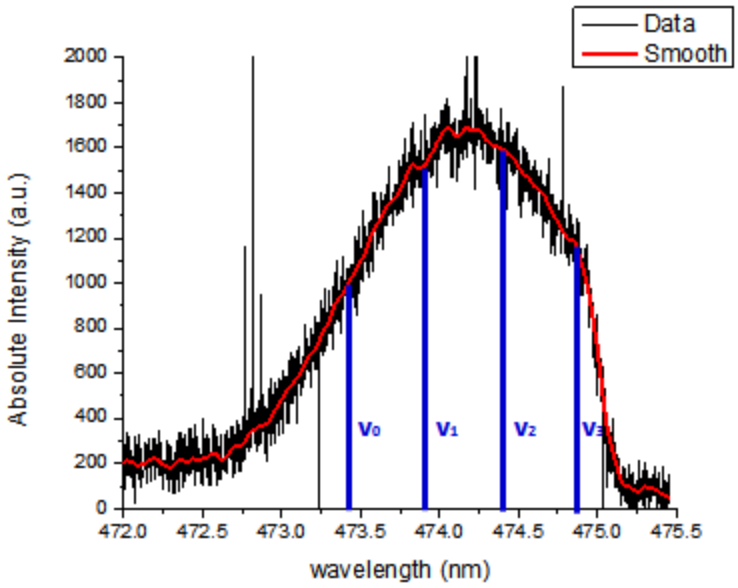


**Figure 4.5. Non-resonant background signal from 1 atm of argon, illustrating the broadband dye laser output spectrum, plotted along with the locations of first four $N_2$ vibrational levels.**

### 4.4. Results and Discussion: Microwave Discharge in Nitrogen

Figure 4.6 shows a photograph of a cw microwave plasma sustained in the flow of $CO_2$ in the quartz tube, at the pressure of P = 200 Torr, flow rate of 10 SLM, and input microwave power of 175 W. At these conditions, the plasma is located near the center of the quartz tube. However, the position of the plasma is very sensitive to the load impedance, which is adjusted by moving the stubs in the three-stub tuner. Changing the gas from $CO_2$ to $N_2$ produces a similar result, with the microwave plasma sustained near the center of the quartz tube.

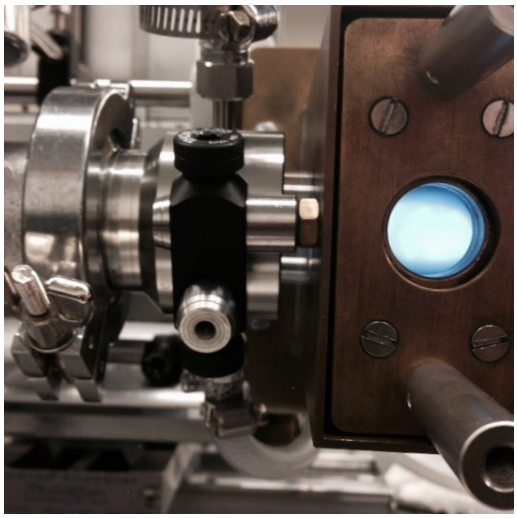

**Figure 4.6. Photograph of a cw microwave plasma in 200 Torr of $CO_2$ at the flow rate of 10 SLM and input microwave power of 175 W.**

Figure 4.7 compares a typical CARS spectrum taken in a microwave discharge in nitrogen at the pressure of P = 200 Torr and the flow rate of 15 SLM with the best-fit CARS synthetic spectrum. The experimental spectrum is taken with injection seeding of the

Nd:YAG laser turned on, to reduce the pump/probe laser output linewidth and improve the spectral resolution, such that the rotational structure of the $N_2$ (v = 0) band is partially resolved. The microwave generator is operated in a cw mode, at the input power of 175 W. The rotational-translational temperature in the plasma inferred from the CARFT spectrum is T = 2000 ± 200 K. At these high-temperature, quasi-steady-state conditions, it is almost certain that the population of $N_2$ vibrational level v = 1 represents an equilibrium population, indicating that the microwave discharge plasma is of near thermal-equilibrium.

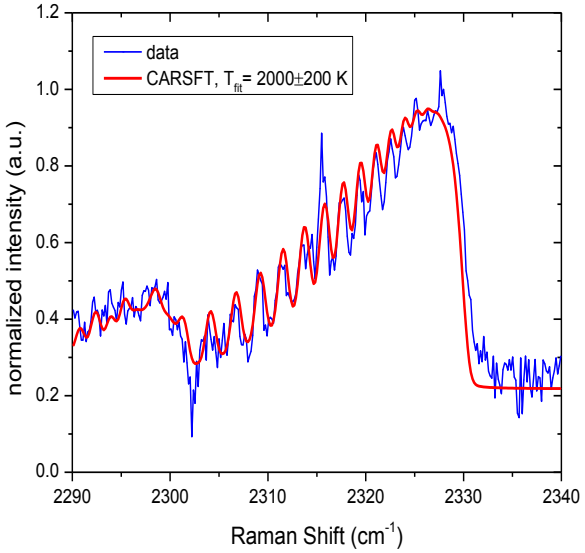


**Figure 4.7. Comparison of a CARS spectrum and a CARSFT synthetic spectrum in a cw microwave discharge in nitrogen. Pressure is 200 Torr, flow rate is 15 SLM, coupled microwave power is 175 W. The microwave generator is operating in a cw mode, the spectrum is taken near the center of the plasma.**

Figures 4.8 and 4.9 show schematically the locations where the temperature was measured at different radial and axial locations in the plasma, and in the afterglow downstream of the plasma. For all data points shown in these figures, the measurements are taken in nitrogen at the flow rate of 15 SLM, pressure of 200 Torr, and cw microwave input power of 175 W. It can be seen that the highest temperature, T = 2000 ± 200 K, is achieved near the center of the plasma, as expected. Near the periphery of the plasma, closer to the quartz tube wall, the temperature gradually decreases to approximately T = 800 K, again as expected. Figure 4.9 shows the temperature measurement locations downstream of the plasma. Figure 4.10 plots radial and temperature distributions in the plasma and in the afterglow. From Figure 4.10, it is evident that the temperature in the afterglow remains very high. Because of this, $N_2$ number density and the signal-to-noise at multiple locations downstream of the discharge were so low that CARSFT could not generated an adequate fit of the experimental CARS spectra, such that the temperature inference was not feasible. This is the reason for the "missing" data points in Figure 4.8. Temperatures measured near the quartz wall remains relatively low, T = 500 - 700 K (see Figure 4.10).

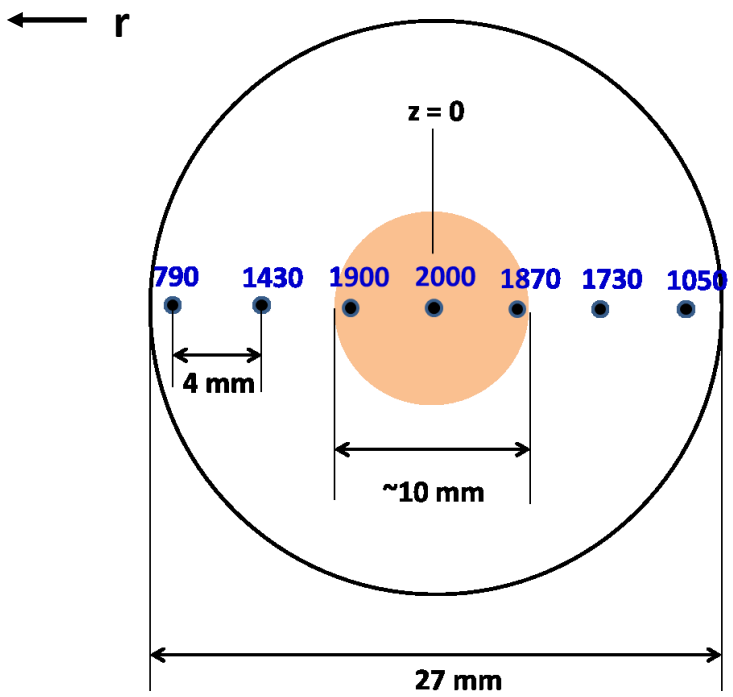


**Figure 4.8. A radial temperature distribution in the center of the microwave discharge plasma (at z = 0) at the conditions of Figure 4.7. Temperatures are in degrees Kelvin.**

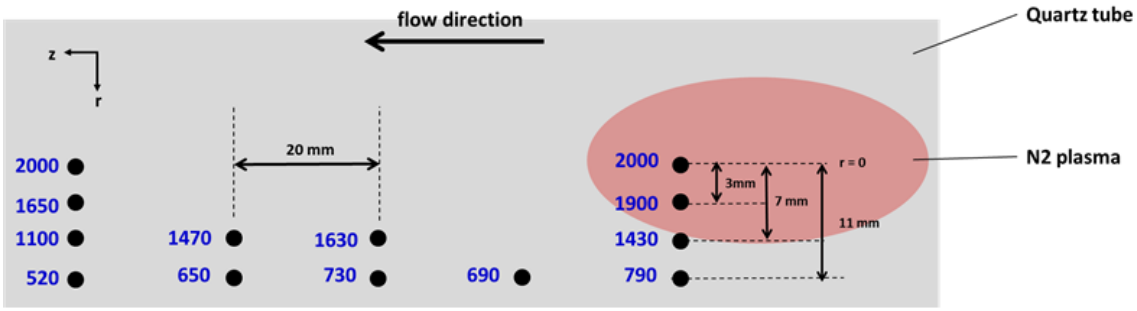


**Figure 4.9. Radial and axial temperature distributions downstream of the plasma at the conditions of Figure 4.7. Temperatures are in degrees Kelvin.**

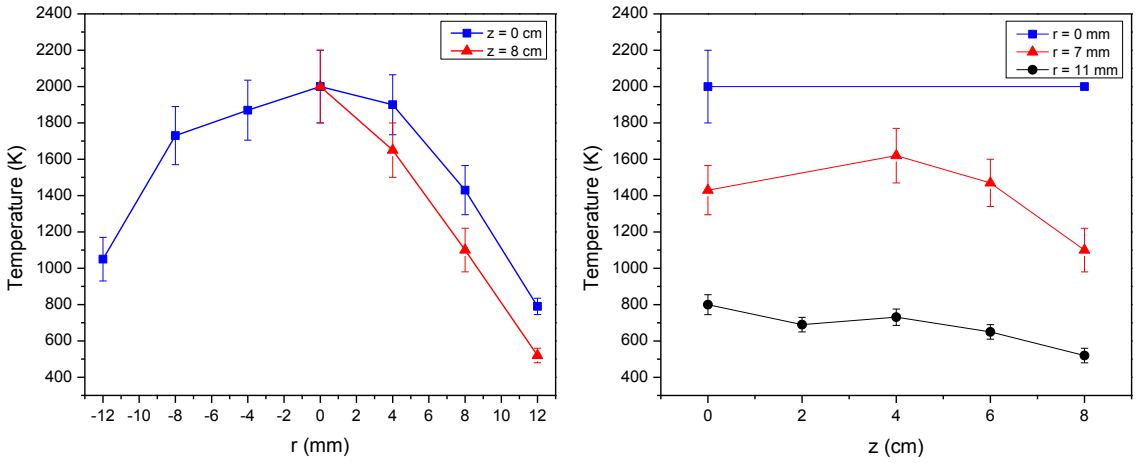


**Figure 4.10. (a) Radial temperature distributions at the plasma center (at z = 0 cm) and in afterglow (z = 8 cm); (b) axial temperature distributions in the afterglow at r = 5 mm and 11 mm (near the wall).**

The results of Figures 4.8 to 4.10 demonstrate that the temperature in a cw microwave plasma is very high, even at relatively high flow rates used to enhance the convective cooling. At these conditions, the axial flow velocity near the center of the quartz tube, estimated based on pressure, flow rate, and the temperature distribution, is approximately 330 cm/s. Clearly, to achieve strong vibrational nonequilibrium that would make $CO_2$ dissociation process more efficient, either the flow velocity (i.e. the flow rate) needs to be increased significantly or the microwave power needs to be reduced. Further increase of the flow rate would be incompatible with the pumping capacity available in the present apparatus. The reduction of the microwave power makes the discharge unstable. To reduce the temperature in the plasma and achieve vibrational nonequilibirum, in the subsequent experiments the microwave power generator was operated in the pulsed mode.

To generate a pulsed microwave plasma, the microwave generator was operated in a pulsed mode, at the repetition rate of 1 kHz, and duty cycle of 5.5%, with peak input power of ~ 180 W (close to the input power in a cw mode), at nitrogen pressure of 200 Torr and flow rate of 15 SLM. Thus, although the microwave discharge power during the pulse did not change significantly, the discharge was operated at a low duty cycle. Figure 4.11 shows a CARS spectrum with the best fit CARSFT synthetic spectrum in the center of the plasma (i.e. r = 0 and z = 0) at these conditions, with the best fit temperature of T = 1780 ± 150 K. The results of temperature measurements at these conditions are similar to the ones plotted in Figure 4.10.

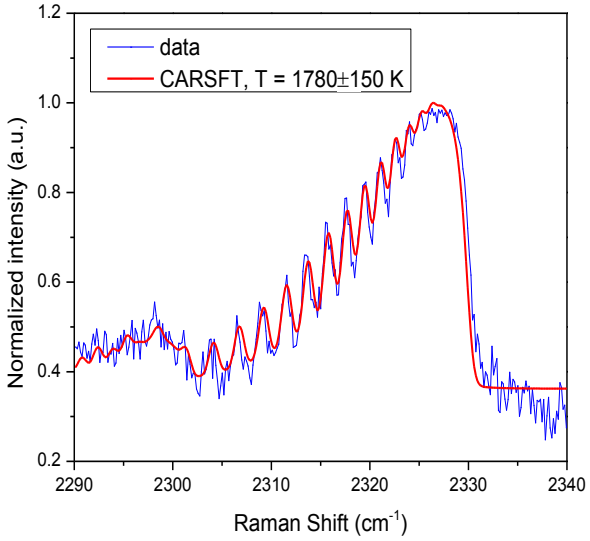


**Figure 4.11. Comparison of an experiemental CARS spectrum and CARSFT synthetic spectrum in a pulsed microwave discharge plasma in nitrogen. Pressure is 200 Torr, flow rate is 15 SLM, coupled microwave power is 180 W, duty cycle is 5.5%. The spectrum taken near the center of the plasma (z = 0, r = 0).**

After this, the microwave discharge duty cycle was reduced further to 0.6%, at the repetition rate of 40 Hz (discharge pulse duration of 150 μs). At this very low duty cycle, the discharge was operated in nitrogen at a lower pressure of 40 Torr. At these conditions, impedance matching controlled by the 3-stub tuner has become worse, with significant fraction of the power, 20-70%, reflected back to the microwave generator after the first 75 μs of the pulse. This is illustrated in Figure 4.12, which plots the raw forward and reflected relative power waveforms measured by an oscilloscope, before they processed by the ANSYS HFSS software package. The CARS spectra are taken every 10 μs during the microwave discharge pulse, as shown in Figure 4.12, and every 100 μs after the pulse.

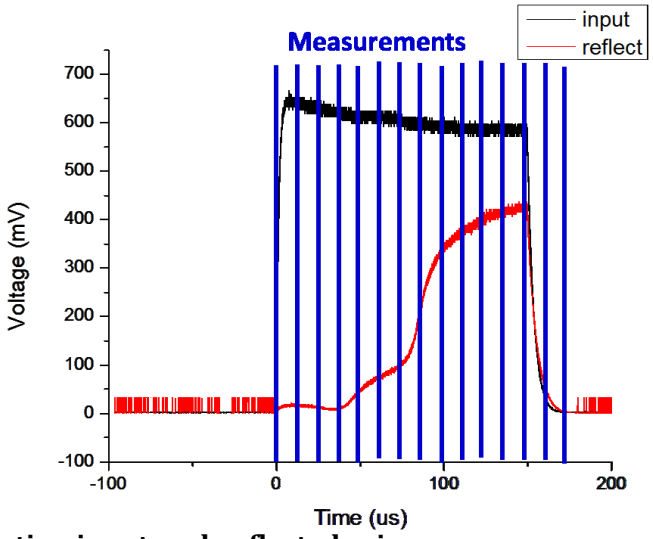


**Figure 4.12. Relative input and reflected microwave power, measured in a pulsed microwave discharge operated at a very low duty cycle of 0.6%. Nitrogen P = 40 Torr, flow rate 5 SLM, microwave pulse repetition rate 40 Hz, pulse duration 150 μs. Estimated peak input power is 100 W.**

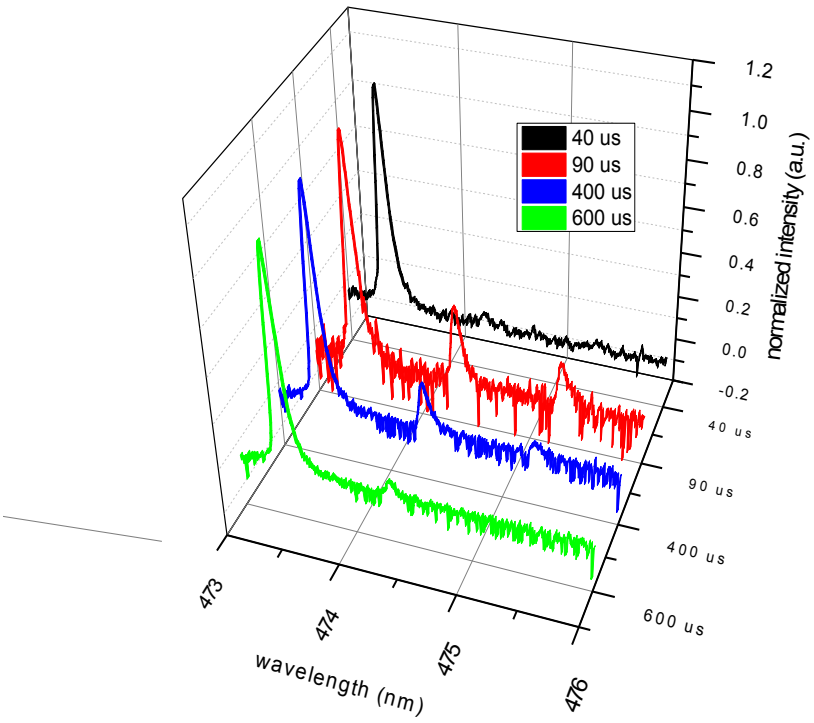


**Figure 4.13. Broadband CARS spectra taken at four different delay times during and after the discharge pulse, at the conditions of Figure 4.12. t=0 corresponds to the beginning of the pulse. $N_2$(v=0-2) vibrational bands are detected.**

Figure 4.13 shows several CARS spectra taken at four different delay times during and after the microwave discharge pulse at the conditions of Figure 4.9 (nitrogen P = 40 Torr, flow rate 5 SLM). Every spectrum is accumulated over 3000 laser shots, i.e. over 300 seconds. In Figure 4.13, it can be seen that $N_2$ vibrational levels up to v = 2 are detected during the discharge pulse, at t = 90 μs. In the afterglow, at t = 400 μs, the reduction of the normalized square-root intensities of v = 1 and v = 2 peaks (i.e. the reduction of the excited vibrational level populations) is apparent, compared to t = 90 μs. In late afterglow, at t = 600 μs, the v = 2 peak is no longer detected. Since the spectra in Figure 4.13 are taken using a lower resolution grating in the spectrometer, and without injection seeding in the Nd:YAG

laser, the spectral resolution is significantly lower, such that the rotational structure of the vibrational bands is only partially resolved. During these measurements, injection seeding was turned off to improve the signal-to-noise of the CARS spectra taken at a relatively low pressure.

Figure 4.14 compares the $N_2$ (v = 0) band CARS spectra at t = 90 μs with the best-fit synthetic spectra, indicating the rotational temperature of T = 468 ± 35 K. As mentioned above, with the Nd:YAG laser injection seeding turned off, the spectral resolution is relatively low, such that the quality of the fit at the tail of the $N_2$(v = 0) band is not very good. Thus, determining the uncertainty in the inferred rotational temperature becomes more challenging. By comparing the experimental CARS spectrum with the synthetic spectra for T = 350 and 500 K, as shown in Figure 4.14, it can be seen that in spite of the relatively low resolution in the experimental spectrum, the uncertainty in the rotational temperature appears to be within ±50 K. Figure 4.15 plots time-resolved $N_2$ "first level" vibrational temperature and rotational-translational temperature at the conditions of Figures 4.12 and 4.13, at the discharge pressure of 40 Torr and nitrogen flow rate of 5 SLM, with the microwave generator operating at the pulse repetition rate of 40 Hz and the estimated coupled power of 100 W. The results indicate that strong vibrational nonequilibrium is achieved in a pulsed microwave discharge in nitrogen operated at a very low duty cycle. It can be seen that the vibrational temperature measured in the beginning of the discharge pulse is approximately $T_V$ = 1000 K (near the detection limit of the present diagnostics) and increases up to $T_V$ = 2000 ± 180 K at 90 μs, due to $N_2$ vibrational excitation by electron impact. At t = 100 – 300 μs, the vibrational temperature remains about the same, $T_V \approx 2000$ K, before it starts decreasing at t = 400 μs. After t > 700 μs, $N_2$ (v = 1) vibrational band and

higher vibrational bands are no longer detected in the CARS spectra. During the first 70 μs, the resolution of the $N_2$(v = 0) vibrational band is too low for reliable rotational-translational temperature inference from the CARSFT spectra. At t = 70 – 400 μs, the gas temperature first gradually increases from T = 430 K to its maximum value of T = 530 K, and then decreases at t > 400 μs. Based on these results, at the present experimental conditions, vibrational nonequilibirum in the microwave discharge and the afterglow in nitrogen is sustained only for several hundred μs, after which the afterglow plasma rapidly approaches near thermal equilibrium. Sustaining vibrational nonequilibrium at quasi-steady-state would require significant reduction of flow residence time in the discharge, i.e. the increase of the flow rate.

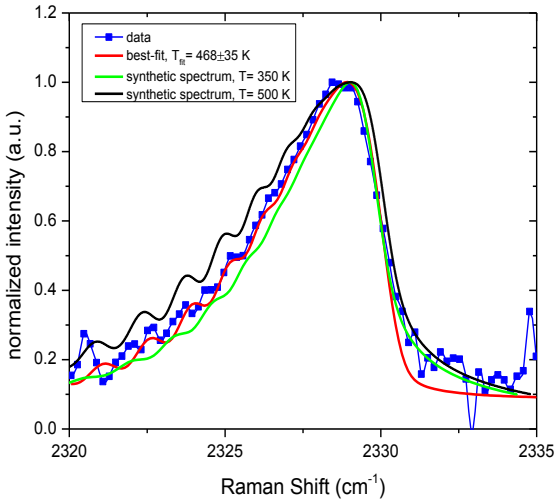


**Figure 4.14. Comparison of the experimental $N_2$ (v = 0) vibrational band CARS spectrum at t = 90 μs with the best-fit synthetic spectrum and with two additional synthetic spectra at different temperatures. The experimental conditions are the same as in Figure 4.12.**

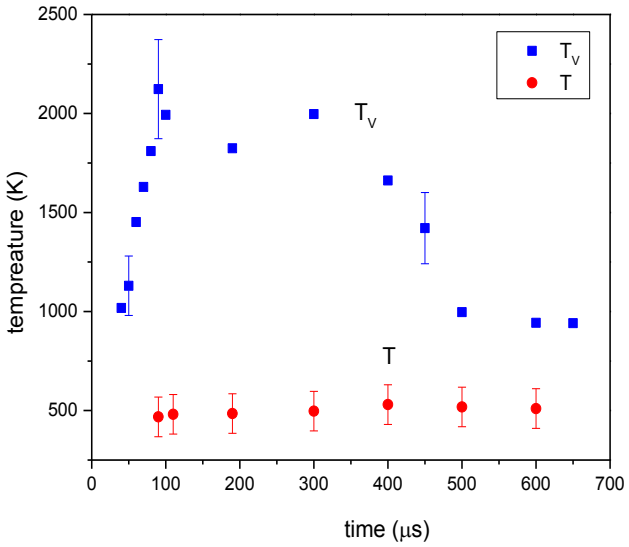


**Figure 4.15. Time-resolved $N_2$ vibrational temperature and rotational-translational temperature inferred from the CARS spectra taken during and after the microwave discharge pulse in 40 Torr $N_2$. The experimental conditions are the same as in Figure 4.12.**

### 4.5. CARS Measurements in a Microwave Discharge in $CO_2$

As discussed in Chapter 4.2, replacing the mixture of KR 620 and R640 dyes by a mixture of R590 and R610 dyes in the broadband dye laser provides access to the $CO_2$ symmetric stretch mode (100 → 000, Raman Shift = 1338 $cm^{-1}$). $CO_2$ CARS spectra are taken in a cw microwave discharge in pure $CO_2$. Figure 4.13 shows comparison of the experimental $CO_2$ spectrum taken in the discharge in 200 Torr of $CO_2$ at a flow rate of 15 SLM and the input power of 175 W with synthetic spectra generated by CARSFT $CO_2$ [62]. It can be seen that in addition to the fundamental transitions (100) → (000), a higher vibrational transition (hot band, (110) → (010)) is also detected in the experimental spectrum (see Figure 4.16). The symmetric stretch vibrational mode of $CO_2$ is expected to

be in equilibrium with the rotational and translational modes, due to its relatively low vibrational energy spacing, 1389 $cm^{-1}$. The best fit rotational-translational temperature inferred from these conditions is T = 738 ± 100 K. However, from Figure 4.16, which plots $CO_2$ synthetic spectra at T = 700 K, 900 K and 1200 K, it can be seen that $CO_2$ CARS spectra are not sensitive to the rotational-translational temperature below T < 900 K. This makes the use of $CO_2$ CARS spectra for temperature inference very challenging and subject to significant uncertainty. Since both the bending mode and the asymmetric stretch mode of $CO_2$ are not Raman active, they cannot be used to study vibrational energy transfer in $CO_2$ (specifically among $CO_2$ (001), $CO_2$ (010), $CO_2$ (020) and $CO_2$ (100) states) by CARS. Although the theory predicts that $(\upsilon_3 + 2\upsilon_1) \rightarrow (\upsilon_3 + \upsilon_1)$ can also be detected in $CO_2$ CARS spectra, at the conditions of Figure 4.16, only the symmetric stretch band transitions (100) → (000) and (110) → (010) have been detected in the experiment. In summary, $CO_2$ CARS does not appear to have significant potential for characterization of microwave discharge plasmas in $CO_2$.

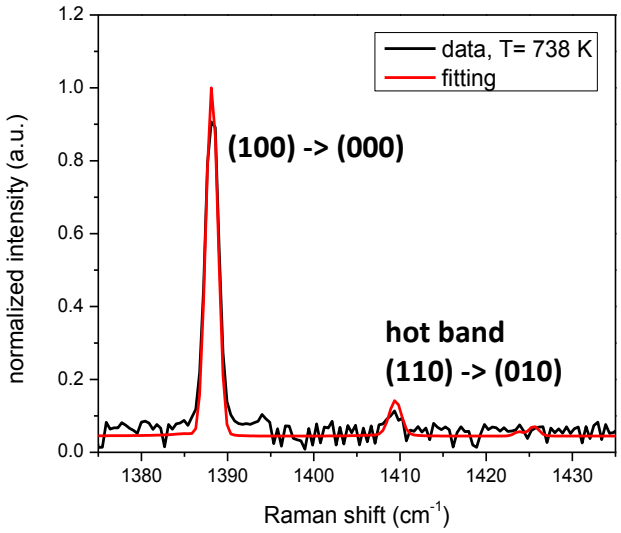


**Figure 4.16. Comparison of an experimental $CO_2$ CARS spectrum with the CARSFT synthetic spectrum. Cw microwave discharge in 200 Torr of $CO_2$, input microwave power 175 W, flow rate 15 SLM.**

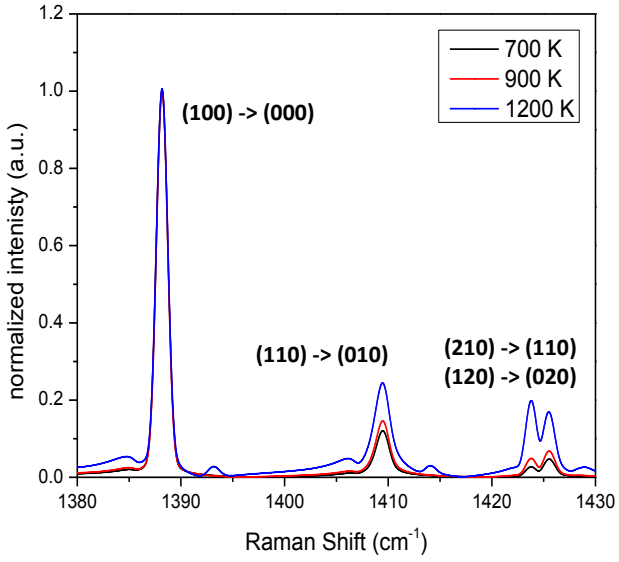


**Figure 4.17. Synthetic $CO_2$ CARS spectra generated by CARSFT at three different temperatures.**

# Chapter 5. Characterization of Atmospheric Pressure Hydrogen Diffusion Flames Enhanced by Ns Pulse Discharge and AC Discharge Plasmas

## 5.1. Introduction

As discussed in Chapter 1, in electric discharges sustained in fuel-air mixtures, the electric field waveform is well known to control the discharge energy partition among internal energy modes of molecules and atoms [1, 23], which is the dominant effect determining the rates of production of excited species and radicals by electron impact, as well as the rates of plasma chemical reactions. In this dissertation, broadband ns CARS is used for temperature measurements, and ps four-wave mixing, as well as ps second harmonic generation are used for electric field measurements in an atmospheric pressure hydrogen diffusion flame enhanced by dielectric barrier discharges (DBD) sustained by ns pulse and AC sine wave waveforms. The use of two different voltage waveforms makes possible isolating two different effects of the applied electric field on the flame, (i) radical species generation in a ns pulse DBD plasma, and (ii) ion wind generated in AC DBD plasma. It is well known that the ion wind effect on the flame in a ns pulse discharge is minimal, since it requires significant impulse of the Coulomb force, typical for AC and DC fields. On the other hand, ns duration voltage pulses can produce significantly higher peak electric fields during breakdown, compared to DC or AC voltage waveforms. The objective of this work is to provide insight into ns pulse breakdown kinetics in reacting hydrogen-air mixtures, which controls discharge energy coupling and energy partition, and to quantify charge transport processes generating the ion wind in the flame.

## 5.2. Temperature and Four-Wave Mixing Electric Field Measurements in a Ns Pulse Discharge in a Hydrogen Diffusion Flame

### 5.2.1. Burner and Discharge Electrode Assembly

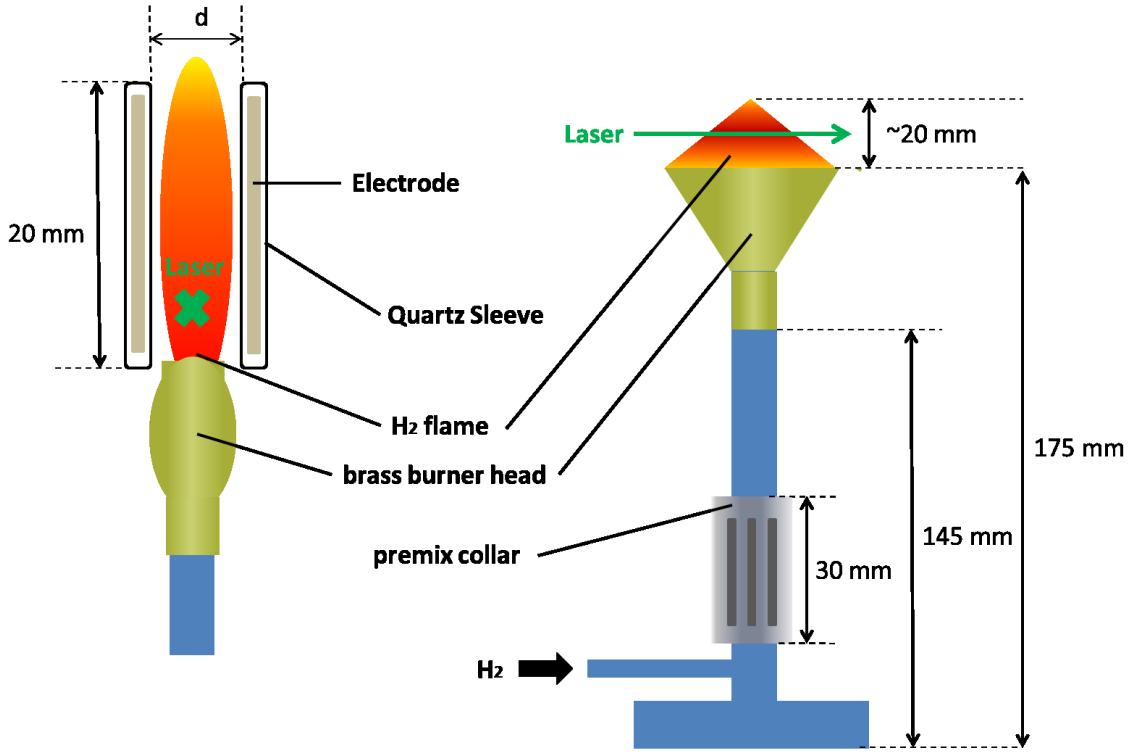


**Figure 5.1. Schematic of the burner and the discharge electrode assembly, front view (left) and side view (right). Distance between the electrode sleeves is varied between 1 mm and 6 mm.**

Figure 5.1 shows the schematic of the burner and the discharge electrode assembly. The height of the Bunsen burner used in the present work is approximately 175 mm. The burner is equipped with a brass flame spreader 50 mm long and approximately 1 mm wide, which produces a narrow elongated diffusion flame with the height above the flame spreader of approximately 20 mm at the hydrogen flow rate of 2 SLM. The burner is connected to the hydrogen supply line via a barbed connector in the base of the burner and a rubber tube. Hydrogen is supplied from a high-pressure gas cylinder. A flashback arrestor is connected between the hydrogen cylinder and the burner, to avoid flame propagation into the cylinder. To produce a diffusion flame or a partially premixed flame, air intake slots in the premixing collar can be closed or open, as shown in Figure 5.1. In the CARS measurements, the air intake slots are set to be fully closed to improve the flame stability. The burner is ignited by a safety laboratory lighter. Two parallel plate stainless steel electrodes L = 55 mm long, W = 18 mm wide, and t = 1.5 mm thick placed inside two quartz sleeves were positioned above the burner, as shown in Figure 5.2. Each quartz sleeve has an inside cross section of 17 mm $\times$ 20 mm and is about 120 mm long. The thickness of the sleeve walls (dielectric constant $\epsilon$ = 3.8) is $\Delta$ = 1.3 mm. The clearance between the electrodes and the channels in the sleeves is approximately $\delta$ = 0.1 mm. The electrode overlap length inside the quartz sleeves is approximately 50 mm. For ps four-wave mixing electric field measurements in a ns pulse discharge and CARS temperature measurement in the flame, the gap between the electrode sleeves is set to d = 1.3 – 1.7 mm and d = 6 mm, respectively. Figure 5.3 shows photographs of the burner and the electrode assembly, taken at the hydrogen flow rate of 2 SLM.

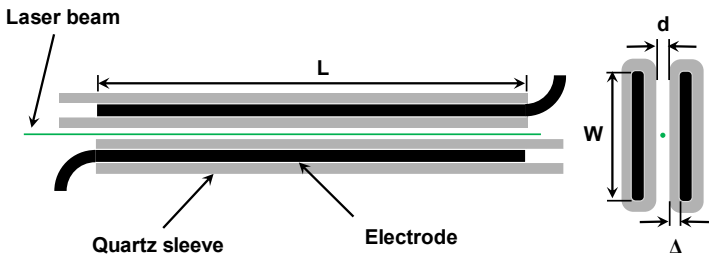


**Figure 5.2. Schematic of the discharge electrode assembly and the laser beam (not to scale) L = 100 mm, W = 18 mm, d = 1 – 10 mm, and Δ = 1.3 mm.**

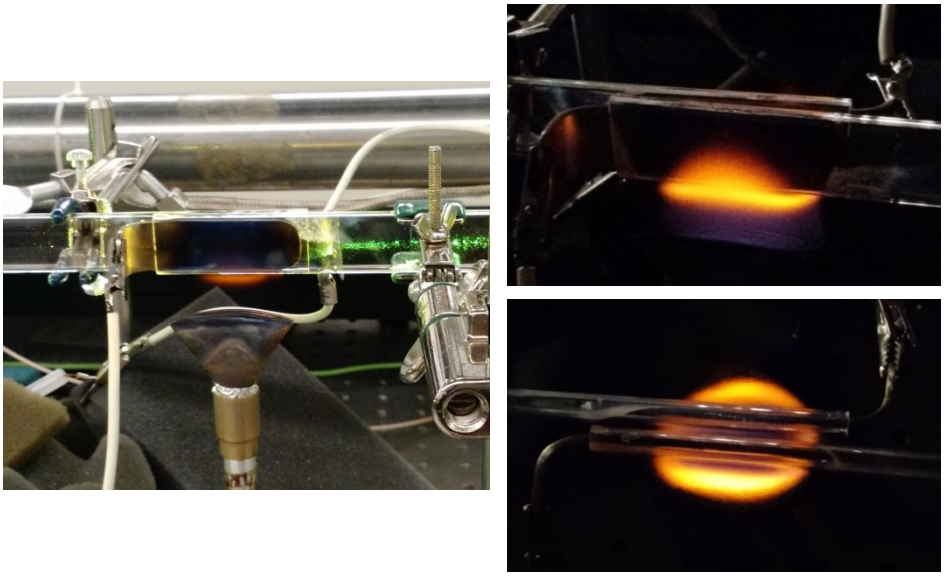

**Figure 5.3. (a) Photographs of the burner with two parallel plate electrodes inside quartz sleeves, placed 20 mm above the burner exit; (b) side view and top view photographs of the hydrogen flame, for the gap between the quartz sleeves of 5 mm. Hydrogen flow rate is 2 SLM.**

The electrodes are powered by a Mega Impulse pulse generator producing pulses with peak voltage of up to 26 kV and pulse duration of 5-10 ns FWHM, operated at the pulse repetition rate of 10 Hz and triggered externally by a delay generator. This generates a double dielectric barrier discharge in air or in a hydrogen diffusion flame between the electrodes. The effective electrode gap is $d^* = d + 2\delta + 2\Delta/\varepsilon$ = 2.2-2.6 mm, with the uncertainty of ± 0.2 mm. The discharge pulse voltage and current are measured by Tektronix P-6015 high voltage probe and Pearson 2877 current probe. Comparison of pulse voltage waveforms measured by the Tektronix probe and by a custom-made, high bandwidth voltage probe shows that peak voltage and pulse width measured by both probes agree within several percent. Plasma emission images are taken by a Princeton Instruments PI-Max 3 ICCD camera.

### 5.2.2. CARS Optical Setup

Temperature in the flame is measured by broadband ns CARS, the same as discussed in Chapter 3.3. Briefly, 90% of the second harmonic output of an injection seeded Nd:YAG laser (Surelite SLIII-10, pulse energy up to 400 mJ, linewidth 0.015 $cm^{-1}$) is used to pump a custom-built broadband dye laser generating the Stokes beam ≈3 nm wide, centered at 605 nm. The rest of the Nd:YAG laser output is used as the pump/probe beam. The pulse energies of the pump/probe and the Stokes beams are 7.0 mJ and 3.2 mJ, respectively. The two beams are combined using a delay line and dichroic mirrors, and focused by a 20 cm focal distance lens, in collinear phase matching geometry. The length of the probe volume, defined as the region where 95% of the CARS signal is generated and measured by

translating a microscope slide along the focused beams, is approximately 4 mm. The CARS signal is separated from the pump and the Stokes beams using dichroic mirrors, and detected by an Andor Shamrock 750 spectrometer with Andor EMCCD camera. The rotational-translational temperature is inferred by fitting the experimental square root intensity of $N_2$ (v=0) band spectra with the synthetic CARSFT spectra [46].

### 5.2.3. Four-Wave Mixing Diagnostics

Figure 5.4 shows a schematic of the four-wave mixing experimental apparatus [37]. A picosecond Nd:YAG laser (Ekspla SL333) producing output pulses ~150 ps long with energy of 60 mJ/pulse at 532 nm, pumps a high-pressure Raman cell to generate a collinear Stokes beam at 607 nm.

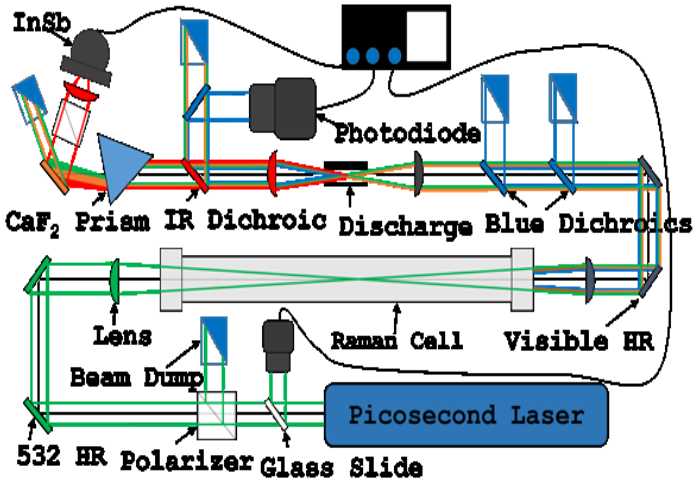


**Figure 5.4. Schematic of ps four-wave mixing diagnostics [38].**

The same delay generator that triggers the high-voltage pulser is also used to trigger the flash lamps of the laser. A second delay generator triggers the Q-switch of the laser and controls the delay time between the discharge pulse and the laser pulse, varied from t = -10 ns (10 ns before breakdown between the electrodes) to t=20 ns. The Raman cell is a stainless steel tube 3 m long and 5 cm in diameter, filled with a 50%-50% mixture of nitrogen and helium at a pressure of 15 bar. Helium is added to help dissipate heating caused by laser beam absorption in the cell and improve the output beam quality. The pump and Stokes beams linewidth, 0.1 $cm^{-1}$ and 0.4 $cm^{-1}$, respectively, are measured by a High Finesse Angstrom WS/6 wavemeter. Higher order Stokes and anti-Stokes output, also generated in the Raman cell, is filtered out by dichroic mirrors transmitting the 607 nm first order Stokes beam and the 532 nm pump beam.

The collinear pump and Stokes beams are re-collimated and focused in the region between the electrodes by a 50 cm focal distance lens, as shown in Figure 5.4. After the test region, the pump and Stokes beams are re-collimated again, and the four-wave mixing signal beam (at 4.3 μm) is separated from the pump, Stokes, and anti-Stokes ($N_2$ vibrational CARS) beams using a dichroic mirror which transmits in the infrared while reflecting in the visible. The CARS beam is separated from the pump and Stokes beams using dichroic mirrors such as placed after the Raman cell, and its intensity is measured by a photodiode. The IR four-wave mixing signal beam is separated from residual visible beams using a $CaF_2$ equilateral dispersion prism, and its intensity is measured by a liquid nitrogen cooled InSb detector with a matching preamplifier.

The four-wave mixing beam intensity is proportional to the squared electric field integrated along the length of the discharge electrodes. Previous measurements [36] show that at the present conditions, the four-wave mixing signal generated along the electrodes is distributed nearly uniformly, due to a large signal coherence length, 14 cm at room temperature and 40 cm at T = 1300 K. IR, $N_2$ CARS, and pump laser signals, as well as voltage and current waveforms, are monitored by a LeCroyWaverunner MXi-A digital oscilloscope with a 1 GHz sampling rate. The waveforms are averaged over 300 laser shots.

The electric field is determined from time-integrated IR, pump, and CARS signal intensities, $|E| = \alpha\sqrt{I_{IR}I_{pump}/I_{CARS}}$, where α is the calibration constant [39]. For absolute calibration, the signal is scaled to match the voltage waveform at t<0 (before breakdown), when the electric field in the gap remains Laplacian, E = U/d*, where d* is the effective electrode gap. The knowledge of the combustion product mixture composition (specifically the number density of the probe species, $N_2$) is not needed for the inference of the electric field. The uncertainty of the electric field is determined by the uncertainty of the gap, ±10%. The detection limit at room temperature is approximately 3-4 kV/cm.

### 5.2.4. Temperature Measurements in a Hydrogen Diffusion Flame

Figure 5.5 (a) shows a typical $N_2$ broadband CARS spectrum measured in the 2 SLM $H_2$ diffusion flame 5 mm above the flame spreader exit, without the electrode sleeves in place. The temperature inferred from the best-fit CARSFT synthetic spectrum is T = 1300 ± 150 K. Comparison of $N_2$ CARS spectra taken with and without the electrode sleeves in place is shown in Figure 5.5 (b), indicating that adding the electrodes has a significant effect on the spectrum, such that it can no longer be represented by a single-temperature synthetic spectrum generated by CARSFT. This effect becomes more pronounced when the gap between electrode sleeves is reduced from 10 mm to 4 mm. For gaps smaller than 4 mm, the CARS pump/probe beam and the Stokes beam cannot pass between electrode sleeves without clipping, such that no CARS spectra are taken for gaps smaller than 4 mm. Since the CARS measurement region is approximately 3.5 mm long (see Figure 3.17), much shorter compared to the length of the flame (about 50 mm), inability of CARSFT to fit the experimental CARS spectra with the electrode sleeves in place is most likely due to incomplete mixing of ambient air with high-temperature combustion products in the narrow slots between the sleeves.

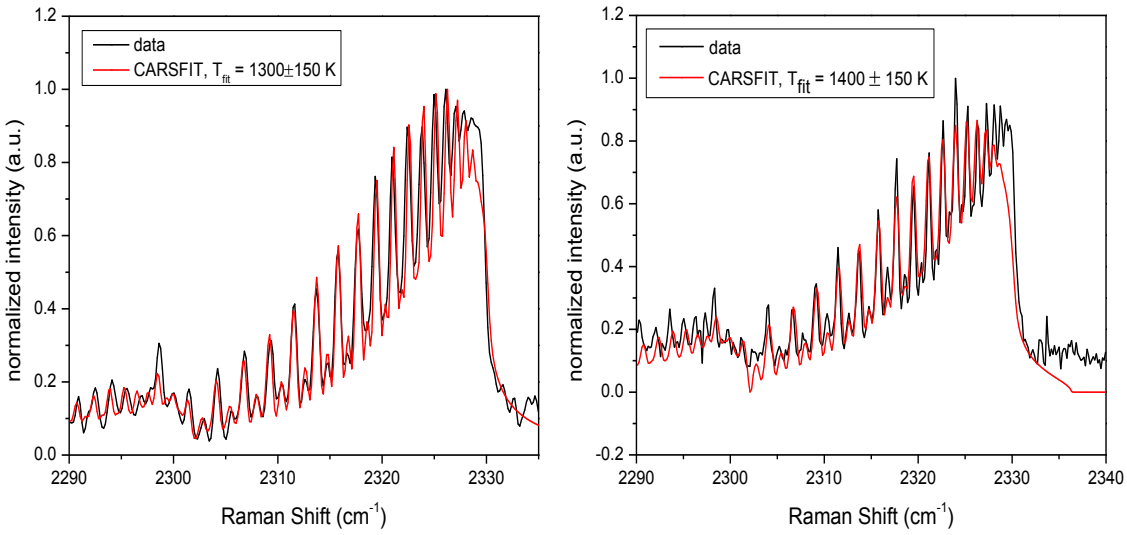


**Figure 5.5. (a) Typical broadband $N_2$ CARS spectrum in the flame measured 5 mm above the flame spreader exit, plotted together with the best fit CARSFT synthetic spectrum. (b) Broadband $N_2$ CARS spectra taken with electrode sleeves placed 6 mm apart. In both spectra, $H_2$ flow rate is 2 SLM.**

Figure 5.6 plots a typical $N_2$ broadband CARS spectrum taken in the flame at the $H_2$ flow rate of 1 SLM, 5 mm above the flame spreader exit, with the electrode sleeves in place. At these conditions, the gap between the electrode sleeves is 4 mm. It can be seen that the temperature inferred from the best fit CARSFT synthetic spectrum, T = 1150 ± 200 K, is lower than at the $H_2$ flow rate of 2 SLM, T = 1400 K, and the fitting quality is somewhat worse compared to the spectrum taken in the 2 SLM flame with the electrode sleeves in place (see Figure 5.5 (b)), indicating higher temperature non-uniformity in the gap in the 1 SLM flame. Table 5.1 summarizes temperatures inferred from the CARSFT best-fit synthetic spectra at different experimental conditions.

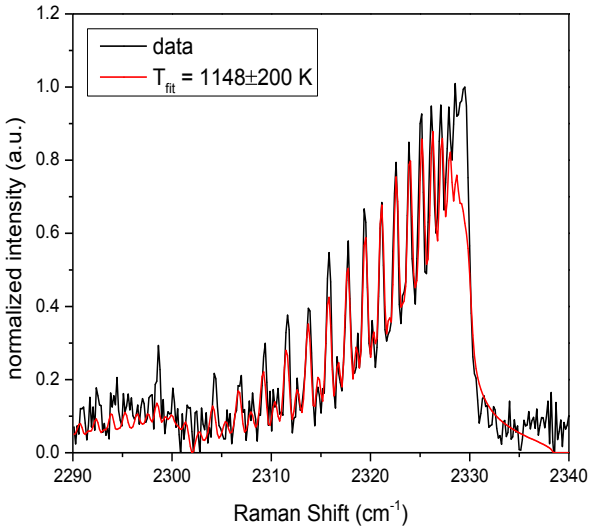


**Figure 5.6. Typical CARS spectrum taken in the flame at the $H_2$ flow rate of 1 SLM, 5 mm above the flame spreader exit, with the electrode sleeves in place. The gap between the sleeves is 4 mm.**

| Measurement Conditions | $T_{fit}$ (K) |
|---|---|
| 1SLM, no electrode sleeves | 1090±150 |
| 2SLM, no electrode sleeves | 1300±150 |
| 1SLM, electrode gap 4 mm | 1150±200 |
| 2SLM, electrode gap 4 mm | estimated to be 1400±150 |
| 1SLM, electrode gap 8 mm | 1300±200 |
| 2SLM, electrode gap 8 mm | 1500±250 |

**Table 5.1. Temperatures inferred from the best fit CARSFT spectra at different experimental conditions, without and with electrode sleeves in place.**

These results show that the electric field measurements, discussed in Section 5.2.5, are taken in the flow of high-temperature combustion products. Reducing the gap between the electrodes obstructs mixing between the combustion products and the ambient air, such that CARS spectra taken at these conditions cannot be represented by a single rotational-translational temperature.

### 5.2.5. Ns Pulse Discharge Plasma Emission Images and Electric Field in a Ns Pulse Discharge in a Hydrogen Diffusion Flame

Single-shot ICCD images of the plasma generated by the discharge pulse in the hydrogen diffusion flame are shown in Figure 5.7(a). These images are taken using a 20 ns camera gate, comprising the entire voltage pulse with peak voltage of 13 kV and FWHM of 10 ns. The plasma appears diffuse, without well-pronounced filaments, with good pulse-to-pulse reproducibility of the images. To illustrate the evolution of plasma emission intensity during the discharge pulse, Figure 5.7(b) shows a sequence of 100-pulse average images taken with a camera gate of 1 ns. The emission decays approximately over 6 ns after breakdown, except for two regions near the ends of the electrodes. Plasma emission images taken in room air for the same discharge gap, with pulse peak voltage of 18 kV and FWHM of 10 ns, exhibit similar behavior.

Time-resolved electric field in the discharge in air and in the hydrogen flame, for the gap between the electrode sleeves of d = 1.3 mm, calibrated by the electrostatic voltage before breakdown, $E = U/d^*$, is plotted in Figure 5.8(a). Breakdown occurs when the field in the discharge gap begins to deviate from the applied voltage waveform, also plotted in

Figure 5.8(a). It can be seen that breakdown field in air, $E_{peak}$ = 75 ± 7.5 kV/cm, is much higher compared to DC breakdown threshold estimated from Paschen law, ≈ 30 kV/cm, due to the rapid voltage increase rate, ≈ 4 kV/ns. At these conditions, the uncertainty in the electric field is controlled mainly by the uncertainty in the measurements of the electrode gap. After breakdown, charge separation and plasma self-shielding result in rapid electric field reduction, to 10-15 kV/cm over 3 ns, while plasma emission decays. The electric field remains below breakdown threshold during the rest of the applied voltage pulse. Although time resolution of the present measurements is approximately 2 ns, these results are consistent with the higher temporal resolution measurements in air, 0.2 ns, at similar conditions [37].

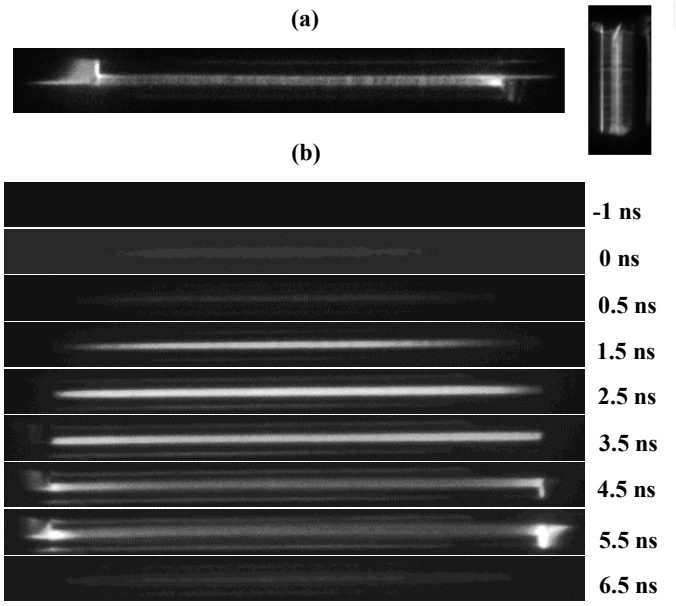


**Figure 5.7. Broadband plasma emission images in the flame: (a) single-pulse, 20 ns camera gate (top view and end view); (b) 100-pulse average, 1 ns gate. Discharge gap d = 1.3 mm.**

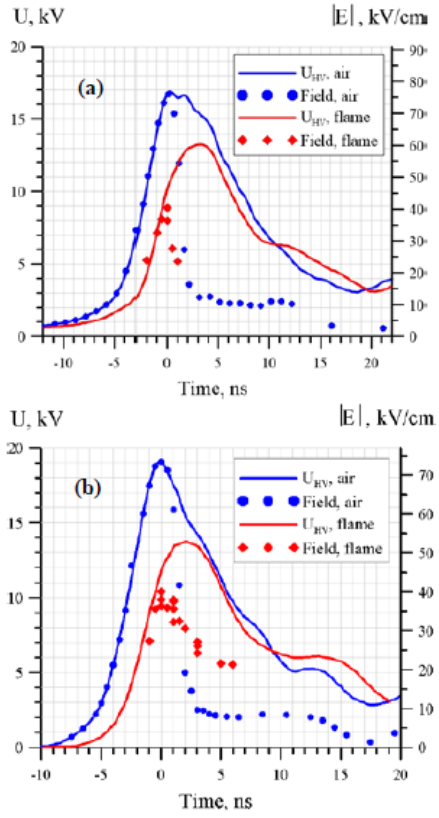


**Figure 5.8. Pulse voltage waveforms and electric field in the ns pulse discharge in room air and in $H_2$ diffusion flame for the discharge gap of (a) 1.3mm and (b) 1.7 mm.**

In the flame, breakdown occurs well before the applied voltage peaks (see Figure 5.8 (a)). Again, the field in the discharge gap begins to deviate from the applied voltage waveform at the breakdown moment. Similar to the discharge in air, in the hydrogen flame the electric field after breakdown in reduced rapidly, over several ns, while the plasma emission decays (see Figure 5.8). Accurate time-resolved field measurements significantly before and well after breakdown are challenging due to low signal-to-noise, with measurement uncertainty at 20 kV/cm increasing to approximately ±35%. Breakdown field in the flame, $E_{peak}$ = 40±4 kV/cm, is considerably lower compared to that in air, for the same

discharge gap. Figure 5.8 (b), plotting electric field data and voltage waveforms in the discharge in air and in the flame for a larger gap between the electrode sleeves, d = 1.7 mm, exhibits very similar results to Figure 5.8 (a), including breakdown field values and electric field behavior before and after breakdown.

Comparing the results of electric field measurements in air and in the hydrogen flame, it is clear that peak electric field in the flame is significantly lower, approximately 40 kV/cm vs. 75 kV/cm. Although it is somewhat difficult to compare these values directly, since the pulse voltage waveforms and the gas mixture compositions for these two cases are different, the breakdown field reduction is almost certainly due to the higher temperature (i.e. lower number density, N) in the flame, which results in a higher reduced electric field, E/N, during the pulse.

Although the sensitivity of the present ps four-wave mixing diagnostics in room air is 3 - 4 kV/cm, its use for measurements of electric fields below ~ 20 kV/cm in atmospheric pressure flames is challenging, due to low signal-to-noise. The present diagnostics will have much better sensitivity in high-pressure flames, since the four-wave mixing signal scales as squared number density of nitrogen. The detection limit in flames maintained at pressures above ~ 3 bar is estimated to improve to below ~ 2 kV/cm, far below breakdown threshold. The present method determines the electric field averaged over the four-wave mixing coherence length (several cm at the present conditions). The use of a shorter focal distance lens would result in significantly higher spatial resolution, controlled by the Rayleigh range of the lens.

## 5.3. Temperature and Electric Field Measurements in Ns Pulse and AC Discharges in a Hydrogen Diffusion Flame

In Section 5.3 ps four-wave mixing was used for measurements of electric field in ns pulse discharges in ambient air and in a hydrogen diffusion flame, using molecular nitrogen as a probe species. The results have shown that the sensitivity of this diagnostics in the flame is significantly worse compared to that in room-temperature air, ~ 20 kV/cm vs. 3-4 kV/cm. This occurs primarily due to higher temperature and lower $N_2$ fraction in the combustion product mixture, since the signal is proportional to the number density of the probe species squared. This difficulty limits the use of four-wave mixing to electric field measurements in high-pressure flames (several atm), where plasma generation becomes more challenging. However, comparison of ps FWM and ps SHG measurements of the electrostatic electric field in ambient air shows that the latter method is considerably more sensitive, generating a much higher signal at a significantly lower laser power, suggesting that it would be more effective for diagnostics of atmospheric pressure flames. Also, electric field induced second harmonic signal is generated in the visible part of the spectrum, instead of the IR signal in four-wave mixing (4.3 μm if molecular nitrogen is used as a probe species), such that it can be measured by PMT detectors and CCD cameras. In this section, ps SHG is used to measure the electric field in hydrogen diffusion flames enhanced by ns pulse and AC sine wave dielectric barrier discharges. The temperature in the plasma, necessary for estimating the reduced electric filed, is measured by ns broadband CARS.

### 5.3.1. Hydrogen Burner and Discharge Electrode Assembly

Figure 5.9 shows the schematic of the burner, the electrode assembly, and the location of the laser beam. Although this experiment is conceptually similar to the one discussed in Section 5.2, both the burner and the electrodes have been modifed. The burner used in this experiment is a Bunsen burner, in which the barrel with air intake slots has been removed and replaced by a custom-made flame spreader made of quartz, with the rectangular exit slot dimensions of 0.5 × 45 mm. The quartz wall thickness of the flame spreader exit is 1.25 mm. Hydrogen flows through the burner at the flow rate of 1 – 2 SLM. maintaining an elongated diffusion flame ≈ 50 mm long above the flame spreader. The height of the burner is approximately 65 mm. Hydrogen at the flow rate of 1- 2 SLM is supplied to the burner from a high-pressure cylinder, via a ¼" diameter stainless steel line, flash arrester, and a flexible tubing connected to a barbed connector at the base of the burner, in the same way as discussed in Section 5.2. The geometry of the flame spreader provides ample access for the discharge electrodes applying external electric field across the flame, in a simple rectangular geometry. The electrodes used in this experiment are two brass rods placed inside alumina ceramic tubes, providing the dielectric barrier. Unlike in the experiment discussed in Section 5.2, alumina ceramic dielectric was used instead of quartz, since filamentation of the AC discharge resulted in damaging the quartz dielectric sleeves. The diameter of the electrode rods is D = 3.2 mm, the alumina ceramic tube wall thickness is Δ = 1.6 mm, the overlapping electrode length is L = 50 mm, and the gap between the electrodes is varied from d = 4 mm to 15 mm. During ns CARS temperature measurements and ps second harmonic generation electric field measurements, the electrodes were placed 2 mm above the flame spreader exit, as show in Figure 5.9 and 5.10.

For larger electrode gaps, d = 12 – 15 mm, the flame is attached to the flame spreader, while for smaller gaps, d = 4 – 5 mm, it is attached to the top of electrode sleeves, as shown schematically in Figure 5.9. The electrodes are powered by a custom-made high-voltage pulse generator producing alternating polarity pulses with peak voltage of up to $U_{peak}$ = 16 kV and pulse repetition rate of 20 Hz, or by a Trek Model 20/20A high-voltage AC amplifier driven by a sine wave function generator, with peak voltages of up to $U_{peak}$ = 14 kV and frequencies of f = 1-10 kHz. The discharge voltage and current waveforms are measured by Tektronix P-6015 high voltage probe (bandwidth 75 MHz) and Pearson 2877 current probe (bandwidth 200 MHz). Plasma emission images are taken by Princeton Instruments PI-Max 3 ICCD camera with a UV lens.

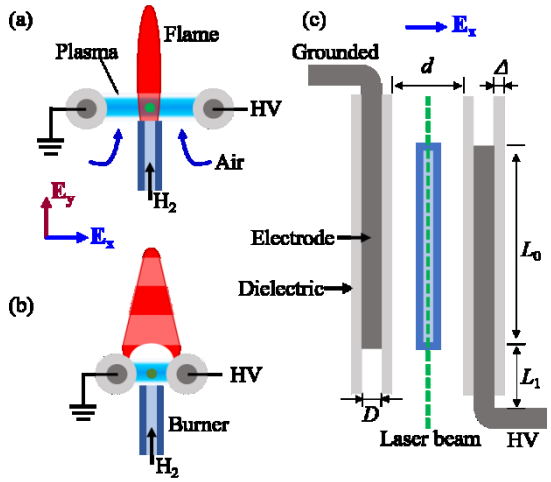


**Figure 5.9. Schematic of the burner, double dielectric barrier discharge electrode assembly, and the laser beam. Diameter of brass electrode rods is D = 3.2 mm, electrode overlap $L_0$ = 45 mm, non-overlapping electrode length $L_1$= 5 - 20 mm, alumina ceramic tube thickness Δ = 1.6 mm, electrode gap d = 12 - 15 mm (a) or d=4-5 mm (b).**

**Figure 5.10. Photographs of the burner and the electrode assembly. The distance between the ceramic tubes is d = 15 mm.**

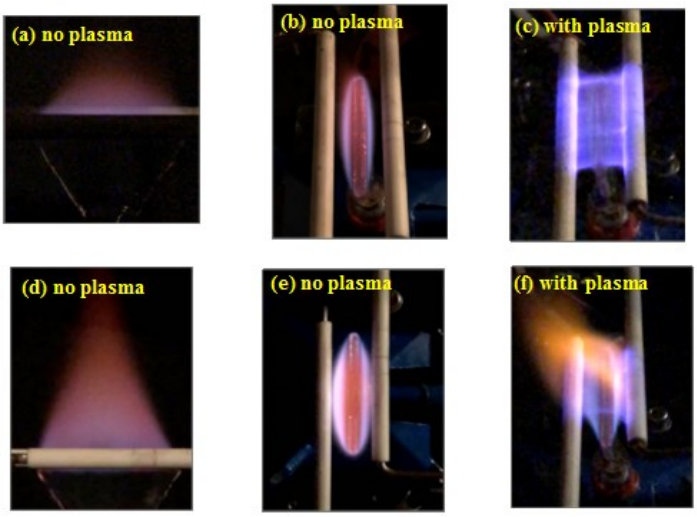


**Figure 5.11. Photographs of a hydrogen diffusion flame, with and without 3 kHz AC voltage applied: (a-c) hydrogen flow rate 1 SLM; (d-f) hydrogen flow rate 2 SLM. Electrode sleeves are placed 2 mm above the flame spreader exit, electrode gap *d*=15 mm. Peak voltage peak voltage 14 kV (c) and 11 kV (f).**

Figure 5.11 shows photographs of the flame at two different $H_2$ flow rates, 1 SLM and 2 SLM, with and without AC voltage applied to the electrodes. It can be seen that applying the AC voltage, when the dielectric barrier discharge (DBD) plasma is generated in the 15 mm gap between the electrode sleeves, strongly distorts the flame, which always extends toward the grounded electrode, due to the ion wind. Since the effect of the ion wind on the flame becomes weaker as the $H_2$ flow rate is increased, the flame is fully overlapped with the plasma at 1 SLM (see Figure 5.11(c)), such that it is difficult to detect in the photograph, and extends beyond the plasma at 2 SLM (see Figure 5.11(f)). For the electrode gap of d = 12-15 mm, the flame is attached to the flame spreader exit (see Figure 5.12(a)). When the electrode gap is reduced to d = 4-5 mm, the flame becomes attached to the top of the electrode sleeves (Figure 5.12(b)). In the latter case, the spacing between the electrode sleeves and the flame spreader becomes so small that the air flow between them is inhibited, such that the flow between the electrodes is mostly hydrogen (with an admixture of air), and mixing between hydrogen and air as well as combustion occurs above the electrode sleeves. When the AC DBD plasma is generated in the 4-5 mm electrode gap, such that it is confined to the region between the electrode sleeves below the flame, the ion wind effect on the flame also becomes much weaker compared to that observed for the 12 - 15 mm gap.

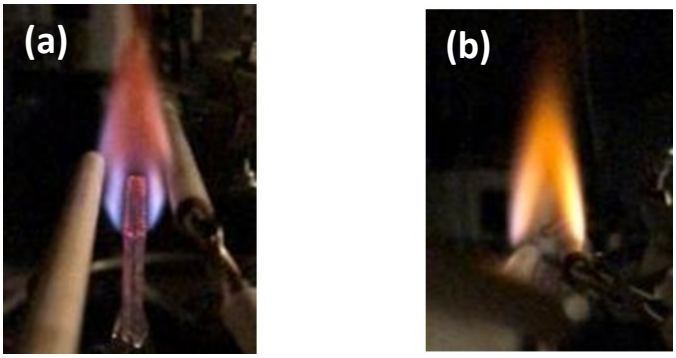


**Figure 5.12. Photographs of a hydrogen diffusion flame for different gaps between the electrodes: (a) d = 12 mm, flame is attached to the flame spreader exit; (b) d = 4.5 mm, flame is attached to the top of the electrode sleeves. In both cases, electrode sleeves are placed 2 mm above the flame spreader exit. Hydrogen flow rate 1 SLM, no plasma.**

When a ns pulse discharge is generated between the electrodes, the ion wind effect on the flame is not detectable in the entire range of electrode gaps tested, d = 4 - 15 mm, due to extremely low Coulomb force impulse and low discharge pulse repetition rate, 20 Hz. Since the main focus of the present work is on measurements of the electric field and temperature in plasma-enhanced flames, rather than on kinetics of plasma-assisted hydrogen combustion, the ns pulse discharge was operated at 20 Hz, such that the repetition rate of positive and negative polarity discharge pulses (10 Hz each) would match the laser pulse repetition rate.

### 5.3.2. Second Harmonic Generation Diagnostics

Figure 5.13 shows a schematic of ps SHG laser diagnostics. Briefly, the fundamental (1064 nm), vertically polarized output beam of an Ekspla PL2143A Nd:YAG laser, with a pulse duration of 30 ps and maximum pulse energy of 50 mJ, operating at 10 Hz, is focused into a region where the electric field is applied, using a 100 cm focal distance lens. The laser beam diameter at the focal point, measured by traversing a razor blade across the beam, is approximately 200 μm, with the Rayleigh range of about $z_R \approx 30$ mm. The focal point of the beam is placed at the center of the discharge electrode assembly (see Figure 5.9). The laser is operated at the pulse energy of 10 mJ/pulse. The main advantage of the use of the fundamental laser output, instead of the second harmonic, is nearly total absence of hydrogen flame emission and plasma emission at the second harmonic wavelength (532 nm) generated in the presence of the external electric field. The second harmonic signal beam is separated from the fundamental beam using a pair of dichroic mirrors and a dispersion prism, as shown in Figure 5.13. The signal beam is re-collimated and then focused onto the entrance slit of a monochromator, followed by a narrowband pass filter (50% transmission at 532 nm, 10 nm band pass) to remove the remaining 1064 nm signal, plasma emission, and stray light (see Figure 5.13), and detected by a photomultiplier tube (PMT). To further reduce the noise due to stray light, the monochromator, the pass filter, and the PMT are placed inside a dark enclosure with a $\sim$ 2 cm diameter entrance aperture. Using a polarizer mounted on a rotation stage before the focusing lens, as shown in Figure 5.13, allows isolating vertically and horizontally polarized second harmonic signals, by rotating the polarizer over 90 degrees. The timing and the pulse energy of the fundamental laser beam are monitored by a photodiode.

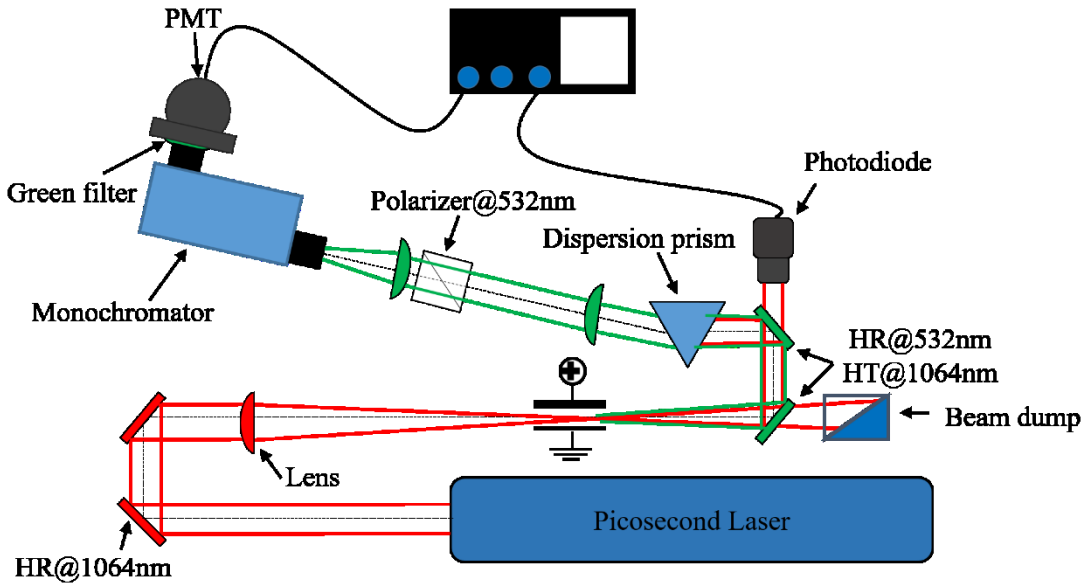


**Figure 5.13. Schematic of picosecond second harmonic generation diagnostics.**

The theory of second harmonic generation in the presence of an external electric field is discussed in detail in [38, 39]. Briefly, the intensity of the electric-field-enabled second-harmonic signal (at the frequency 2ω) is given as follows,

$$I_i^{(2\omega)} \sim [N\chi_{ijkl}^{(3)}(2\omega, 0, \omega, \omega)E_j^{ext}E_k^{(\omega)}E_l^{(\omega)}]^2 L^2 \left[\frac{\sin(\Delta k \cdot L/2)}{\Delta k \cdot L/2}\right]^2 \qquad \text{(Equation 5.1)}$$

In Equation 5.1, N is the total number density, $E_j^{ext}$ is the external "zero frequency" electric field, $E_k^{(\omega)}$ and $E_l^{(\omega)}$ are the electric field vector components in the incident laser beam (at the frequency ω), $\chi_{ijkl}^{(3)}$ is the third-order nonlinear susceptibility in the series expansion of the induced polarization vector, *i,j,k,l* are the indices indicating *x* or *y* components of the electric field vectors in the second harmonic signal beam, external electric field, and incident laser beam, respectively (see Figure 5.11), and *L* is the interaction length. Two non-

zero components of the susceptibility, $\chi^{(3)}_{yyyy}$ and $\chi^{(3)}_{xxyy}$, generate vertically and horizontally polarized second harmonic signals for $E_y^{ext}$ and $E_x^{ext}$, respectively, for a vertically polarized laser beam. Basically, the signal is proportional to the external electric field squared and laser beam intensity squared. The last factor in Equation 5.1 is the phase-matching factor controlling coherent growth of the second harmonic signal due to constructive interference, where

$$\Delta k = k(\omega) - k(2\omega) = \frac{2\omega \cdot n(2\omega) - \omega \cdot n(\omega)}{c} \qquad \text{(Equation 5.2)}$$

and $n$ is the refraction index of air. At the present conditions, the signal coherence length is relatively long, $L_c = \pi/\Delta k \approx 17$ cm, such that the region where the second harmonic signal is generated (i.e. the spatial resolution in the direction of the laser beam) is limited by the confocal parameter of the lens, $b = 2z_R \approx 60$ mm. Measurements of the spatial distribution of the second harmonic signal, by translating a pair of electrodes with sub-breakdown DC voltage applied to them along the laser beam, showed that the signal varies by only about 10% over a 4 cm distance. Therefore the present diagnostics measures root mean square values of the electric field vector components, $\langle E_i^{ext}(x,y,t)^2 \rangle_z^{1/2}$, averaged nearly uniformly over the span of the electrodes in the $z$-direction. The spatial resolution in $x$ and $y$ directions is of the order of the laser beam diameter, approximately 200 μm.

Absolute calibration of the measurements is obtained from the known electrostatic electric field generated halfway between the electrodes during the ns pulse voltage rise, before breakdown, or from a separate measurement of the electrostatic field produced by a lower peak voltage AC waveform, at the conditions when the plasma was not generated. The electrostatic (Laplacian) electric field distribution is calculated by solving the Laplace

equation for the electric potential, for the given electrode and burner geometry (two parallel cylinder electrodes in alumina ceramic sleeves, with the quartz flame spreader placed below the electrode plane, see Figure 5.9). During the calibration and measurements in the discharge, the PMT voltage is kept sufficiently low to avoid its saturation at high electric fields.

### 5.3.3. Temperature Measurements in $H_2$ Diffusion Flame, with and without the Plasma

Figure 5.14 plots CARS spectra in the hydrogen flame taken (a) in the circular diffusion flame in the burner with the barrel still attached and air intake slots closed, and (b) in the elongated flame when the barrel was replaced with the flame spreader, as shown in Figures 5.9 and 5.10, at the same $H_2$ flow rate of 1 SLM. In both cases, the experimental spectra are taken with the laser beam placed 2 mm above the burner exit, without the electrode tubes in place. The experimental spectra are plotted together with the best-fit CARSFT spectra, used to infer the temperature in the flame. The best-fit temperature in the circular flame is T = 1360 K (see Figure 5.14(a)). However, no good fit with a single-temperature CARSFT spectrum could be obtained in the elongated flame (see Figure 5.14(b)). Specifically, although the tail of the $N_2$ (v=0) band is reproduced relatively well by the synthetic spectrum with T = 1480 K, the shape of the head of the same band indicates the contribution of a low-temperature gas mixture. This is most likely due to incomplete mixing between hydrogen and ambient air, on a spatial scale of the length of CARS measurement region (a few mm), resulting in contribution of both low-temperature and

high-temperature regions into the CARS spectrum. Note that the CARS measurement region, approximately ≈ 4 mm long, is much shorter compared to the length of the flame, about 45 mm. The temperature estimated from the tail of the experimental spectrum is T ≈ 1500 K. Putting the discharge electrode tubes in place, at the gap with d = 15 mm, did not change this result significantly.

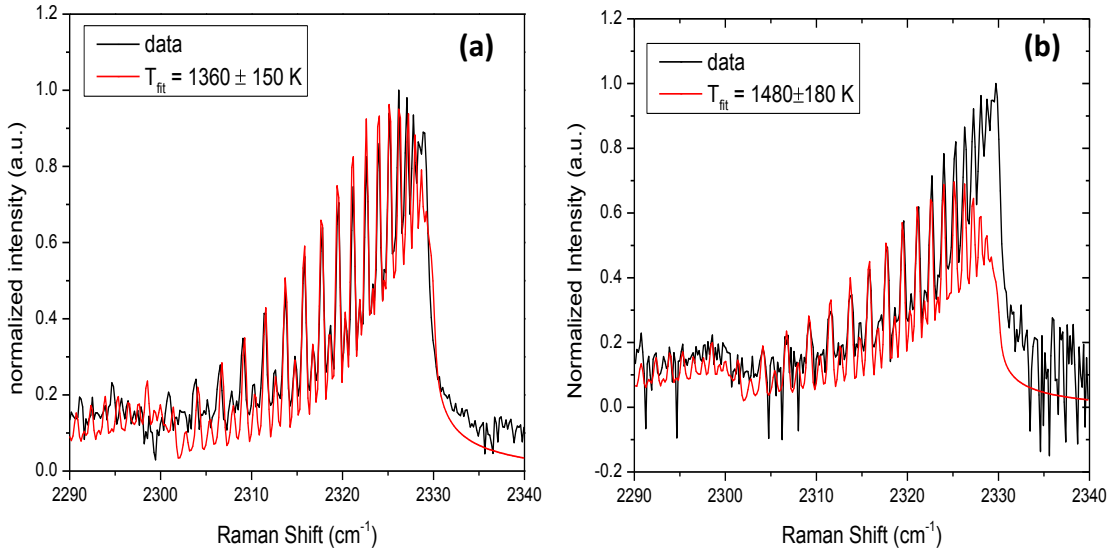


**Figure 5.14. CARS spectra of a hydrogen flame in a burner, (a) without the flame spreader, and (b) with the flame spreader for the electrode gap of *d* = 15 mm, when the flame is attached to the flame spreader (see Fig. 5.13(a)), plotted together with the best-fit CARSFT spectra. In both cases, $H_2$ flow rate is 1 SLM, laser beam is placed 2 mm above the burner exit.**

Reducing the gap between the electrode sleeves to d = 4 mm reduces dramatically both the CARS signal intensity and the temperature inferred from the CARS spectrum, to T = 370 K (see Figure 5.15). Note that the quality of the fit is not very good, both due to low signal-to-noise and the higher intensity maxima at the tail of the $N_2$(v = 0) band, which suggest contribution of a higher-temperature region. As discussed above, at these conditions, the flame is attached to the top of the electrode sleeves rather than the flame spreader exit (see Figure 5.12(b)), such that the temperature is measured in a hydrogen flow mixed with a small amount of ambient air, below the flame.

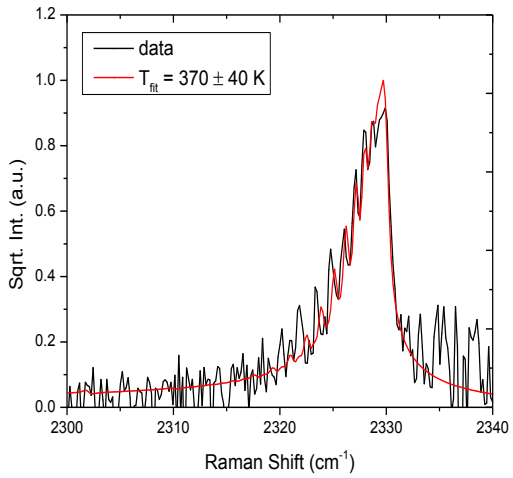


**Figure 5.15. CARS spectrum taken below the hydrogen flame in a burner with the flame spreader, for electrode gap of *d* = 4 mm, when the flame is attached to the top of the electrode sleeves (see Fig. 5.13(b)), plotted together with the best fit CARSFT spectra. Laser beam is 2 mm above the burner exit, $H_2$ flow rate is 1 slm. Best-fit temperature is T = 370 K.**

To estimate the temperature distribution in the flame, the effect of temperature non-uniformity across the CARS measurement volume was neglected, and the rotational-translational temperature was inferred from the synthetic spectrum providing best fit to the rotational structure of the tail of the $N_2(v = 0)$ band, as shown in Figure 5.14(b). Figure 5.16 shows a schematic of the locations where the temperature has been measured, as well as the horizontal and vertical temperature distributions inferred from the CARS spectra. It can be seen that the highest temperature region is about 5 mm wide and located approximately 5 – 7 mm above the flame spreader exit. The horizontal temperature distribution also suggests presence of two temperature maxima located on both sides of the flame spreader exit, approximately at x = -3 mm and x = 2 mm (see Figure 5.16). This is consistent with the flame visible emission intensity distribution (e.g. see Figure 5.12(a)) and suggests that combustion occurs in two hydrogen-air mixing layers attached to the side walls of the burner. Note, however, that the height of these maxima is comparable with the temperature inference uncertainty. The highest temperature is likely achieved when these two mixing layers overlap with each other, at y = 5 - 7 mm. As the vertical distance between the laser beam and the flame spreader exit is increased further, to y = 10 - 12 mm, the temperature begins to decrease, most likely due to mixing of combustion products with ambient air (see Figure 5.16).

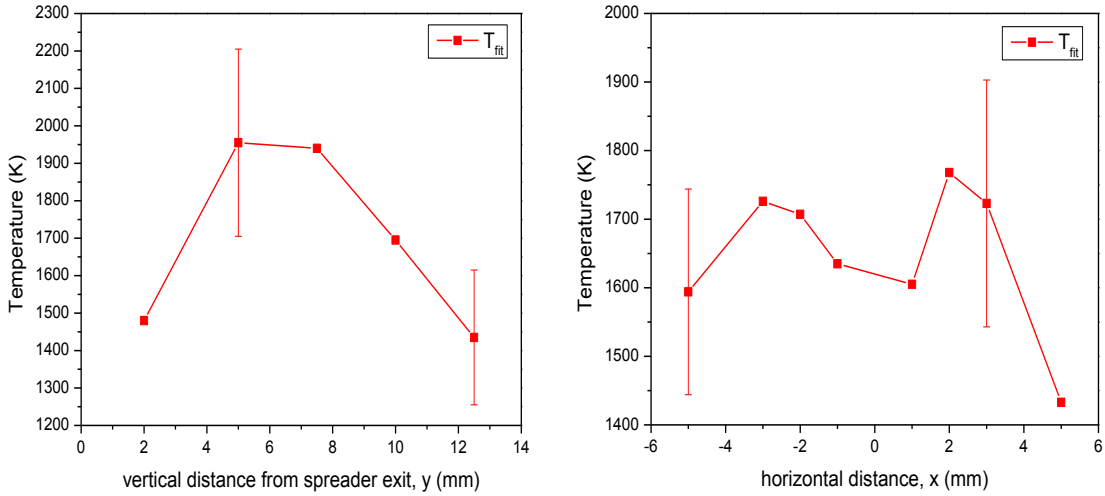


**Figure 5.16. (a) Vertical temperature distribution and (b) horizontal temperature distribution in the 1 SLM $H_2$ diffusion flame without the electrodes in place, inferred from CARSFT synthetic spectra, such as shown in Figure 5.14. Laser beam is placed 2 mm above the burner exit.**

**Flame Temperature vs. Applied AC Voltage**

| Condition | $T_{fit\text{-}tail}$ (K) | $T_{fit\text{-}head}$ (K) |
|---|---|---|
| No electrodes | 1480 | 590 |
| d = 15mm, $V_{peak}$= 7.4 kV | 1510 | 570 |
| d = 15mm, $V_{peak}$= 10 kV | 1530 | 510 |
| d = 15mm, $V_{peak}$= 14 kV | 1730 | 560 |

**Table 5.2. Temperatures inferred from CARSFT synthetic spectra at different AC voltages. Electrode gap is d = 15 mm, $H_2$ flow rate is 1 SLM. All measurements are taken on the center plane of the flame, 2 mm above the flame spreader exit.**

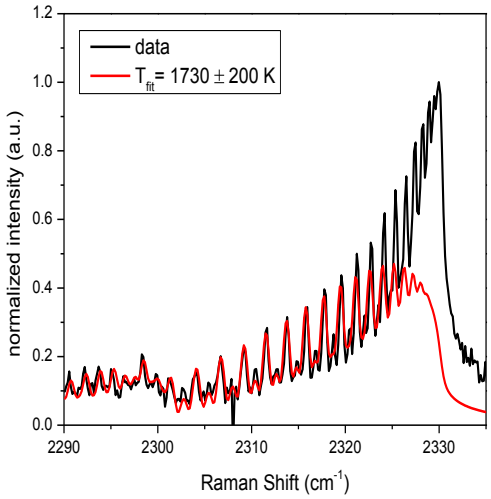


**Figure 5.17. CARS spectra of a hydrogen flame in a burner, with 14 kV, 3 kHz AC discharge in operation, with the temperature inferred from the best fit to the tail of the spectrum. Electrode gap d = 15 mm, $H_2$ flow rate = 1 SLM.**

Comparison of CARS spectra taken in the flame in a burner equipped with the flame spreader, with and without the 14 kV peak voltage, 3 kHz AC discharge sustained between the electrode sleeves separated by a gap of d = 15 mm (see Figure 5.17) shows that the temperatures estimated from the tail of the spectra are fairly close, T ≈ 1480 K and T ≈ 1730 K. This indicates that sustaining the AC DBD plasma in the flame does not results in a significant additional temperature rise. The results of flame temperature measurements with the AC discharge turned on are summarized in Table 5.2. Since no single-temperature synthetic spectrum fit could be obtained at these conditions, for each set of conditions temperatures inferred from the bestfit to the tail and the head of $N_2$ (v = 0) band are reported.

From Table 5.2, it can be seen that as long as the AC peak voltage remains below 14 kV, at the conditions when breakdown is not achieved and plasma is not generated, the

temperatures inferred from the CARS spectra remain essentially without a change. This is as expected, since below breakdown the AC discharge current could not be detected (except for the capacitive current), such that essentially no energy is coupled to the flow. When the peak voltage is increased to 14 kV, the plasma is generated between the electrode tubes, and the temperature inferred from the tail of the $N_2$ (v = 0) band increases from T ≈ 1480 K to T ≈ 1730 K, indicating additional energy dissipation in the AC discharge. However, the temperature rise remains relatively modest.

### 5.3.4. Electric Field Measurements in $H_2$ Diffusion Flames

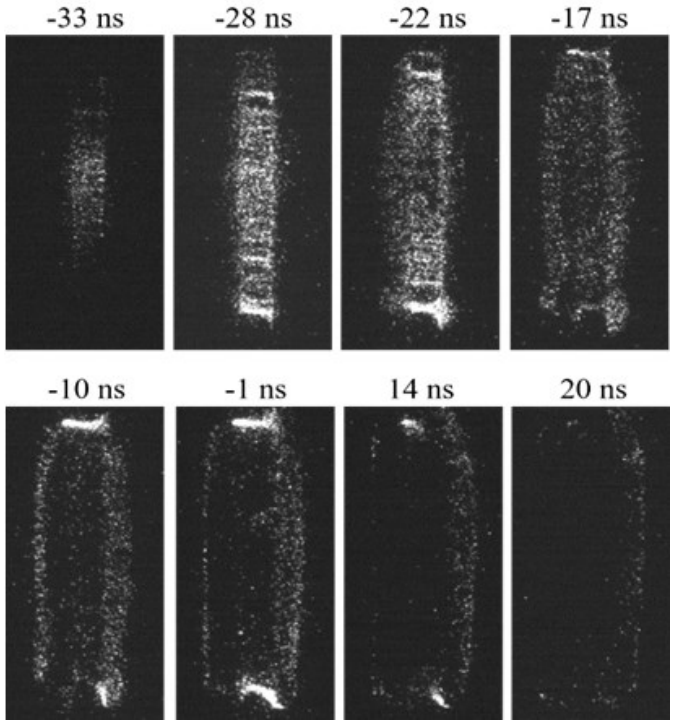


**Figure 5.18. Collage of single-shot plasma emission images taken during a positive polarity ns pulse discharge in a hydrogen flow below the flame. Hydrogen flow rate 1.5 SLM, pulse repetition rate 20 Hz, discharge gap d = 4.5 mm, camera gate 10 ns.**

Figure 5.18 shows a collage of single-shot plasma emission images taken during the positive polarity ns pulse discharge generated in a 1.5 SLM hydrogen flow below the flame, for the electrode gap of d = 4.5 mm. In these images, the camera gate is 10 ns, and t = 0 corresponds to the moment when the pulse voltage peaks. It can be seen that for both pulse polarities, the plasma is first generated in the central region between the electrode sleeves. The breakdown moment during the discharge pulse is indicated clearly by a well-pronounced current spike and a "kink" in the voltage waveforms, both reproducible shot-to-shot. After breakdown, the plasma extends both along the discharge gap and over the surface of the electrode sleeves, while emission in the central region between the electrodes decays, indicating electric field reduction due to charge separation and plasma self-shielding. The plasma eventually extends to the ends of the alumina ceramic electrode sleeves and the exposed parts of the electrodes, generating bright localized emission. At this moment, the applied voltage begins to decrease. The plasma between the electrodes remains fairly diffuse, without well-pronounced filaments, except near the exposed electrodes.

Increasing the discharge gap to d = 12 mm while keeping the $H_2$ flow rate the same, when the flame becomes attached to the exit of the flame spreader, results in ns pulse discharge plasma becoming more filamentary. Figures 5.19 show single-shot 10 ns gate plasma emission images taken during the positive polarity ns pulse discharge at these conditions, as well as a 50-shot image with a 400 ns gate "wrapped around" the entire applied voltage pulse. In this case, the plasma is sustained in the flame as well as in the ambient air flow near the electrode sleeves, on both sides of the flame. It can be seen that in this case every discharge pulse generates several fairly well-pronounced streamers. A 50-

shot accumulation image shown in Figure 5.19 indicate that these streamers remain fairly random, generating quasi-diffuse time-averaged emission.

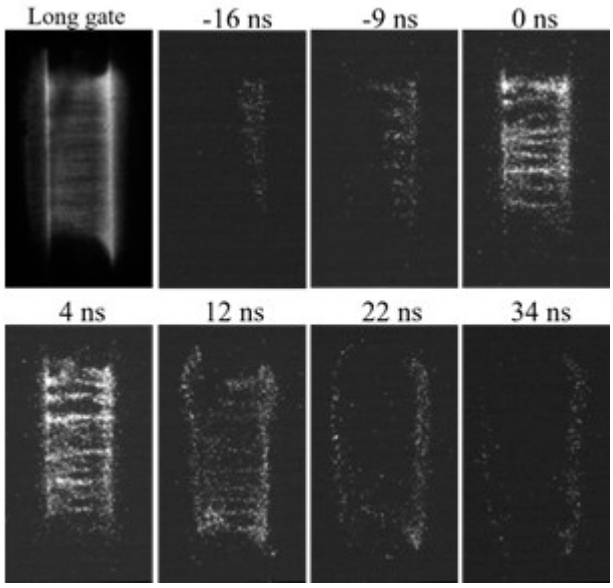


**Figure 5.19. Collage of single-shot, 10-ns camera gate plasma emission images, and a 50-shot, 400-ns camera gate accumulation image, taken during a positive polarity ns pulse discharge in a hydrogen flame. Hydrogen flow rate 1.5 SLM, pulse repetition rate 20 Hz, discharge gap *d* = 12 mm.**

Figure 5.20 plots horizontal electric field in a positive polarity ns pulse discharge at pulse peak voltage of 15 kV. Electric field data are plotted together with pulse voltage and current waveforms. It can be seen that the electric field follows the applied voltage pulse until breakdown, when the current increases abruptly and the field decays rapidly due to plasma self-shielding. The electrostatic electric field between the parallel cylinder electrodes in alumina ceramic sleeves before breakdown is calculated by solving the Laplace equation.

Breakdown field measured at the present conditions is $E_{br} \approx 19$ kV/cm, very close to the prediction of Paschen law in hydrogen at atmospheric pressure and room temperature [23]. Rapid reduction of the electric field after breakdown is consistent with the plasma emission images, shown in Figure 5.18, which indicate the decay of plasma emission intensity between the electrodes following breakdown. Note that plasma self-shielding occurs as the ionization wave propagates along the surface of the electrode sleeves (see Figure 5.18). When the wave reaches the exposed parts of the electrodes, both the applied voltage and the electric field are gradually reduced to near detection limit. No detectable electric field offset is observed either before or after the discharge pulse, indicating that residual surface charge accumulation from the previous pulse, as well charge accumulation after the pulse, are insignificant.

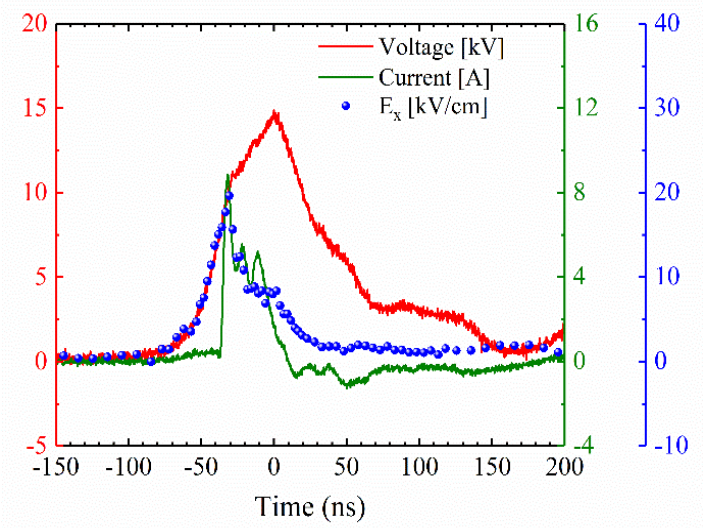


**Figure 5.20. Horizontal electric field in a positive polarity ns pulse discharge in a hydrogen flow below the flame, plotted together with pulse voltage and current waveforms. Hydrogen flow rate 1.5 SLM, pulse repetition rate 20 Hz, discharge gap d = 4.5 mm.**

Figure 5.21 plots the electric field measured in the ns pulse discharge between the electrode sleeves placed d = 12 mm apart, at the same $H_2$ flow rate of 1.5 SLM. As discussed above, at these conditions, when the flame becomes attached to the exit of the flame spreader, the plasma becomes more filamentary (see Figure 5.19). Comparing Figures 5.20 and 5.21, it can be seen that in the discharge with the larger electrode gap, breakdown occurs later during the pulse, near the pulse voltage peak. Breakdown field, on the other hand, is almost a factor of two lower compared to that in hydrogen below the flame, $E_{br} \approx 9$ kV/cm, due to much higher temperature in the central part of the discharge gap (compare Figures 5.14(b) and 5.15). Also, the apparent plasma self-shielding effect is significantly less pronounced. This occurs since the present diagnostics measures the absolute value of the electric field averaged over the length of the flame and the overlapping length of the

electrodes, approximately 50 mm. Therefore the field is averaged over the regions where the plasma self-shielding is strong (in the filaments) as well as over the regions between the filaments, where the self-shielding is less significant. Similar to the electric field measurements in the discharge with the gap of d = 4.5 mm gap, no electric field offset due to surface charge accumulation or vertical electric field were detected.

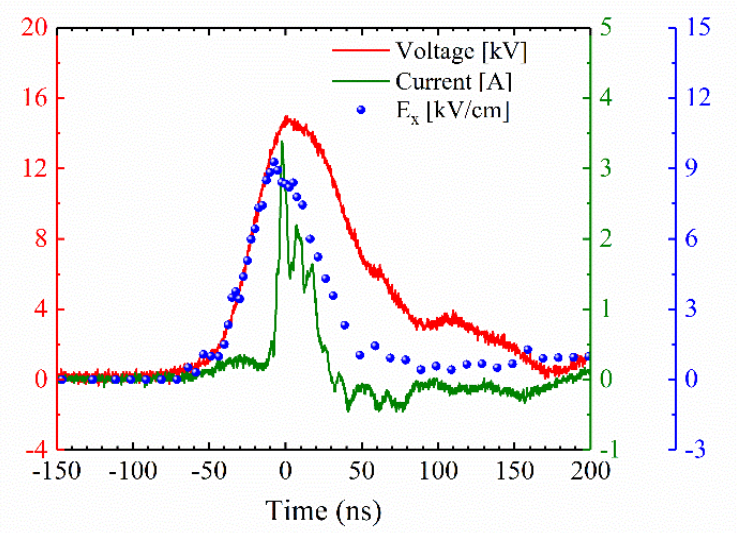


**Figure 5.21. Horizontal electric field in a positive polarity ns pulse dischage in a hydrogen flame, plotted together with pulse voltage and current waveforms. Hydrogen flow rate 1.5 SLM, pulse repetition rate 20 Hz, discharge gap *d* = 12 mm.**

Figure 5.22 shows plasma emission images in the AC dielectric barrier discharge in a hydrogen flame, taken at hydrogen flow rate of 2 SLM, at the peak voltage of 14 kV, AC frequency of 3 kHz, and electrode gap of d = 12 mm, when the flame is attached to the flame spreader. A 50-shot accumulation, full AC period (333 μs) camera gate image exhibits a quasi-diffuse plasma, while single-shot and 10-shot accumulation, 20 μs gate images taken during positive and negative AC half-periods clearly show individual well-defined filaments (micro-discharges) extending between the electrode sleeves. The average number of filaments generated during the positive polarity AC period exceeds that during the negative polarity half-period (see Figure 5.22). At these conditions, the discharge current waveforms also indicate micro-discharges generated during positive and negative AC half-periods and separated by ~10 μs, with positive polarity current peaks exceeding those of negative polarity. As expected, a 50-period accumulation image illustrates that the micro-discharges are fairly random, generating quasi-diffuse plasma emission. As discussed in Section 5.3.2, the second harmonic signal measured in the present work is accumulated over the entire distance between the overlapping electrodes, such that the measured electric field represents a root mean square value averaged along the electrodes, including both the field in the micro-discharges and in the regions between the micro-discharges.

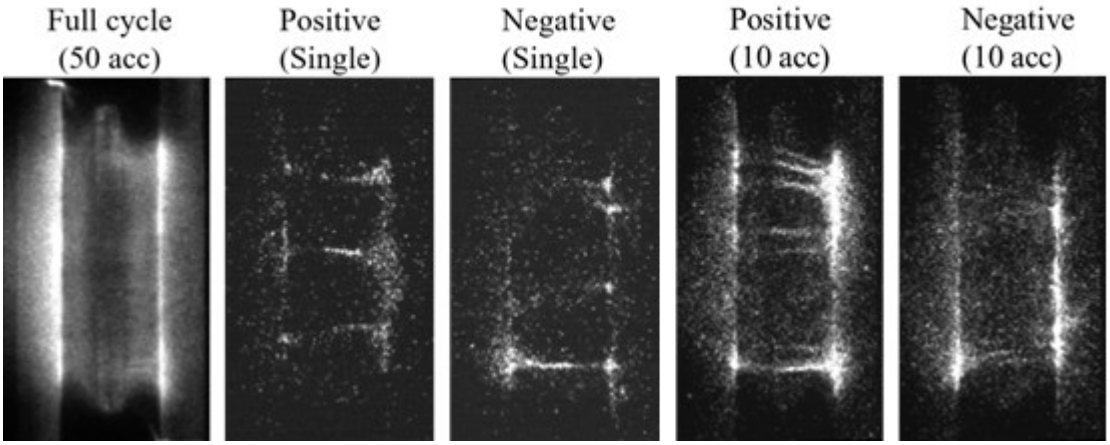


**Figure 5.22. Full AC period (333 μs) camera gate, 50-shot accumulation plasma emission image, two 20 μs gate, single-shot images, and two 20 μs gate, 10-shot accumulation images taken during positive and negative half-periods of AC dielectric barrier discharge in a hydrogen flame. Hydrogen flow rate 2 SLM, AC frequency 3 kHz, peak voltage 14 kV, electrode gap d = 12 mm.**

Figure 5.23 plots second harmonic signal calibration for the horizontal component of the electrostatic field in the hydrogen flame without the plasma, and the absolute value of the horizontal field in the AC dielectric barrier discharge in the hydrogen flame. Unlike in ns pulse discharges, putting the electric field measured in the AC discharge on the absolute scale requires separate calibration (see Figure 5.23(a)). The data are taken at the $H_2$ flow rate of 1 SLM, AC frequency of 3 kHz, and the electrode gap of d = 15 mm. For calibration, the AC peak voltage was reduced from 14 kV to 8 kV, until the plasma was no longer generated between the electrodes. No evidence of breakdown or the effect of ion wind on the flame was detected during the calibration. Without the plasma, it can be seen that the square root of the second harmonic signal follows the absolute value of the applied voltage closely, indicating no detectable space charge effect, due to weak chemi-ionization in the flame. Note that since the second harmonic signal is proportional to the absolute value of

the electric field, the negative half-period of the applied voltage, when the electrostatic electric field clearly changes direction (at t = 167 - 333 μs), is inverted.

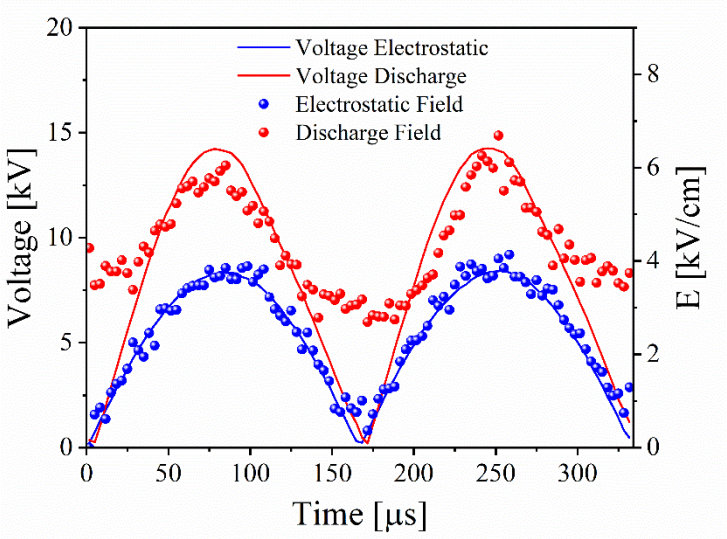


**Figure 5.23. (a) Second harmonic signal calibration for the absolute value of the horizontal component of the electrostatic field ($E_x$) in the hydrogen flame without the plasma; (b) absolute value of the horizontal component of the field in the AC dielectric barrier discharge in the flame. $H_2$ flow rate 1 SLM, AC frequency 3 kHz, electrode gap d = 15 mm. Non-zero field offset resulting in ion wind is apparent.**

With the AC plasma on, non-zero offset in the second harmonic signal (i.e. horizontal electric field offset of approximately 3 kV/cm, similar to the peak-to-peak variation of the periodic electric field component) is readily apparent in Figure 5.23(b). Combining this result with the AC plasma images shown in Figure 5.22, which illustrate formation of individual micro-discharges, suggests that the net second harmonic signal is due to the AC electric field produced by the applied voltage, combined with the field induced by charge accumulation on the electrode sleeves by the ensemble of random micro-discharges

shielding the applied field. This near-DC electric field is likely to be responsible for generation of the ion wind, which results in flame distortion and motion toward the grounded electrode, observed during the experiments (see Figure 5.11(f)). Since the extent of the regions where the fields due to charge accumulation and the applied AC field are produced is uncertain, estimating their individual magnitudes from the present data is challenging. Therefore Figure 5.23 plots only the root mean square value of the net horizontal electric field averaged over the length of the electrodes, measured by the present diagnostics. Note that using the electrostatic calibration in Figure 5.23 assumes that the chemical composition of the combustion products is not affected by the plasma and by the ion wind, which at this time remains an open question.

# Chapter 6. Summary

In this dissertation, broadband ns Coherent Anti-Stokes Raman Spectroscopy (CARS) diagnostics is used to study vibrational energy transfer in the afterglow of a diffuse filament, ns pulse discharge in nitrogen, air, and their mixtures with carbon dioxide and hydrogen, in two closely related experiments. The objective of the first experiment was to study feasibility of control of vibrational distribution of $N_2$ in nonequilibrium plasmas sustained in nitrogen and air by rapid vibration-vibration energy transfer to $CO_2$. Time-resolved $N_2$(v=0-3) vibrational level populations and temperature in the afterglow of a diffuse filament ns pulse discharge are measured by CARS in collinear phase-matching geometry, with pump and Stokes laser beams directed along the plasma filament through ports drilled in the discharge electrodes. Spatial resolution of the CARS measurements along the discharge filament is approximately 4 mm. Rotational-translational temperature in the afterglow is inferred from the partially rotationally resolved structure of the $N_2$(v=0) band. The results indicate that nitrogen vibrational excitation in the discharge occurs by electron impact, with subsequent vibration-vibration (V-V) energy transfer within $N_2$ vibrational manifold, vibration-translation (V-T) relaxation, and near-resonance V-V′ energy transfer from $N_2$ to $CO_2$ asymmetric stretch vibrational mode. The results also show that rapid V-V′ energy transfer to $CO_2$, followed by collisional intramolecular energy redistribution to symmetric stretch and bending modes of $CO_2$ and their V-T relaxation, considerably accelerate the net rate of energy thermalization and temperature rise in the afterglow. This demonstrates that adding $CO_2$, a rapid V-T relaxer species, to nonequilibrium flows of nitrogen and air would result in a rapid temperature increase. In compressible flows, this would also result in pressure increase, inducing significant changes in the flow field. This result is consistent

with recent experiments in a nonequilibrium supersonic shear layer, where accelerated vibrational relaxation of nitrogen induced by injection of $CO_2$ resulted in a transient pressure rise and a shear layer displacement. The present results show that significant amounts of vibrational energy can be stored in nonequilibrium nitrogen and air flows and released at a desired location, using local injection of rapid "relaxer" species such as $CO_2$ or hydrocarbons, and producing a significant effect on the high-speed flow. Modulated flow perturbations can also be produced using this approach, by repetitive loading of energy into $N_2$ vibrational mode by a repetitively pulsed electric discharge.

In the second experiment in a diffuse filament ns pulse discharge, time-resolved measurements of temperature, $N_2$ vibrational temperature, and absolute OH number density in nitrogen, air, and $H_2$-air mixtures are used to study a possible effect of nitrogen vibrational excitation on low-temperature kinetics of $HO_2$ and OH radicals, at high specific energy loading. Translational-rotational temperature and $N_2$ vibrational temperature in the discharge and the afterglow are measured by ns broadband, degenerate-pump CARS, using the same approach as in the first experiment. The uncertainty of translational-rotational temperature and vibrational temperature inference is ±50 K and ±200 K, respectively. OH number density is measured by LIF, using direct measurements of LIF quenching rate and absolute calibration by Rayleigh scattering. CARS measurements demonstrate that the discharge generates strong vibrational nonequilibrium in air and $H_2$-air mixtures for delay times after the discharge pulse up to ~ 1 ms, with peak $N_2$ vibrational temperature of up to $T_v$ = 1700-1900 K at T = 500-580 K. $N_2$(v=0-2) vibrational levels are detected both in air and $H_2$-air mixtures. The kinetics of population and decay of $N_2$ vibrational levels at these conditions are well understood, based both on previous CARS measurements and on kinetic modeling predictions. LIF measurements show that OH number density increases gradually

after the discharge pulse, starting at t = 10 μs, before peaking at t ~ 100-300 μs (depending on the $H_2$ fraction in the mixture), and decaying on a longer time scale, until t ~ 1 ms. Increasing the discharge pulse energy from 7.5 mJ to 10.0 mJ results in the peak OH number density increase by up to a factor of three. The peak OH number density in $H_2$-air mixtures is reached at approximately the same time as peak $N_2$ vibrational temperature. Comparison of the experimental data with kinetic modeling predictions shows that OH kinetics at the present conditions is controlled primarily by reactions of $H_2$ and $O_2$ with O and H atoms generated during the discharge. At the present conditions, OH number density is not affected by $N_2$ vibrational excitation directly, i.e. via vibrational energy transfer to $HO_2$. However, as the discharge pulse coupled energy is increased, the model predicts a transient OH number density overshoot due to the temperature rise caused by $N_2$ vibrational relaxation by O atoms, which may well be a dominant effect in discharges with high specific energy loading.

In the third experiment, ns broadband CARS diagnostics developed to study vibrational energy transfer and kinetics of energy thermalization in ns pulse discharge plasmas has been used to characterize a microwave discharge in nitrogen. The objective of this study was to determine the potential of a cw microwave discharge for energy-efficient plasmachemical dissociation of $CO_2$. In addition to its accessibility to CARS measurements, nitrogen was chosen for this study since discharge energy fractions going to vibrational excitation of $N_2$ and $CO_2$ in nonequilibrium discharge plasmas are comparable, and since $N_2$ vibrational relaxation rate is much slower compared to that of $CO_2$. This means that measurements of vibrational and rotational-translational temperatures in nitrogen plasma would provide an upper bound estimate of vibrational nonequilibrium in $CO_2$ plasma, at the

same microwave discharge power, pressure, and flow rate. The measurement results indicate that rotational-translational temperature in a cw microwave discharge plasma in nitrogen is very high, up to T=2000 K, such that it is extremely unlikely that significant $N_2$ vibrational nonequilibrium can be sustained at these conditions. Vibrational nonequilibrium of $CO_2$ at these conditions is even more unlikely, since $CO_2$ vibrational relaxation is considerably more rapid. However, operating a pulsed microwave discharge at a very low duty cycle, 0.6%, resulted in significant $N_2$ vibrational nonequilibrium. At these conditions, peak vibrational temperature of $T_V$= 2100 ± 250 K was achieved at t = 90 μs after the beginning of the microwave discharge pulse. Peak rotational-translational temperature, T ≈ 530 ± 50 K, is measured in the afterglow, at t = 400 μs after the beginning of discharge pulse. On a longer time scale, the plasma rapidly approaches near thermal equilibrium. These results suggest that energy efficient $CO_2$ dissociation in pure $CO_2$ or in $CO_2$-$N_2$ microwave discharges may be achieved either during pulsed operation or at conditions when the flow residence time in the discharge is very short, as occurs in discharges sustained in supersonic flows. $CO_2$ CARS diagnostics has also been used in this experiment. However, it does not appear to have significant potential for characterization of microwave discharge plasmas in $CO_2$ due to its low sensitivity to variation of the rotational-translational temperature.

Finally, ns broadband CARS diagnostics, combined with CARS-like ps Four-Wave Mixing and ps Second Harmonic Generation diagnostics, has been used for temperature and electric field measurements in atmospheric pressure hydrogen diffusion flames, enhanced by ns pulse and AC discharges. Electric field is put on the absolute scale using the Laplacian field measured before breakdown, and reduced electric field (E/N) is estimated from the

electric field and temperature measurements. Without the discharge electrodes in place, the temperature in the atmospheric pressure hydrogen diffusion flame is T = 1300 ± 150 K. With the electrodes in place, the experimental CARS spectra can no longer be represented by single-temperature synthetic spectra, indicating incomplete mixing of high-temperature combustion products with ambient air, due to the narrow gap between the electrodes, resulting in contributions of both low-temperature and high-temperature regions into the spectra. At these conditions, the temperature was estimated from the best fit of the synthetic spectra to the tail of the $N_2$(v=0) band, T ≈ 1400-1500 K. The four-wave mixing measurements show that peak electric field during breakdown in the flame, approximately 40 kV/cm, is significantly lower compared to that in room air, 75 kV/cm, due to the higher temperature (lower number density) of the combustion products. Both in air and in the flame, the electric field follows the applied voltage before breakdown and decreases rapidly after breakdown, due to charge separation and plasma self-shielding. Peak reduced electric field in the plasma sustained in the flame varies from E/N=300 Td to 800 Td, indicating that most of the discharge input energy goes to electronic excitation of nitrogen, dissociation of oxygen, and ionization, generating reactive species. The sensitivity of the ps four-wave mixing measurements of electric field is the atmospheric pressure flame is fairly low, ~20 kV/cm, mainly due to higher temperature and lower $N_2$ fraction in the combustion product mixture.

To improve the signal-to-noise, electric field in a hydrogen diffusion flame in a slightly different geometry burner equipped with a flame spreader was measured by ps Second Harmonic Generation diagnostics. At these conditions, temperature inference from the CARS spectra was again complicated by incomplete mixing of high-temperature

combustion products with ambient air in the elongated flame, such that the temperature was estimated from the best fit of the synthetic spectra to the tail of the $N_2$(v=0) band. Temperature distribution in the flame was measured vs. the height above the burner exit and vs. the transverse distance across the flame, with the temperature at the burner exit of T ≈ 1500 K and peak temperature of T ≈ 1950 K. Putting the discharge electrodes in place did not change the temperature at the burner exit, unless the distance between the electrodes was significantly reduced, when the flame became attached to the top of the electrodes. In this case, the flow at the burner exit (below the flame) is predominantly hydrogen with a small admixture of air, with a very low temperature of T ≈ 370 K. The electric field measurement results demonstrated that the sensitivity of ps Second Harmonic Generation in the flame is much better compared to ps Four-Wave Mixing, ~2 kV/cm, and it allows straightforward, non-intrusive measurements of time-resolved and spatially-resolved electric field in atmospheric pressure flames enhanced by ns pulse and AC sine wave dielectric barrier discharge (DBD). Again, electric field measurements in a ns pulse discharge are self-calibrating, since the field follows the applied voltage until breakdown. No additional calibration is necessary in this case, and chemical composition of the reacting mixture does not need to be known. Both temperature and time-resolved electric field are measured in a ns pulse discharge sustained both in the low-temperature hydrogen flow below the flame (for small electrode gaps) and in the hydrogen diffusion flame (for large electrode gaps). In both cases, the electric field rapidly decreases to near zero after breakdown, which is identified by a sudden rise in the discharge current, due to plasma self-shielding. Peak reduced electric field measured in a near-room temperature hydrogen flow is close to breakdown field in hydrogen predicted by Paschen law (electric field of 19 kV/cm, reduced electric field of ≈ 100 Td). Peak electric field in the flame is significantly lower, 9

kV/cm, due to the lower number density in the plasma at these conditions. Knowledge of the reduced electric field variation during and after breakdown is critical for predicting energy partition in the plasma and number densities of excited species and radicals generated in the plasma. In the AC plasma, the electric field data are put on the absolute scale by measuring an electrostatic electric field between the parallel cylinder electrodes and comparing the results with the numerical solution of the Laplace equation for the electric potential in this geometry. The accuracy of the calibration depends on whether the AC plasma affects the chemical composition of the flow at these conditions, which has not been studied in the present work. The measurement results demonstrate that strong electric field in the plasma-enhanced flame is produced during the entire AC voltage period, without any apparent correlation with the discharge current waveform (i.e. with random micro-discharges detected in the plasma images). The measurement results indicate higher peak electric field during the negative AC half-period, in spite of symmetric electrode geometry, as well as significant near-DC electric field offset. The asymmetry and the offset of the electric field are likely responsible for the electrohydrodynamic (EHD) body force ("ion wind") resulting in flame distortion, which is one of the dominant effects of the electric field at these conditions.

Future work using ns broadband CARS diagnostics developed during these studies includes measurements of translational-rotational temperature and vibrational temperature in supersonic nonequilibrium flows, to detect and quantify the effect of vibrational relaxation on the supersonic flow field.

# Bibliography

[1] Y. P. Raizer, “Gas Discharge Physics”, Berlin: Springer (1997).

[2] S. Leonov, V. Petrishchev and I. Adamovich, “Dynamics of Energy Coupling and Thermalization in Barrier Discharges over Dielectric and weakly Conducting Surfaces on us to ms time scale”, Journal of Physics D: Applied Physics, Vol. 47, 2014, 465201

[3] A. Montello, Z. Yin, D. Burnette, I. Adamovich, and W. Lempert, “Picosecond CARS Measurements of Nitrogen Vibrational Loading and Rotational/Translational Temperature in Non-equilibrium Discharges”, Journal of Physics D: Applied Physics, Vol. 46, 2013, 464002

[4] S. Lanier, I. Shkurenkov, I. Adamovich, and W. Lempert, “Two-stage Energy Thermalization Mechanism in Nanosecond Pulse Discharges in Air and Hydrogen-air Mixtures”, Plasma Sources Science and Technology, Vol. 24, 2015, 025005

[5] I. Shkurenkov and I. Adamovich, “Energy Balance in Nanosecond Pulse Discharges in Nitrogen and Air”, Plasma Sources Science and Technology, Vol. 25, 2016, 015021

[6] K. Frederickson, Y.-C. Hung, W.R. Lempert, and I.V. Adamovich, "Control of Vibrational Distribution Functions in Nonequilibrium Molecular Plasmas and High-Speed Flows", Plasma Sources Science and Technology, Vol. 26, 2017, 014002

[7] I. V. Adamovich, S. B. Leonov, K. Frederickson, J. G. Zheng, Y. D. Cui, and B. C. Khoo, “Thermal perturbations generated by near-surface electric discharges and mechanisms of their interaction with the airflow”, AIAA Paper 2017-1339, 55th AIAA Aerospace Sciences Meeting (SciTech 2017), 9-13 January 2017, Grapevine, TX

[8] A. Starikovskiy, and N. Aleksandrov “Plasma-assisted ignition and combustion”, Progress in Energy and Combustion Science, vol. 39(1), 2013, pp. 61-110.

[9] Y. Ju. & W. Sun,“Plasma assisted combustion: dynamics and chemistry”, Progress in Energy Combustion Science, vol. 48, 2015, pp. 21-83.

[10] N. A. Popov “Effect of a pulsed high-current discharge on hydrogen-air mixtures”, Plasma Physics Reports, vol. 34(5), 2008, pp. 376-391.

[11] Z. Yin, K. Takashima, and I. V. Adamovich, "Ignition Time Measurements in Repetitive Nanosecond Pulse Hydrogen-Air Plasmas at Elevated Initial Temperatures", IEEE Transactions on Plasma Science, vol. 39, 2011, pp. 3269-3282

[12] M. Nishihara, I. V. Adamovich, W. R. Lempert, and J.W. Rich, "Effect of Accelerated Vibrational Relaxation on a Supersonic Shear Layer", AIAA Paper 2015-0577, 53rd AIAA Aerospace Sciences Meeting (SciTech 2015), 5-9 January 2015, Kissimmee, Florida

[13] T. J. Fuller, A. G. Hsu, R. Sanchez-Gonzalez, J. C. Dean, S. W. North & R. D. Bowersox ," Radiofrequency plasma stabilization of a low-Reynolds-number channel flow", Journal of Fluid Mechanics, vol. 748, 2014, pp. 663–691

[14] M. Nishihara, K. A. Frederickson, and W. R. Lempert, "Single / Dual Pump CAR Measurements in Vibrationally Relaxing Supersonic Mixing Layer", AIAA Paper 2016-1762, 54th AIAA Aerospace Sciences Meeting (SciTech 2016), 4-8 January 2016, San Diego, CA

[15] D. Burnette, A. Montello, I. V. Adamovich, and W. R. Lempert, "Nitric Oxide Kinetics in the Afterglow of a Diffuse Plasma Filament", Plasma Sources Science and Technology, vol. 23, 2014, 045007

[16] L. Wu, J. Lane, N. P. Cernansky, D. L. Miller, A. A. Fridman & A. Y. Starikovskiy, "Plasma-assisted ignition below self-ignition threshold in methane, ethane, propane and butane-air mixtures." Proceedings of the Combustion Institute, vol. 33(2), 2011, pp. 3219-3224.

[17] C. Winters, Y.-C. Hung, E. Jans, Z. Eckert, K. Frederickson, I. V. Adamovich, and N. Popov, "OH Radical Kinetics in Hydrogen-Air Mixtures at the Conditions of Strong Vibrational Nonequilibrium", Journal of Physics D: Applied Physics, vol. 50, 2017, 505203

[18] A. Lo, G. Cléon, P. Vervisch and A. Cessou "Spontaneous Raman scattering: a useful tool for investigating the afterglow of nanosecond scale discharges in air", Applied Physics B, vol. 107, 2102, p. 229

[19] A. Lo, A. Cessou, P. Boubert, and P. Vervisch "Space and time analysis of the nanosecond scale discharges in atmospheric pressure air: I. Gas temperature and vibrational distribution function of $N_2$ and $O_2$", Journal of Physics D: Applied Physics, vol. 47, 2014, 115201

[20] A. Lo, A. Cessou and P. Vervisch "Space and time analysis of the nanosecond scale discharges in atmospheric pressure air: II. Energy transfers during the post-discharge", Journal of Physics D: Applied Physics, vol. 47, 2014, 115202

[21] Z. Yin, A. Montello, C. D. Carter, W. R. Lempert, and I. V. Adamovich, "Measurements of temperature and hydroxyl radical generation/decay in lean fuel–air mixtures excited by a repetitively pulsed nanosecond discharge", Combustion and Flame, vol. 160(9), 2013, pp. 1594-1608.

[22] I. V. Adamovich, T. Li, and W. R. Lempert “Kinetic mechanism of molecular energy transfer and chemical reactions in low-temperature air-fuel plasmas.” Philosophical Transaction of the Royal Society A, vol. 373, 2015, 20140336

[23] A. Fridman, Plasma Chemistry. Cambridge University Press (2012)

[24] A. Lebouvier, S. A. Iwarere, P. d’Argenlieu, D. Ramjugernath, and L. Fulcheri, “Assessment of Carbon Dioxide Dissociation as a New Route for Syngas Production: A Comparative Review and Potential of Plasma-Based Technologies”, Energy and Fuels, vol. 27(5), 2013, pp. 2712-2722

[25] N. Harder, D. van den Bekerom, R. S. Al, M. F. Graswinchel, J. M. Palomares, F. J. J. Peeters, S. Ponduri, T. Minea, W. A. Bongers, M. C. M. can de Sanden and G. J. Rooij, Homogenouse “$CO_2$ conversion by microwave discharge plasma: Wave propagation and diagnostics”, Plasma Processes and Polymers, vol. 14(6), 2017, 1600120

[26] C. E. Treanor, J. W. Rich & R. G. Rehm, “Vibrational Relaxation of Anharmonic Oscillators with Exchange-Dominated Collisions”, Journal of Chemical Physics, vol. 48 ,1968, p. 1798

[27] R. L. Taylor & S. Bitterman, “Survey of Vibrational Relaxation Data for Processes Important in the $CO_2$-$N_2$ Laser System”, Reviews of Modern Physics, vol. 41(26), 1969

[28] G. J. Rooij, D. C. M. van den Bekerom, N. den Harder, T. Minea, G. Berden, W. A. Bongers, R. Engeln, M. F. Graswinckel, E. Zoethout, and M. C. M. can de Sanden “Taming microwave plasma to beat thermodynamics in CO2 dissociation”, Faraday Discussions, vol. 183, 2015, p. 233

[29] P. Versailles, W. A. Chishty, and H. D. Vo, “Application of dielectric barrier discharge to improve the flashback limit of a lean premixed dump combustor”, Journal of Engineering for Gas Turbines and Power, vol. 134, 2012, 031501

[30] M. Cha, S. Lee, K. Kim, and S. Chung, “Soot suppression by nonthermal plasma in coflow jet diffusion flames using a dielectric barrier discharge”, Combustion and Flame, vol. 141 , 2005, p. 438

[31] D. G. Park, S. H. Chung, and M. S. Cha, “Bidirectional ionic wind in nonpremixed counter flow flames with DC electric fields”, Combustion and Flame, vol. 168, 2016, pp. 138-146

[32] J. E. Retter, G. S. Elliott, and S. P. Kearney, “Dielectric-barrier-discharge plasma-assisted hydrogen diffusion flame. Part 1: Temperature, oxygen, and fuel measurements by onedimensional fs/ps rotational CARS imaging”, Combustion and Flame, vol. 191, 2018, pp. 527-540

[33] T. Ito, K. Kobayashi, S. Müller, D. Luggenhölscher, U. Czarnetzki, and S. Hamaguchi, “Electric Field Measurement in an Atmospheric or Higher pressure gas by Coherent Raman Scattering of Nitrogen”, Journal of Physics D: Applied Physics, vol. 42, 2009, 092003

[34] T. Ito, T. Kanazawa, and S. Hamaguchi. "Rapid Breakdown Mechanisms of Open Air Nanosecond Dielectric Barrier Discharges", Physics Review Letters, vol. 107, 2011, 065002

[35] M. Simeni Simeni, B. Goldberg, I. Gulko, K. Frederickson, and I. V. Adamovich, “Subnanosecond resolution electric field measurements during ns pulse breakdown in ambient air”, Journal of Physics D: Applied Physics, vol. 51, 2018, 01LT01

[36] M. Simeni Simeni, B. M. Goldberg, C. Zhang, K. Frederickson, W. R. Lempert, and I. V. Adamovich, "Electric Field Measurements in a Nanosecond Pulse Discharge in Atmospheric Air", Journal of Physics D: Applied Physics, vol. 50, 2017, p. 184002

[37] M. Simeni Simeni, E. Baratte, Y.-C. Hung, K. Frederickson, and I.V. Adamovich, “Ps FourWave Mixing Measurements of Electric field in a Ns Pulse Discharge in a Hydrogen Diffusion Flame”, accepted for publication in Proceedings of the Combustion Institute, 2018

[38] A. Dogariu, B. M. Goldberg, S. O’Byrne, and R. B. Miles, “Species-independent femtosecond localized electric field measurement”, Physical Review Applied, vol. 7, 2017, 024024

[39] B. M. Goldberg, T. L. Chng, A. Dogariu, and R. B. Miles, “Electric field measurements in a near atmospheric pressure nanosecond pulse discharge with picosecond electric field induced second harmonic generation”, Applied Physics Letters, vol. 112, 2018, 064102

[40] S. Roy, J. R. Gord & A. K. Patnaik, "Recent advances in coherent anti-Stokes Raman scattering spectroscopy: Fundamental developments and applications in reacting flows", Progress in Energy and Combustion, vol. 36(2), 2010, pp. 280-306

[41] P. F. Bernath, “Spectra of Atoms and Molecules 2nd edition”, Oxford University Press (2005)

[42] A. C. Eckbreth, “Laser Diagnostics for Combustion Temperature and Species”, CRC Press (1996)

[43] F. Duarte and L. Hillman, “Dye Laser Principles: With Applications”, Elsevier (2012)

[44] C. Winters, “Laser Diagnostics of Reacting Molecules for Plasma Assisted Combustion”, Ph.D dissertation, Ohio State University, 2017

[45] Z. Eckert, ”Energy Transfer in Nonequilibrium Reacting Flows: Application in Plasma Assisted Combustion and Chemical Gas Lasers ”, Ph.D dissertation, OSU State University, 2018

[46] R. E. Palmer, The CARSFT Computer Code for Calculating Coherent Anti-Stokes Raman Spectra: User and Programmer Information, Report No. SAND89-8206, Sandia National Laboratories, Livermore, CA, 1989

[47] M. Cacciatore, A. Kurnosov & A. Napartovich, “Vibrational Energy Transfer in $N_2$-$N_2$ Collisions: a New Semiclassical Study”, Journal of Chemical Physics, vol. 123(17), 2005, p. 174315

[48] G. D. Biling and E. R. Fisher, “VV and VT rate coefficients in $N_2$ by a quantum classical model”, Journal of Chemical Physics, 43(3), 1979, pp. 395-401

[49] LXcat database: www.lxcat.laplace.univ-tlse.fr

[50] I. A. Kossyi, A. Y. Kostinsky, A. A. Matveyev, and V. P. Silakov, “Kinetic Scheme of the Non-equilibrium Discharge in Nitrogen-Oxygen Mixtures”, Plasma Sources Science and Technology, vol. 1, 1992, pp. 207-220

[51] K. Schofield., “Rate Constants for the Gaseous Interactions of $O(2^1D_2)$ and $O(2^1S_0)$ – a Critical Review”, Journal of Photochemistry, vol. 9, 1978, p. 55-68

[52] Y. Matsumi, K. Tonokura, Y. Inagaki, and M. Kawasaki, “Isotopic Branching Ratios and Translational Energy Release of H and D Atoms in Reaction of $O(^1D)$ Atoms with Alkanes and Alkyl Chlorides”, Journal of Chemical Physics, vol. 97, 1993, pp 6816-6821

[53] N. A. Popov, “Effect of Singlet Oxygen $O_2(a^1\Delta_g)$ Molecules Produced in a Gas Discharge Plasma on the Ignition of Hydrogen Oxygen Mixtures”, Plasma Sources Science and Technology, vol. 20, 2011, 045002

[54] J. T. Herron, “Evaluated Chemical Kinetics Data for Reactions of $N(^2D)$, $N(^2P)$, and $N2(A^3\Sigma_g^+)$ in the Gas Phase”, Journal of Physical and Chemical Reference Data, 28(5), 1999 1453-1483

[55] I. V. Adamovich, T. Li, and W. R. Lempert, “Kinetic Mechanism of Molecular Energy Transfer and Chemical Reactions in Low-Temperature Air-Fuel Plasmas”, Philosophical Transactions of the Royal Society A, vol. 373, 2015, pp. 20140336

[56] A. A. Konnov. “Detailed Reaction Mechanisms for Small Hydrocarbons Combustion, Release 0.5”, http://homepages.vub.ac.be/akonnov/, 2000.

[57] G. J. M. Hagelaar and L.C. Pitchford, "Solving the Boltzmann equation to obtain electron transport coefficients and rate coefficients for fluid models", Plasma Sources Science and Technology, vol. 14, 2005, pp. 722-73

[58] D. C. Allen, E. T. Chandler, E. A. Gregory, R. M. Siddles, and C. J. S. M. Simpson, "Vibrational deactivation of $N_2$ (v= 1) by n-$H_2$ and by p-$H_2$ in the temperature range 300-80 K", Chemical Physics Letters, vol. 76(2), 1980, pp. 347-353

[59] A. Garscadden and R. Nagpal, "Non-equilibrium electronic and vibrational kinetics in $H_2$-$N_2$ and $H_2$ discharges", Plasma Sources Science and Technology, vol. 4(2), 1995, p. 268

[60] N. A. Popov, "Effect of a pulsed high-current discharge on hydrogen–air mixtures", Plasma Physics Reports, vol. 23, 2008, pp. 376-391

[61] ANSYS HFSS: www.ansys.com

[62] R. D. Hancock, F. R. Schauer, R. P. Lucht and R. L. Farrow, " Dual-pump coherent anti-Stokes Raman scattering measurements of nitrogen and oxygen in a laminar jet diffusion flame", Applied Optics, vol. 36(15), 1997, pp. 3217-3226